ESA - Project
From Eötvös to mGal +

WP 2: Improved modeling of SGG-data sets by advanced filter strategies

FINAL REPORT

Wolf-Dieter Schuh, Bonn

November 4, 2002

Summary

Satellite gravity gradiometry (SGG) data allow the recovery of the detailed structures of the Earth's gravity field, which are represented by a set of the order of 100 000 parameters. This large number of parameters has to be derived from an even larger number of correlated observations (tens of millions). Semi-analytical strategies allow to handle this inverse problem in a very efficient way. Especially, the time-wise approach enables the handling of correlations of the observations in the frequency domain. On the other hand, serious restrictions must be imposed to perform this semi-analytical approach. In order to determine realistic measurement scenarios with perturbed orbits, satellite maneuvers, calibration phases and measurement interruptions, only a "brute force" least squares strategy (with the exact observation equations being solved) is able to deal with such kinds of individual situations. Beside the huge numerical computational problem, the modeling of correlated observations adds another difficulty, because it seems to be necessary to invert the variance/covariance matrix. In former studies (e.g. ESA-Study "From Eötvös to mGal") new investigations have been presented, which enable the introduction of spectral behavior of the observation series in a direct approach as discrete filters in the time-domain. The causality of the used filters renders a way for the application of "brute force" least squares adjustment by iterative techniques with sequential access to the observations. Additional investigations are necessary

- to elaborate the theoretical background in detail,
- to improve the numerical implementation of filter tools, and
- to perform test simulations with correlated SGG data sets.

Only a perfect modeling of all available informations can guarantee optimal results. Therefore, it is necessary

- to concretize the long-wavelength behavior of the SGG error budget and to adapt cascaded filters (second order sections), and

- to describe the high-frequency part, with special attention to aliasing and leakage effects.

One additional target of this study is the definition of concrete routines to describe the quality of the SGG-adjustment-models. Special tools must be developed

- to analyze the residuals themselves, but also
- to describe the quality of second level products like geoid heights, geoid slopes and gravity anomalies, and
- to prove the quality of the estimated variance/covariance matrix.

Consequently, the scope of this study within this work package is, to investigate the following **baseline tasks:**

1. Improvement of the theoretical background of the application of digital filter strategies within adjustment procedures (cf. Sec. 2.1).
2. Design and implementation of tailored SGG filters (cf. Sec. 2.2).
3. Elaboration of a test scenario to evaluate the quality of SGG products (cf. Sec. 2.3).
4. Development of statistical test procedures to assess the quality of the adjustment procedure (cf. Sec. 2.4).

2.1 Improvement of the theoretical background of the application of digital filter strategies within adjustment procedures

In geodesy two different approaches are used to model correlated observations. In the space/time domain the autocovariance function allows a very efficient modeling of the correlations. Particularly for small data sets, an individual treatment of each observation is possible. An irregular data distribution and different types of data can be assimilated to one consistent model (*MORITZ (1980)[8]*). But in general, for large data sets it is impossible to handle the covariance matrix, because the dimension of the matrix grows with the number of observations. Therefore, it is necessary to introduce additional restrictions – equispaced data, periodicity – to get special types of matrices (Toeplitz, circulant matrices), which can be treated by tailored strategies very efficiently.

Gathering all the measurements in an observation vector $\boldsymbol{\ell} \in \mathbb{R}^{n\times 1}$ and the corresponding error covariances in the symmetric, positive definite matrix $\boldsymbol{\Sigma}\{\boldsymbol{\ell}\} \in \mathbb{R}^{n\times n}$, we use the Gauss-Markov model to solve the overdetermined system

$$\boldsymbol{\ell} + \boldsymbol{v} = \boldsymbol{A}\boldsymbol{x}, \qquad \boldsymbol{\Sigma}\{\boldsymbol{\ell}\} = \boldsymbol{\Sigma} \tag{2.1}$$

where the design matrix $\boldsymbol{A} \in \mathbb{R}^{n\times m}$ contains the linear (or linearized) relation between observations $\boldsymbol{\ell}$ and the parameters $\boldsymbol{x} \in \mathbb{R}^{m\times 1}$. Applying the least squares optimization principle

$$\langle \boldsymbol{v}, \boldsymbol{v} \rangle_{\boldsymbol{\Sigma}^{-1}} = \boldsymbol{v}^T \boldsymbol{\Sigma}^{-1} \boldsymbol{v} \quad \ldots \quad \text{Min} \tag{2.2}$$

with respect to the $\boldsymbol{\Sigma}^{-1}$ norm leads to the normal equation system

$$\left(\boldsymbol{A}^T \boldsymbol{\Sigma}^{-1} \boldsymbol{A} \right) \tilde{\boldsymbol{x}} = \boldsymbol{A}^T \boldsymbol{\Sigma}^{-1} \boldsymbol{\ell} \tag{2.3}$$

and the best linear unbiased estimator $\tilde{\boldsymbol{x}}$ of the parameter $\boldsymbol{x}$. With respect to gridded data sets or sequences of equispaced samples the covariance matrix $\boldsymbol{\Sigma}$ reflects a Toeplitz structure [1]. The spectral representation of the symmetric covariance matrix is given by

$$\boldsymbol{\Sigma} = \boldsymbol{U} \boldsymbol{\Lambda} \boldsymbol{U}^T \tag{2.4}$$

with the diagonal matrix $\boldsymbol{\Lambda} \in \mathbb{R}^{n \times n}$ of eigenvalues and the orthogonal matrix $\boldsymbol{U} \in \mathbb{R}^{n \times n}$ of eigenvectors. Because of the regular structure these eigenvectors can be expressed in terms of cosine and sine functions

$$\boldsymbol{U} = \frac{2}{\sqrt{N}} \left[\frac{1}{\sqrt{2}}, \cos \boldsymbol{t}, \cos 2\boldsymbol{t}, \ldots, \cos h_c \boldsymbol{t}, \ \sin h_s \boldsymbol{t}, \ldots, \sin \boldsymbol{t} \right] \tag{2.5}$$

with

$$\boldsymbol{t} = \left[0, \ \frac{2\pi}{n}, \ldots, \ (n-1)\frac{2\pi}{n} \right]^T \ , \quad h_c = \text{INT}(\frac{n}{2}) \ , \quad h_s = \text{INT}(\frac{n-1}{2}) \ . \tag{2.6}$$

Therefore, these types of covariance matrices describe immediately the frequency behavior of the measurement series, and the eigenvalues represent the power spectrum of a periodic process (cf. Fig. 2.1).

The two different representations can be used to model the correlations. The time domain approach describes the stochastic behavior of the measurement series in term of the covariance function, and the frequency domain approach uses the power spectral density – the frequency domain representation of the autocovariance function – to model the behavior of the correlated observations (cf. Fig. 2.1). This frequency domain strategy requires the whole measurement series at once, so this series must be complete in the sense of equispaced data within the entire period (periodicity). Otherwise the transformation from the space domain into the frequency domain in a strict form is impossible. Due to the convolution theorem the time consuming circular convolution – a matrix-vector operation – in the space domain corresponds to an element-wise multiplication in the frequency domain (cf. *STRANG (1986)[15]*, pp. 294-329). Therefore, the correlations of the observations, represented by the covariance matrix can be simply expressed by a multiplication frequency by frequency. This frequency domain approach is often denoted as fast collocation (*BOTTONI et al.(1993)[1]*).

In the next section, we will introduce the general model to describe the functional relations between the observations, the deterministic model (unknown parameters) and the stochastic model (unknown signals, random noise). In our approach we use

[1] Unfortunately the inversion process destroys the regular structure, but in this application we deal only with periodic and large sequences of data streams, and therefore, we treat the Toeplitz systems like circulant or infinite systems.

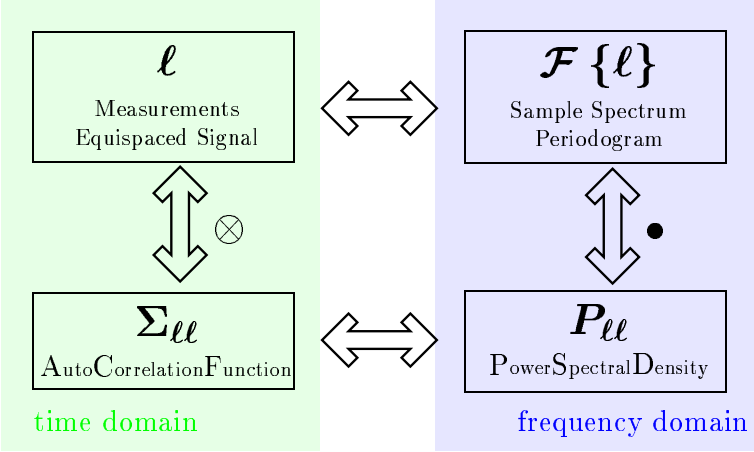

Figure 2.1: This figure summarizes the principle relations between the time domain and the frequency domain. The measurement series $\boldsymbol{\ell}$ and the autocorrelation function in the time domain correspond to the periodogram and the power spectral density in the frequency domain. The correlation theorem states that the correlation $\otimes$ in the time domain is equivalent to a multiplication element-by-element $\bullet$ in the frequency domain. Therefore the auto-covariance function in the time domain corresponds with the square of the amplitude spectrum, which is denoted as power spectral density (confer Sec. 2.1.3). The Fourier transform and inverse Fourier transform perform the transfer from the time domain to the frequency domain and vice versa.

a decorrelation process to transform the measurement series into a form, where each measurement can be treated independently (cf. Section 2.1.2).

Then we will summarize the characteristic quantities of a general linear process and introduce the decorrelation process into this terminology. We will see that the decorrelation process corresponds to a pre-whitening procedure, where the target of a the filter design is to transform a colored noise of a random process into a white Gaussian noise. Especially the application of discrete filters in the time domain enables treating measurement series observation by observation. The advantage of this sequential access can be immediately utilized within the solution process. These computational aspects to treat huge least squares problems and to distribute the numerical effort to a cluster of computers is described in Sec. 2.2.3. It is shown that both the direct and the iterative solver benefit from the sequential access and especially parallel strategies can be brought into action.

As mentioned above, the result of the adjustment procedure, beside the parameters of the Earth's gravity field, are the residuals consisting of a signal and a noise part. If the signal part is well characterized by the covariance function or by the filter process, respectively, the remaining noise should reflect the behavior of white Gaussian noise. In Sec. 2.4 strategies are developed to test this assumption in a statistical strict manner by hypothesis tests.

2.1.1 Observation - General Model

In general we have to discuss the model

$$\ell_i = f_i(\phi_i, \lambda_i, r_i, t_i) + \varepsilon_i \tag{2.7}$$

where each individual observation ℓ_i can be expressed by a function with respect to an Earth-fixed coordinate system (ϕ_i, λ_i, r_i) and the time coordinate t_i. The residuals ε_i reflect the random uncertainties in the measurement process. In general, the functions $f_i(\phi_i, \lambda_i, r_i, t_i)$ can be split into a static part $f_i^s(\phi_i, \lambda_i, r_i)$ and a time dependent dynamic part $f_i^d(\phi_i, \lambda_i, r_i, t_i)$,

$$f_i(\phi_i, \lambda_i, r_i, t_i) = f_i^s(\phi_i, \lambda_i, r_i) + f_i^d(\phi_i, \lambda_i, r_i, t_i) \ . \tag{2.8}$$

The main goal of the GOCE mission is the determination of the static part of the Earth's gravity field. Because not all dynamic effects are efficiently observed by this mission, additional a priori information is necessary to reduce the dynamic effects $f_i^d(\phi_i, \lambda_i, r_i, t_i)$ from the model and especially from the observations. The reduced observations ℓ^s

$$\ell_i^s = \ell_i - f_i^d(\phi_i, \lambda_i, r_i, t_i) \tag{2.9}$$

involve only the static information, with respect to the Earth-fixed system. Because of the incompleteness of the dynamic model an additional uncertainty is introduced by this reduction process, which appears in the remaining model

$$\ell^s = f_i^s(\phi_i, \lambda_i, r_i) + \varepsilon_i^d + \varepsilon_i \tag{2.10}$$

as error ε_i^d. If the a priori knowledge of the dynamic model is good enough, we can expect ε_i^d to be very small and to reflect a stochastic behavior, which is mostly independent from the location of the measurement, but may reflect a small time-dependent influence.

Now we focus our attention on the static model and parameterize the Earth's gravity field in terms of spherical harmonics as base functions,

$$f_i^s(\phi_i, \lambda_i, r_i) = \frac{GM}{r}\left\{1 + \sum_{\ell=2}^{\infty}\sum_{m=0}^{\ell}\left(\frac{R}{r_i}\right)^{\ell}\bar{P}_{\ell m}(\sin\phi_i)\left(\bar{C}_{\ell m}\cos m\lambda_i + \bar{S}_{\ell m}\sin m\lambda_i\right)\right\} . \tag{2.11}$$

G, M and R are the gravitational constant, the Earth's mass and the Earth's reference radius, respectively, while $\bar{P}_{lm}$ denotes the fully normalized Legendre polynomials depending on the harmonic degree ℓ and order m.

Unfortunately, we lose the orthogonality relations of these base functions by using discrete measurement points. Therefore, we have to solve the inverse problem numerically and must restrict the set of parameter to a finite number. Simulation studies (cf. *ESA [3]*, but see also Sec. 2.3.3) show us that the GOCE mission allows a recovery of the Earth's gravity field up to degree 240 to 260 with a reasonable accuracy. This resolution is mainly influenced by the types of measurements and the satellite altitude.

The smoothing effect with respect to the satellite altitude causes the insensitivity of the measurements to high degree coefficients (cf. Fig. 2.26). Therefore, the modeling of high degree coefficients gives rise to numerical instabilities and decreases the accuracy of the whole system. The transition from the stable to the instable system is fluent.

In practice, this series expansion has to be cut off at an upper maximum degree ℓ_{max}, i.e. the upper limit ∞ of the index ℓ is replaced by a finite number ℓ_{max}, defining the resolution of the parameterization

$$f_i^{s_t}(\phi_i, \lambda_i, r_i) = \frac{GM}{r}\left\{1 + \sum_{\ell=2}^{\ell_{max}} \sum_{m=0}^{\ell} \left(\frac{R}{r_i}\right)^{\ell} \bar{P}_{\ell m}(\sin phi_i)\Big(\bar{C}_{\ell m}\cos m\lambda_i + \bar{S}_{\ell m}\sin\lambda_i\Big)\right\}. \quad (2.12)$$

This truncation can be seen as a special type of regularization, but it is also possible to develop the system to a higher degree and stabilize the system by a special regularization.

Both strategies yield to an additional systematic error ε^{s_t}

$$f_i^{s}(\phi_i, \lambda_i, r_i) = f_i^{s_t}(\phi_i, \lambda_i, r_i) + \varepsilon^{s_t} \ . \quad (2.13)$$

We can expect this error to be small and to be treatable as a random signal. Because of the neglected terms, ε^{s_t} depends on the location of the measurement. Each measurement device is characterized by an inertia, which means, that some fluctuations of the measured values are smoothed, because the instrument can not follow in real-time. Especially high frequency information is smoothed, but also the low frequency contents may be influenced by the measurement process.

In many cases the relation between the real signal ℓ_i and the measured quantity ℓ_i^m can be described by a differential equation

$$\ell_i^m(t) + \gamma\frac{d\ell_i^m(t)}{dt} = \ell_i(t) \quad (2.14)$$

with a constant coefficient γ, which is denoted as the *time constant* of the measurement device. The solution of (2.14)

$$\ell_i^m(t) = \int_{-\infty}^{t} \gamma e^{\frac{t'-t}{\gamma}}\ell_i(t')dt' \quad (2.15)$$

shows that the signal $\ell_i(t)$ is a filtered quantity with the transfer function

$$g(\theta) \ = \ \begin{cases} \frac{1}{\gamma}e^{\frac{\theta}{\gamma}} & \theta \le 0 \\ 0 & \theta > 0 \end{cases} \ . \quad (2.16)$$

This causal filter process (only signal contents of the past measurements are merged) influences the output of the measurement device in two ways. The amplitudes of the measurements are smoothed and, in addition, a phase shift of the filter process results in a delay of the measurement time. Both effects can be modeled and eliminated by an inverse filter, if the characteristic of the measurement device is known.

In case of the gradiometer measurements our knowledge of the characteristics of the complex measurement device and process is only poor. The gradiometer has a selected

measurement bandwidth, where it measures the gravity gradients very accurately, while the performance beyond this spectral window is substantially degraded. This leads to correlations between the errors of the measurements, which have to be taken into account. The measurement error has to be split into two parts,

$$\varepsilon_i = \varepsilon_i^{mb} + \varepsilon_i^{w} \ . \tag{2.17}$$

where the time-dependent part ε_i^{mb} defines the correlated part due to the measurement bandwidth, and ε_i^{w} describes a pure white noise random process. The error budget of the gradiometer output (cf. [3]) is given in terms of the power spectral density curves (cf. Fig. 2.2).

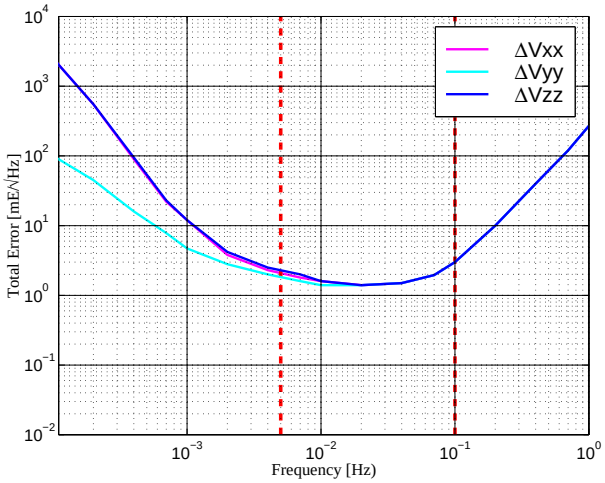

Figure 2.2: Spectra of the gravity-gradient measurement error budget for the components ΔV_{xx}, ΔV_{yy}, and ΔV_{zz} (*Granada*-SGG error budget, cf. [3], pp. 177, digitized Fig. 8.2). Evidently, the error level is below $\pm 3\, mE/\sqrt{Hz}$ within the measurement bandwidth between $5 \times 10^{-3}\, Hz$ and $0.1\, Hz$.

Summarizing all effects, the static part of the observations can be expressed by

$$\ell_i^s = f_i^{s_t}(\phi_i, \lambda_i, r_i) + \varepsilon_i^{s_t} + \varepsilon_i^{d} + \varepsilon_i^{mb} + \varepsilon_i^{w} \ , \tag{2.18}$$

where we can distinguish two main parts of errors. The model truncation effect (spectral leakage) results in a space-dependent correlation of the observations and, therefore, the signal series $\boldsymbol{\varepsilon}^{s_t}$ defines a random process with respect to the location of the measurements. The residuals $\boldsymbol{\varepsilon}^{d}$ and $\boldsymbol{\varepsilon}^{mb}$ are time-dependent due to an incomplete dynamic model and the measurement bandwidth, respectively. But, while the first effect reflects a periodic behavior (seasonal effects, long periodic effects with respect to the satellite revolution (cycle/revolution)), the second part involves a non-periodic behavior. The power spectral density derived from simulation studies (cf. [5]) reflects this different behavior by isolated peaks in the low frequency range for periodic effects and by smeared, smooth behavior in the high frequency part for the non-periodic effect (cf. Fig. 2.3).

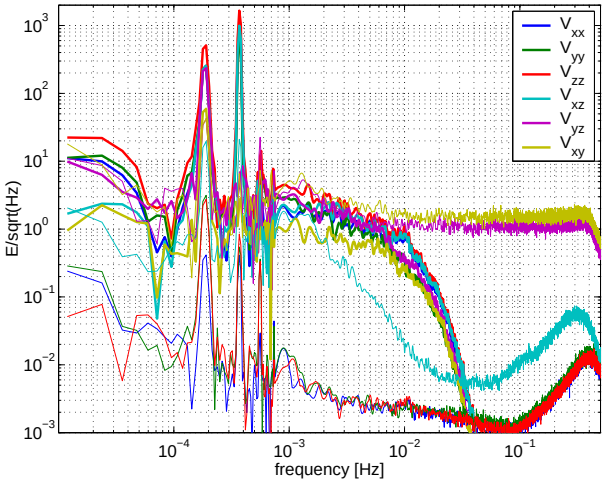

Figure 2.3 : Power Spectral Density: End-to-End Simulator Munich (cf. [5]).

In a general approach the observations are modeled by the deterministic model and a stochastic model. The deterministic model describes the functional relation between the observations and the parameters, in case of the SGG observations the relations between the tensor components T_{xx}, T_{yy}, T_{zz}, and T_{xz}, respectively, and the spherical harmonic coefficients $C_{\ell m}$ and $S_{\ell m}$, which describe the Earth's gravity field. All other influences, especially the time-dependent quantities $\boldsymbol{\epsilon}^{d}$ and $\boldsymbol{\epsilon}^{mb}$, but also the space related quantities $\boldsymbol{\epsilon}^{S_t}$, are described by the signal $\boldsymbol{s}$. The pure white noise random quantity $\boldsymbol{\epsilon}^{w}$ is equivalent to the noise $\boldsymbol{n}$. Fig. 2.4 summarizes these components. Goal of the computation is the best estimation of all three components: the parameter $\boldsymbol{x}$, the signal $\boldsymbol{s}$ and the noise $\boldsymbol{n}$. In our approach the signal depends mainly on instrumental effects. Therefore, we are not interested in the concrete values of the realization. Our main interest is the best computation of the parameters. The remaining residuals should consist only of the signal and the noise part. Applying the right stochastic model means that the filtered residuals reflect a pure random white noise behavior. The filter process is equivalent with reduced residuals, where the signal part is reconstructed by a prediction process. Therefore, test criteria describing this target should be defined (cf. Sec. 2.4).

With respect to the SGG analysis, it will be necessary to investigate two different noise characteristics. On the one hand, a periodic noise characteristic yields a discrete spectrum, which can be modeled very efficiently in the spectral domain. On the other hand, a non-periodic noise characteristic affects a continuous spectrum. To investigate the behavior of different modeling strategies, two different test series are created. The first series is based on a harmonic stochastic process and yields a periodic behavior with a discrete spectrum. The second series is created by a general linear process. The continuous spectrum reflects the non-periodic behavior of this series.

The correct modeling of the correlated measurement series is one of the major issues of the processing of GOCE Level 2 products. Therefore, the theoretical background of random processes has to be investigated. So far, the characteristic quantities to

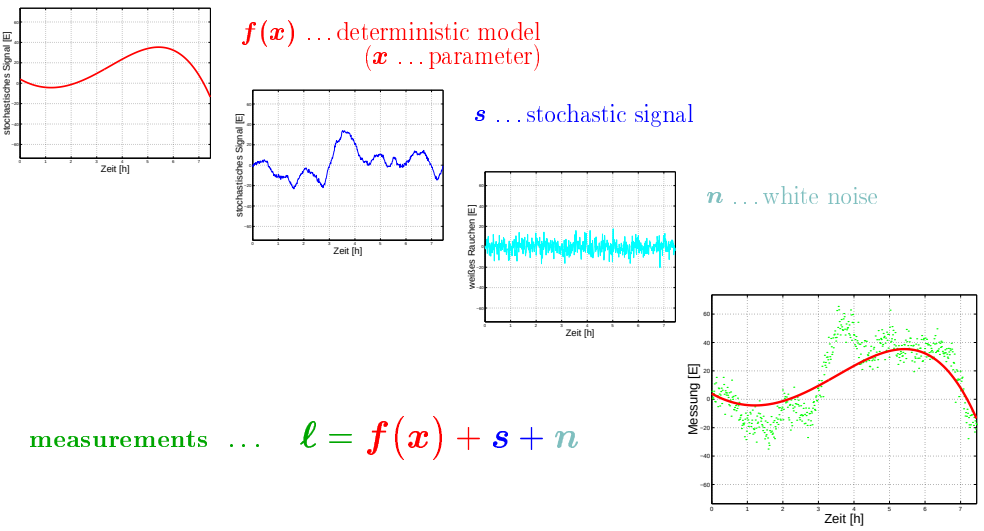

Figure 2.4: Functional relation between observations, deterministic and stochastic model.

describe random processes are identified. We turn special attention to wide-sense stationary Gaussian processes and identify two types of random processes. The **harmonic process**, defined by

$$x(n) = \sum_{i=1}^{I} A_i \cos(n\omega_i + \phi_i) \tag{2.19}$$

with an arbitrary sequence of constants $\{\omega_i\}$, the independent random variables $\{\phi_i\}$ being uniformly distributed between $[-\pi, \pi]$, and the independent random variables $\{A_i\}$. The autocorrelation function of this process reflects a periodic behavior and never delays to zero. The power spectral density function is discrete. With this type of random processes periodic phenomena like remaining drag-forces can be simulated. Special attention is necessary, because, as mentioned above, the autocorrelation function never delays to zero. Therefore, the whole measurement series is correlated and has to be modeled in one piece. A detailed mathematical description of harmonic processes is given in Sec. 2.1.4.

The second type of random processes, the **general linear process**, is given by

$$x(n) = w(n) * h(n) \tag{2.20}$$

where $w(n)$ characterizes a white Gaussian noise and $h(n)$ defines a discrete shift-invariant filter, which is responsible for the spectral behavior of the resulting random process $x(n)$. The autocorrelation function of this type of processes delays to zero, and the spectral density function is continuous due to the fact that the general linear process is non-periodic (cf. Sec. 2.1.5).

Different strategies open the possibility to implement the correlations. In the time domain the application of the covariance matrix or linear filter techniques are available, while in the frequency domain the power spectral density can be used to model the behavior of the measurements.

The main goal of the following is the efficient application of the filter operation in the time domain. We will see that we can reduce the necessary computational effort by substituting the time consuming convolution by an autoregressive moving average (ARMA) operation. As mentioned above the filter process can be seen as a decorrelation process.

2.1.2 Decorrelation - Whitening Process

Again we start from an overdetermined linear equation system

$$\boldsymbol{A}\boldsymbol{x} = \boldsymbol{\ell} + \boldsymbol{v} \qquad \boldsymbol{A} \in \mathbb{R}^{n\times m},\ \boldsymbol{x} \in \mathbb{R}^{m\times 1},\ \boldsymbol{\ell} \in \mathbb{R}^{n\times 1},\ \boldsymbol{v} \in \mathbb{R}^{n\times 1} \tag{2.21}$$

with the design matrix $\boldsymbol{A}$, the parameter vector $\boldsymbol{x}$, the observations $\boldsymbol{\ell}$, and introduce the residuals $\boldsymbol{v}$ to get a consistent system. Applying the least squares adjustment principle the square sum of the residuals has to be minimized with respect to the $\boldsymbol{\Sigma}^{-1}$-norm

$$\langle \boldsymbol{v}, \boldsymbol{v} \rangle_{\boldsymbol{\Sigma}^{-1}} = \boldsymbol{v}^T \boldsymbol{\Sigma}^{-1} \boldsymbol{v} \quad \ldots \quad \text{Min} \qquad \boldsymbol{\Sigma} \in \mathbb{R}^{n\times n} \tag{2.22}$$

where the variance/covariance matrix $\boldsymbol{\Sigma}$ represents the accuracy of the observations as well as the correlations between the observations. This symmetric, positive definite matrix $\boldsymbol{\Sigma}$ can be factorized into two regular, upper triangular systems $\boldsymbol{R}$

$$\boldsymbol{\Sigma} = \boldsymbol{R}^T \boldsymbol{R}\,, \qquad \boldsymbol{R} \in \mathbb{R}^{n\times n}\,. \tag{2.23}$$

The inverse $\boldsymbol{R}^{-1}$ of the regular triangular system can be used to multiply the observation equations from the left and to substitute the Gauss-Markov model (2.1) by

$$\bar{\boldsymbol{\ell}} + \bar{\boldsymbol{v}} = \bar{\boldsymbol{A}}\boldsymbol{x}\,, \qquad \boldsymbol{\Sigma}\{\bar{\boldsymbol{\ell}}\} = \bar{\boldsymbol{\Sigma}} \tag{2.24}$$

with

$$\bar{\boldsymbol{\ell}} = (\boldsymbol{R}^{-1})^T \boldsymbol{\ell}, \qquad \bar{\boldsymbol{v}} = (\boldsymbol{R}^{-1})^T \boldsymbol{v}, \qquad \bar{\boldsymbol{A}} = (\boldsymbol{R}^{-1})^T \boldsymbol{A}\,. \tag{2.25}$$

The covariance matrix $\bar{\boldsymbol{\Sigma}}$ of the transformed observations has to be determined by variance propagation. Introducing (2.23) we end up with

$$\bar{\boldsymbol{\Sigma}} = (\boldsymbol{R}^{-1})^T \boldsymbol{\Sigma} \boldsymbol{R}^{-1} = \boldsymbol{I}\,, \tag{2.26}$$

where $\boldsymbol{I}$ represents the identity matrix. This means that the observations $\bar{\boldsymbol{\ell}}$ of the substitute model (2.24) are uncorrelated and the optimization principle is given by

$$\langle \bar{\boldsymbol{v}}, \bar{\boldsymbol{v}} \rangle_{\boldsymbol{I}} = \bar{\boldsymbol{v}}^T \bar{\boldsymbol{v}} \quad \ldots \quad \text{Min}\,. \tag{2.27}$$

If we denote the matrix $(\boldsymbol{R}^{-1})^T$ by $\boldsymbol{F}$

$$\boldsymbol{F} = (\boldsymbol{R}^{-1})^T \tag{2.28}$$

the transformation (2.25) can be rewritten as

$$\bar{\boldsymbol{\ell}} = \boldsymbol{F}\boldsymbol{\ell}, \qquad \bar{\boldsymbol{v}} = \boldsymbol{F}\boldsymbol{v}, \qquad \bar{\boldsymbol{A}} = \boldsymbol{F}\boldsymbol{A}\,. \tag{2.29}$$

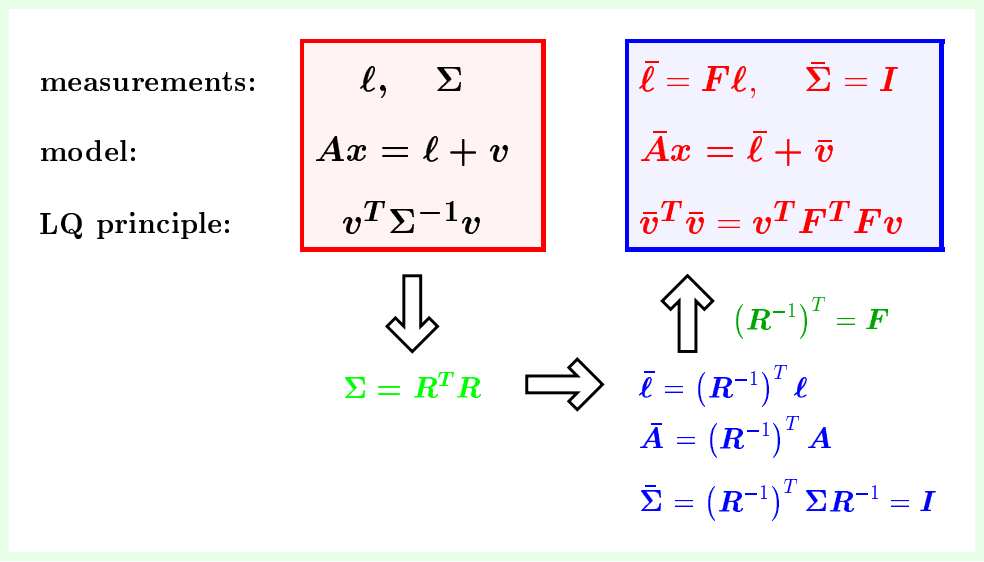

Figure 2.5: Decorrelation Process.

This decorrelation process, which is summarized in Fig. 2.5, works for any covariance matrix, but if the covariance matrix possesses a special structure, e.g. circulant structure because of periodic equispaced data, also the factorized matrices $\boldsymbol{R}$ and $\boldsymbol{F}$ will reflect this property (pay regard to footnote on page 115), and we end up with triangular Toeplitz systems. The multiplication of a Toeplitz system with a vector (2.29) can be interpreted as a convolution of the first column of $\boldsymbol{F}$, denoted by $\boldsymbol{f}$, with the vector $\boldsymbol{\ell}$, thus we get

$$\bar{\boldsymbol{\ell}} = \boldsymbol{f} * \boldsymbol{\ell}\,, \qquad \bar{\ell}(n) = \sum_{k=1}^{n} f(k)\ \ell(n-k) \tag{2.30}$$

or

$$\bar{\boldsymbol{a}}^{(j)} = \boldsymbol{f} * \boldsymbol{a}^{(j)}\,, \qquad j = 1, \ldots, m \tag{2.31}$$

respectively, for each column $\boldsymbol{a}^{(j)}$ of the design matrix $\boldsymbol{A}$. This convolution can be seen as the application of a discrete, linear, shift-invariant filter and the vector $\boldsymbol{f}$ represents the impulse response of the filter (Fig. 2.6).

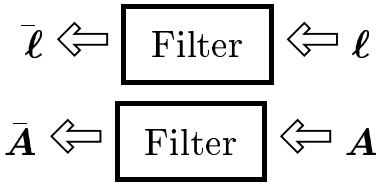

Figure 2.6: Discrete Filter.

Naturally, this filter operation can also be performed in the frequency domain, where the signal $\boldsymbol{\ell}$ is Fourier transformed and denoted as sample spectrum or periodogram

$\mathcal{F}\{\boldsymbol{\ell}\}$, and the impulse response function $\boldsymbol{f}$ is transformed to the frequency response function $\mathcal{F}\{\boldsymbol{f}\}$. The convolution in the time domain degenerates to a simple multiplication in the frequency domain (cf. Fig. 2.7).

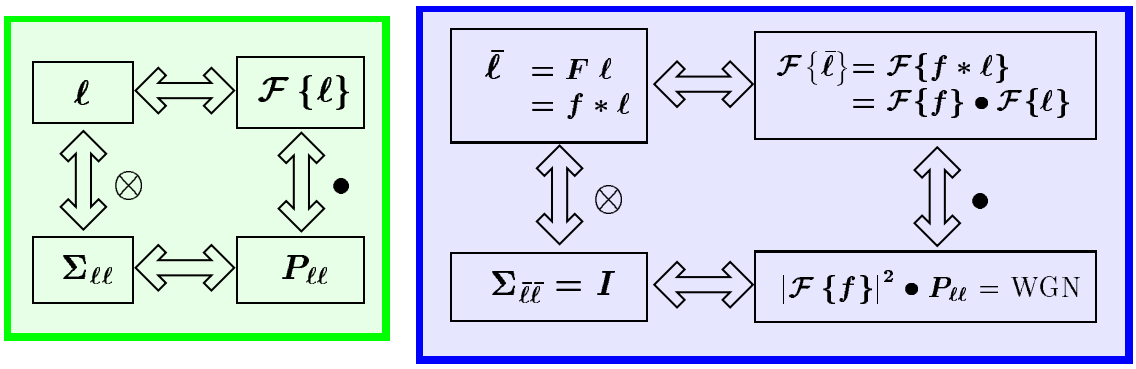

Figure 2.7: Filter Design - **P**ower**S**pectral**D**ensity
$\boldsymbol{f}$ ... impulse response
$\boldsymbol{\mathcal{F}\{f\}}$ ... frequency response
$\boldsymbol{WGN}$ ... white Gaussian noise

Discrete, linear filter techniques enable us to model the spectral behavior of the correlated measurements also in the space domain. The causality of the used filters gives the possibility for the application of the *'direct method'*, a least squares adjustment approach with sequential access to the observations. From the theoretical point of view, both strategies are equivalent. But in practice numerical effects and boundary problems cause slightly different results.

Summarizing, while the *direct method* works in the space domain and model the colored noise by discrete filters applied sequentially to the observation stream, the *semi-analytic approach* switches to the time domain and the corresponding frequency domain.

2.1.3 Characteristic Quantities of a Random Process

A time-discrete random process may be considered as an indexed sequence of random variables

$$\ldots, x(-2), x(-1), x(0), x(1), x(2), \ldots \tag{2.32}$$

where the statistics of each random variable in the sequence $\{x(n)\}$ is defined by a probability distribution. This ensemble of discrete time signals generates a sequence of *mean values* as a function of discrete time steps n

$$m_x(n) = E\{x(n)\} \tag{2.33}$$

and an ensemble of *variances*

$$\sigma_x^2(n) = E\left\{[x(n) - m_x(n)]^2\right\} \tag{2.34}$$

of the process. Two other statistic moments are the *autocovariance*

$$c_x(k,l) = E\left\{[x(k) - m_x(k)]\ [x(l) - m_x(l)]\right\} \tag{2.35}$$

and the *autocorrelation*

$$r_x(k,l) = E\left\{x(k)\, x(l)\right\}\ . \tag{2.36}$$

Note that if $k = l$ the autocovariance function reduces to the variance

$$c_x(k,k) = \sigma_x^2(k)\ . \tag{2.37}$$

As usual, the central moments can be expressed by a linear combination of the non-central moments, and thus the autocovariance sequence is related to the autocorrelation sequence by

$$c_x(k,l) = r_x(k,l) - m_x(k)m_x(l)\ . \tag{2.38}$$

The *cross-covariance* sequence as the interrelation between two random sequences $x(n)$ and $y(n)$ is defined by

$$c_{xy}(k,l) = E\{(x(k) - m_x(k))(y(l) - m_y(l))\}\ , \tag{2.39}$$

and the *cross-correlation* is given by

$$r_{xy}(k,l) = E\{x(k)y(l)\}\ . \tag{2.40}$$

For our approach we consider in particular *stationary* processes, which means that the statistical behavior is time-invariant. As mentioned above, the statistical behavior is expressed by the moments of the process. Therefore, stationarity up to the order m is given if the process $x(n)$ and $x(n+k)$ have the same m^{th}-order joint density function. We restrict our investigations to *wide sense stationary* (WSS) processes. Hence, the following three conditions must be satisfied:

- The mean of the process is independent of time, $m_x(n) = m_x$,
- the autocorrelation $r_x(k,l)$ depends only on the difference $k - l$, and
- the variance of the process is finite, $c_x(0) = \sigma_x^2 < \infty$.

However, in the case of a Gaussian process, wide-sense stationarity is equivalent to strict-sense stationarity. This is a consequence of the fact that a Gaussian random process is completely defined in terms of mean and covariance. A discrete-time random process $x(n)$ is said to be Gaussian if every finite collection of samples of $x(n)$ are jointly

$$f_x(\boldsymbol{x}) = \frac{1}{(2\pi)^{n/2}|\boldsymbol{C}_x|^{1/2}} e^{-\frac{1}{2}(x-m_x)^T C_x^{-1}(x-m_x)} \tag{2.41}$$

with the vector of the expectation values $\boldsymbol{m}_x$ and the covariance matrix $\boldsymbol{C}_x$, where the individual elements are defined by

$$m_x(i) = E\{x(i)\} \quad \text{and} \quad c_{ij} = c(i,j) = E\{(x(i) - m_x(i))(x(j) - m_x(j))\}\ . \tag{2.42}$$

The autocorrelation sequence of a WSS process provides a description of the second-order moment of the process in time domain. If we compute its discrete Fourier transform

$$P_x\left(e^{j\omega}\right) = \sum_{k=-\infty}^{\infty} r_x(k)\ e^{-jk\omega}\ , \tag{2.43}$$

we obtain the *power spectral density* (power spectrum) of the process, which characterizes the second order moment of the process in the frequency domain. The *total power* of the process is proportional to the area under the power spectral density curve

$$E\left\{|x(n)|^2\right\} = \frac{1}{2\pi}\int_{-\pi}^{\pi} P_x\left(e^{j\omega}\right)\ d\omega\ . \tag{2.44}$$

Standard discrete parameter models can be divided into two quite different groups: the general linear processes and the harmonic processes.

2.1.4 Harmonic Process

A harmonic process is defined by

$$x(n) = \sum_{i=1}^{I} A_i \cos(n\omega_i t + \phi_i) \tag{2.45}$$

where $I, \{A_i\}, \{\omega_i\}, (i = 1, \ldots, I)$ are constants and the phases $\{\phi_i\}, (i = 1, \ldots, k)$ are independent random variables, each having a rectangular distribution on the interval $(-\pi, \pi)$. Caused by the independence of the random variables $\{\phi_i\}$ it can be shown that $x(n)$ represents a stationary process, irrespective of the values of $\{A_i\}, \{\omega_i\}$. For simplicity, the case with just one cosine term $(I = 1)$

$$x(n) = A\cos(n\omega + \phi) \tag{2.46}$$

is treated. The probability density function of a rectangular distribution is given by

$$f(\phi) = \begin{cases} 0 & \phi \le -\pi \\ \frac{1}{2\pi} & -\pi \le \phi \le \pi \\ 0 & \pi \le \phi\ . \end{cases} \tag{2.47}$$

If we introduce (2.46) to the expectation operator

$$E\{x(n)\} = \int_{-\infty}^{\infty} x(n) f(\phi) d\phi \tag{2.48}$$

we get

$$\begin{aligned} E\{x(n)\} &= \int_{-\infty}^{\infty} A\cos(n\omega + \phi) f(\phi)\ d\phi \\ &= \frac{A}{2\pi}\int_{-\pi}^{\pi} \cos(n\omega + \phi)\ d\phi \\ &= \frac{A}{2\pi}\int_{-\pi}^{\pi} \left(\cos n\omega \cos\phi - \sin n\omega \sin\phi\right)\ d\phi \end{aligned}$$

$$= \frac{A}{2\pi}\Big[\cos n\omega \sin\phi + \sin n\omega \cos\phi\Big]_{-\pi}^{\pi}$$
$$= \frac{A}{2\pi}\Big(-\sin n\omega + \sin n\omega\Big) = 0\ . \tag{2.49}$$

Also

$$c_x\{k,\ell\} = E\{x(k), x(\ell)\} = \frac{A^2}{2\pi}\int_{-\pi}^{\pi}\cos(k\omega+\phi)\cos(\ell\omega+\phi)\ d\phi$$
$$= \frac{A^2}{2\pi}\int_{-\pi}^{\pi}\cos((k-\ell)\omega+\ell\omega+\phi)\cos(\ell\omega+\phi)\ d\phi\ . \tag{2.50}$$

Using the theorem

$$\cos(x+y)\cos(x-y) = \frac{1}{2}(\cos 2x + \cos 2y) \tag{2.51}$$

with

$$x = \omega x + \phi + \frac{1}{2}(k-\ell)\omega$$
$$y = \frac{1}{2}(k-\ell)\omega \tag{2.52}$$

results in

$$\cos((k-\ell)\omega+\ell\omega+\phi)\cos(\ell\omega+\phi) = \frac{1}{2}\Big(\cos(2(\ell\omega+\phi)+(k-\ell)\omega)+\cos(k-\ell)\omega\Big)\ . \tag{2.53}$$

Therefore, (2.50) can be expressed by

$$c_x\{k,\ell\} = \frac{A^2}{4\pi}\int_{-\pi}^{\pi}\Big(\cos(2(\ell\omega+\phi)+(k-\ell)\omega)+\cos(k-\ell)\omega\Big)d\phi$$
$$= \frac{A^2}{4\pi}\Big[\sin(2(\ell\omega+\phi)+(k-\ell)\omega)\Big]_{-\pi}^{\pi} + \cos(k-\ell)\omega\Big[\phi\Big]_{-\pi}^{\pi}\ . \tag{2.54}$$

The first term in the above integral vanishes and hence the autocovariance function consists of a cosine term

$$c_x\{k,\ell\} = \frac{1}{2}A^2\cos(k-\ell)\omega \tag{2.55}$$

which depends only on the time difference $(k-\ell)$

$$c_x\{k,\ell\} = c_x\{k-\ell\} = \frac{1}{2}A^2\cos(k-\ell)\omega\ . \tag{2.56}$$

This shift invariant function never delays to zero.

If the random variables $\{\phi_i\}, (i = 1,\ldots,I)$ are independent the probability density function is defined as the product of the I marginal density functions

$$f(\phi_1\ldots\phi_I) = f_1(\phi_1)\cdot\ldots\cdot f_I(\phi_I) \tag{2.57}$$

where each marginal density function results in

$$f_i(\phi_i) = \begin{cases} 0 & \phi_i \le -\pi \\ \frac{1}{2\pi} & -\pi \le \phi_i \le \pi \\ 0 & \pi \le \phi_i\ . \end{cases} \tag{2.58}$$

The harmonic process (2.45) results in a stationary process. This process is characterized by a zero mean

$$m_x = E\{x(n)\} = 0 \,, \tag{2.59}$$

and the autocorrelation (= autocovariance) sequence

$$r_x(k,l) = r_x(k-l) = \frac{1}{2}\sum_{i=1}^{I} A_i^2 \cos\left((k-l)\omega_i\right) \tag{2.60}$$

depends only on the time difference $k-l$. The variance σ_x^2 is given by

$$\sigma_x^2 = R(0) = \sum_{i=1}^{I} \frac{1}{2} A_i^2 \,. \tag{2.61}$$

Thus, the harmonic process is a WSS process. The power spectral density can be determined by

$$P_x\left(e^{j\omega}\right) = \frac{1}{2}\pi \sum_{i=1}^{I} A_i^2 \left[\delta(\omega-\omega_i) + \delta(\omega+\omega_i)\right] \tag{2.62}$$

where $\delta(\omega-\omega_i)$ is used to denote an impulse at frequency $\omega = \omega_i$, and $\delta(\omega+\omega_i)$ is an impulse at $-\omega_i$. If, in addition, the amplitudes $\{A_i\}$ are also uncorrelated random variables, the autocorrelation sequence is

$$r_x(k,\ell) = r_x(k-\ell) = \frac{1}{2}\sum_{i=1}^{I} E\{A_i^2\} \cos\left((k-\ell)\omega_i\right) \quad , \tag{2.63}$$

and the power spectral density can be computed by

$$P_x\left(e^{j\omega}\right) = \frac{1}{2}\pi \sum_{i=1}^{I} E\{A_i^2\} \left[\delta(\omega-\omega_i) + \delta(\omega+\omega_i)\right] \quad , \tag{2.64}$$

again defining a WSS process.

It should be mentioned here that equation (2.45) may also be written as

$$x_(n) = \sum_{i=1}^{k} \left(\bar{A}_i \cos n\omega_i + \bar{B}_i \sin n\omega_i\right) \tag{2.65}$$

where the coefficients a_i and b_i can be determined by

$$a_i = A_i \cos\phi_i \,, \quad b_i = -A_i \sin\phi_i \,. \tag{2.66}$$

If we introduce the coefficients a_i and b_i as uncorrelated, zero mean and random variables with a common variance σ_i^2 we end up with the autocorrelation

$$r_x(k,\ell) = r_x(k-\ell) = \sum_{i=1}^{I} \sigma_i^2 \cos\left((k-\ell)\omega_i\right) \tag{2.67}$$

and the power spectral density

$$P_x\left(e^{j\omega}\right) = \pi \sum_{i=1}^{I} \sigma_i^2 \left[\delta(\omega - \omega_i) + \delta(\omega + \omega_i)\right] \ . \tag{2.68}$$

Therefore, this approach can be used to generate a harmonic WSS process as well. But this definition has an additional benefit, because its allows to describe a special type of WSS processes, a Gaussian process, where the probability density function of the coefficients a_i and b_i are defined by the two-dimensional joint normal distribution. Because of the independence of the coefficients and the identical variance σ_i^2 the two-dimensional normal distribution is given as the product of the marginal density functions

$$\begin{aligned} f(a_i, b_i)da_i db_i &= \frac{1}{2\pi\sigma_i^2}\ e^{-\frac{a_i^2}{2\sigma_i^2}}\ \ e^{-\frac{b_i^2}{2\sigma_i^2}}\ da_i\ db_i \\ &= \frac{1}{2\pi\sigma_i^2}\ \ e^{-\frac{a_i^2+b_i^2}{2\sigma_i^2}}\ da_i\ db_i \ . \end{aligned} \tag{2.69}$$

The two-dimensional distribution of the amplitude A_i and the phase ϕ_i can be derived by converting the Cartesian coordinates a_i, b_i into polar coordinates

$$A_i = \sqrt{a_i^2 + b_i^2}\ , \quad \phi_i = \mathrm{ATAN2}(-b_i, a_i) \tag{2.70}$$

and, therefore, the infinitesimal area element is given by

$$da_i\ db_i = A_i\ dA_i\ d\phi_i \ . \tag{2.71}$$

As defined above the expectations of a_i and b_i is equal zero, and both coefficients possess the same variance σ_i. This variance is connected with the expectation of the square amplitude by

$$E\{A_i^2\} = E\{a_i^2\} + E\{b_i^2\} = 2\sigma_i^2 \tag{2.72}$$

and defines a *mean energy* of the process with respect to the frequency ω_i. Substituting (2.71) and (2.72) in (2.69) the probability density function of A_i and ϕ_i becomes

$$f(A_i, \phi_i)dA_i d\phi_i = \frac{2A_i}{E\{A_i^2\}}\ \ e^{-\frac{A_i^2}{E\{A_i^2\}}}\ dA_i\ \ \frac{1}{2\pi}\ d\phi_i \ , \tag{2.73}$$

which can be easily represented as a product of two one-dimensional functions

$$f(A_i, \phi_i)dA_i d\phi_i = f(A_i)dA_i\ f(\phi_i)d\phi_i \ . \tag{2.74}$$

This means that the amplitude A_i and the phase ϕ_i are independent. The distribution of the phase ϕ_i is given by

$$f(\phi_i) = \frac{1}{2\pi} \tag{2.75}$$

and defines a uniform distribution. The statistical behavior of the amplitude A_i is given by the probability density function

$$f(A_i) = \frac{2A_i}{E\{A_i^2\}}\ \ e^{-\frac{A_i^2}{E\{A_i^2\}}} \ . \tag{2.76}$$

Using (2.72) the constant parameter $E\{A_i^2\}$ can be substituted by $2\sigma_i^2$ and (2.76) results in

$$f(A_i;\sigma_i) = \frac{A_i}{\sigma_i^2} \; e^{-\frac{A_i^2}{2\sigma_i^2}} \; . \tag{2.77}$$

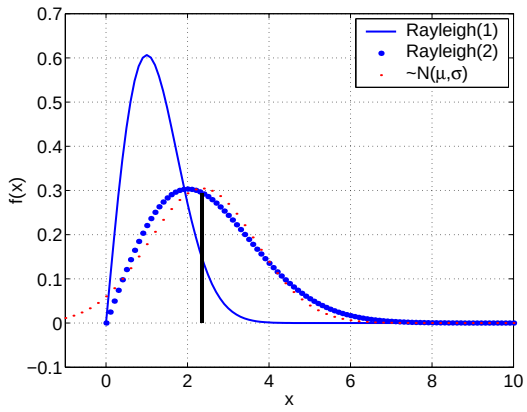

Figure 2.8: Probability density function of the Rayleigh distribution. This distribution is only defined for positive values. The maximum of the function $f(x;b)$, which defines the most probable value x_p is fixed by the parameter b, $x_p = b$. The median x_m (probability = 0.5) is given by $x_m = b\sqrt{2\,ln2}$. The expectation $E\{x\}$ can be derived as $E\{x\} = b\sqrt{\pi/2}$, and the variance σ_R can be computed by $\sigma_R = \frac{4-\pi}{2}\,b^2$. To compare the behavior of the Rayleigh distribution $f(x;2)$ (bold dashed), the normal distribution $f(x;x_m,\sigma_R)$ is plotted (dashed). Especially for small x the difference is evident.

Therefore, the probability density function of the amplitudes is equivalent with the *Rayleigh distribution*, which is defined by

$$f(x;b) = \frac{x}{b^2} \; e^{-\frac{x}{2b^2}} \tag{2.78}$$

with the parameter b (cf. Fig. 2.8).

Summarizing the properties of a Gaussian process, we can say that the coefficients a_i and b_i are independent, normally distributed with the same variance σ_i. The phase ϕ_i has to reflect a uniform distribution and the amplitudes A_i are Rayleigh distributed, where σ_i defines the corresponding parameter b.

But we must keep in mind that a stationary process is characterized by a continuous spectrum. Therefore, we need an infinite realization of this process, because then, the discrete spectral lines are agglomerated to a continuous spectrum. In this case, a range in the spectrum is characterized by infinitesimally dense adjacent frequencies, and each realization of the stochastic process shows arbitrary results depending on the actually interfered frequencies of the process. But on the other hand, if the probability

density distribution of the coefficients a_i and b_i or the amplitude A_i and phase ϕ_i are known, different realizations of the same process can be computed by varying these parameters. Therefore, the computation of the expectation of the infinite series can be substituted by the ensemble-mean, the mean over different realizations. This property of stationary processes is denoted as *ergodicity*.

2.1.5 General Linear Process

A *general linear process* is given by the convolution

$$\boldsymbol{y} = \boldsymbol{x} * \boldsymbol{h} \tag{2.79}$$

or written in sequence form

$$y(n) = x(n) * h(n) = \sum_{k=-\infty}^{\infty} h(k)\ x(n-k) \tag{2.80}$$

with a stationary random sequence $x(n)$ and a linear shift-invariant filter defined by the impulse response $h(n)$. The mean of this process

$$m_y(n) = E\{y(n)\} = E\left\{\sum_{k=-\infty}^{\infty} h(k)\ x(n-k)\right\} = m_x \sum_{k=-\infty}^{\infty} h(k) = m_y \tag{2.81}$$

is independent of the time n, and thus the autocorrelation sequence

$$r_{yy}(k) = r_{xx}(k) * h(k) * h(-k) \tag{2.82}$$

is also shift-invariant and depends only on time differences expressed by k. If we look at processes with zero mean $m_x = 0$, the autocorrelation sequences $r_{xx}(k)$ and $r_{yy}(k)$ as second moments correspond to the autocovariance sequences $c_{xx}(k)$ and $c_{yy}(k)$ as second central moments

$$c_{yy}(k) = c_{xx}(k) * h(k) * h(-k)\ . \tag{2.83}$$

Therefore, the power spectral density of the filtered process is given by

$$P_{yy}\left(e^{j\omega}\right) = P_{xx}\left(e^{j\omega}\right)\left|H\left(e^{j\omega}\right)\right|^2 \tag{2.84}$$

where $H\left(e^{j\omega}\right)$ denotes the frequency response of the filter defined by the Fourier transformed impulse response sequence $h(n)$

$$H\left(e^{j\omega}\right) = \sum_{k=-\infty}^{\infty} h(k)e^{-jk\omega} = \mathcal{F}\left\{h(k)\right\}\ . \tag{2.85}$$

The power spectral densities P_{yy} and P_{xx} are obtained by the Wiener-Khinchin theorem as the Fourier transforms of the autocorrelation sequence $r_{yy}(k)$

$$P_{yy}\left(e^{j\omega}\right) = \sum_{k=-\infty}^{\infty} r_{yy}e^{-jk\omega} = \mathcal{F}\left\{r_{yy}(k)\right\} \tag{2.86}$$

and $r_{xx}(k)$, respectively. In terms of z-transforms (2.84) is written as

$$P_{yy}(z) = P_{xx}(z)\, H(z)\, H^*(1/z^*)\ . \tag{2.87}$$

where z can be interpreted as a shift operator $z^\alpha h(k) = h(k-\alpha)$. The reverse sequence $h(-k)$ of the impulse response $h(k)$ is substituted by the conjugated reciprocal form $H^*(1/z^*)$.

Thus, if we use a white noise process as input process $x(n)$, the frequency response function $H\left(e^{j\omega}\right)$ of the filter will determine the spectral behavior of the output process $y(n)$. This relation is used to generate colored sequences of measurement noise. In our simulations of the performance of the GOCE gradiometer mission, we start with a given power spectral density function, which was deduced from simulation studies and which describes the spectral behavior of the gradiometer measurements (cf. Fig. 2.2). We compute the square root form and design a linear shift-invariant filter with a frequency response function, which reflects the same behavior.

Exactly the other way round can be gone to decorrelate the measurements. Here we start with a colored input sequence $x(n)$ and try to find a filter, which "pre-whitens" this sequence. The resulting sequence $y(n)$ has to reflect white Gaussian noise (WGN), which means that the power spectrum density function doesn't favor particular frequencies. The flattening of P_{yy} can be obtained by multiplying the power spectral density P_{xx} of the colored sequence $x(n)$ by a function $|\mathcal{F}\{\boldsymbol{f}\}|^2$, which reflects the inverse behavior (cf. Fig. 2.7).

In general, this linear shift-invariant discrete system can be represented by the difference equation

$$y(n) + \sum_{l=1}^{n_a} a_l\, y(n-l) = \sum_{l=0}^{n_b} b_l\, x(n-l) \tag{2.88}$$

with a finite number n_a and n_b of constant coefficients a_l and b_l. The corresponding frequency response function (denoted here as filter *transfer* or *system function*) is given by

$$H(z) = \frac{\sum\limits_{l=0}^{n_b} b_l\, z^{-l}}{1 + \sum\limits_{l=1}^{n_a} a_l\, z^{-l}}\ . \tag{2.89}$$

Signal processing tools enable us to design discrete linear filters, which can express the correlation between the observations. In general, there are two types of filters:

- *Nonrecursive filters*, which describe the relation between input and output sequence by a convolution. These filters are also denoted as *convolution* or *transversal filters*. They are represented by a moving average operation in the time domain and by the product of the spectra as given by (2.84) in the frequency domain.
- *Recursive filters*, for which the filter output $y(n)$ at time $t_n = n$ is computed recursively from the filter output $y(j)$, $j < n$ and the input sequence $x(k)$, $k \leq n$.

Therefore, the summation indices n_a and n_b in (2.88) determine the type of the filter, which is often denoted as **A**uto-**R**egressive-**M**oving-**A**verage (ARMA) filter

- $n_a=0$, $n_b>0$ ... convolution filter, ARMA(0,n_b) filter,
- $n_a>1$, $n_b=0$ ... recursive filter, ARMA(n_a,0) filter and
- $n_a>1$, $n_b>0$ ... ARMA(n_a,n_b) filter.

All types of filters have their advantages and disadvantages. The examples in Sec. 2.2.3 show two typical applications of pre-whitening filters in least squares problems, applying a recursive filter ARMA(2,2) to minimize the number of operations during the assembling of the normal equations. In contrast, a moving average filter ARMA(0,88) is integrated in the iterative solution process, because the symmetry of this type of filter allows an efficient access to compute the update steps.

2.1.6 Non-stationary Processes

In many applications the random process is superposed by periodic distortions due to unmodeled effects (tides, atmosphere, ...) or model inconsistencies (truncation error, spectral leakage, ...). These periodic effects cause discrete frequency lines, which are merged with the continuous spectrum of the stationary process. In contrast to a pure stationary process the probability density function of the amplitude A_i and phase ϕ_i of the disturbed process do not reflect the Rayleigh and uniform distribution. We denote the amplitudes of the disturbing elements by A_i^d in contrast to the amplitudes of the stationary process with A_i^s. The energy of the disturbing oscillation is defined by the squared amplitude $(A_i^d)^2$ (deterministic approach) and the energy of the stationary process is again defined by the expectation $E\{(A_i^s)^2\}$ (stochastic approach). Using (2.72) the mean energy is equivalent to $2(\sigma_i^s)^2$. The probability density function for the amplitude A_i of the non-stationary process is given by

$$f(A_i;\sigma_i^s,A_i^d) = \frac{A_i}{(\sigma_i^s)^2}\; e^{-\frac{A_i^2+(A_i^d)^2}{2(\sigma_i^s)^2}}\; I_0\left(\frac{A_i A_i^d}{(\sigma_i^s)^2}\right) \tag{2.90}$$

where $I_0(x) = J_0(ix)$ defines the modified zeroth order Bessel function of the first kind, or the Bessel function J_0 with a complex argument. This probability density function is named *Rice distribution* (cf. e.g. *TAUBENHEIM [16]*, pp. 238).

In contrast to the Rayleigh distribution the Rice distribution fits especially for high signal-to-noise ratios s

$$s = \sqrt{\frac{(A_i^d)^2}{E\{(A_i^s)^2\}}}\,, \tag{2.91}$$

defined by the quotient between the energy of the involved signal $(A_i^d)^2$ and the noise $E\{(A_i^s)^2\}$, to a normal distribution. The parameters of the fitting normal distribution are fixed by the same expectation and variance values. If one of the two factors is

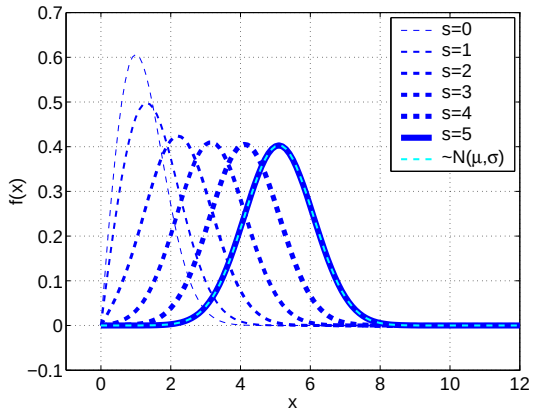

Figure 2.9 : Probability density function of the Rice distribution $f(x; b, c)$. This distribution is only defined for positive values. The ratio $s = c/b$ between the parameters influences the shape of the function. The graph shows different ratios, where the first parameter is fixed ($b = 1$) and the second parameter c is modified between 0 and 5. If $c = 0$ or $s = 0$ the Rice distribution degenerate to the Rayleigh distribution (cf. Fig. 2.8). For larger factors s the Rice distribution converges to the normal distribution. The plotted normal distribution with the expectation μ and the variance σ, computed from the Rice distribution $f(x; 1, 5)$, demonstrates this behavior.

known a priori (e.g. the noise level), the other one can be estimated (e.g. a systematic shift due to spectral leakage).

In addition it should be mentioned that the behavior of the phase also reflects a typical characteristic for non-stationary processes . Due to the definition of an infinite process, the phase spectrum of a stochastic process is continuous. Therefore, the phase alters permanently, and each individual realization - each part of the measurement series - reflects an individual phase parameter. But on the other hand a deterministic disturbance does not change the phase. This typical behavior can be utilized to detect also deterministic effects with a small signal-to-noise ratio. Capmann and Bartels (cf. e.g. *TAUBENHEIM (1969) [16]*, pp. 300-304) have elaborated strategies to recover such deterministic effects.

2.2 Design and implementation of tailored SGG filters

2.2.1 Implementation of Digital Filters

To elaborate an efficient implementation of a digital frequency selective filter, we use the normalized form of the difference equation

$$y[n] = \sum_{l=0}^{nb} b_l \; x[n-l] - \sum_{l=1}^{na} a_l \; y[n-l] \tag{2.92}$$

where $x[\,]$ denotes the input sequence and $y[\,]$ represents the output sequence. All coefficients are normalized, which means $a_0 = 1$. This formula can be interpreted as a computational algorithm. Each new value of the output sequence $y[n]$ can be computed by the sum of the delayed values of the input sequence $x[n-l]$ multiplied by the constant coefficients b_l and by the sum of the delayed values of the output sequence $y[n-l]$ multiplied by a_l. If this algorithm is implemented on a digital computer, it is necessary to store the past nb values of the input sequence as well as the past na values of the output sequence. If we include a filter procedure to describe the correlation in a least squares adjustment procedure, it may be necessary (especially for direct solvers, cf. Sec. 2.2.3) to apply this filter on each column of the observation matrix, i.e. about 60.000 (degree/order 240) filter processes done simultaneously. Therefore, a reduction of the number of registers, which represent the '*memory*' of the filter, is useful. This can be done by reformulating formula (2.92) in an analytic way. A very efficient and illustrative approach uses signal-flow graphs to represent a digital filter (*OPPENHEIM et al. (1975)[9]*, Sec. 4). The theory of flow-graphs allows us to construct a variety of structures which are equivalent with respect to the input-output characteristics. To represent a linear shift-invariant digital filter as a flow-graph, we only need three basic operations. The addition of two sequences, the multiplication of a sequence by a constant and a unit delay step, that means the storage of the previous value of the sequence (cf. Fig. 2.10). The last step is connected with a register, which is updated after each step.

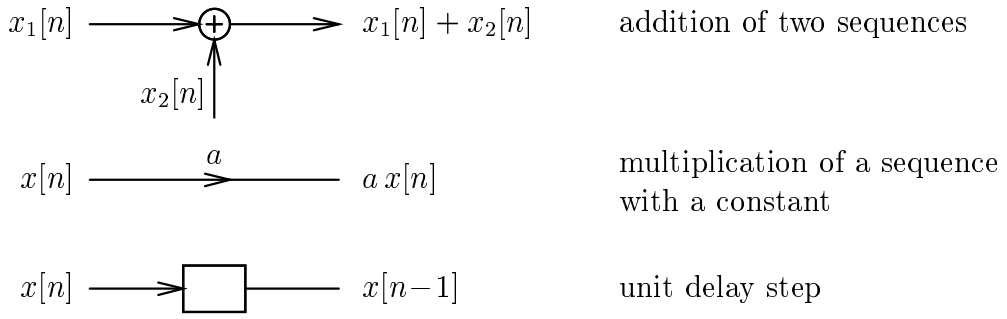

Figure 2.10: Block-diagram representation of the three basic operations.

To simplify the following graphs we restrict ourselves to a small number of delay elements. Therefore, the order of the filter is fixed by $nb = na = 2$. The difference equation

$$y[n] = \sum_{l=0}^{2} b_l \; x[n-l] - \sum_{l=1}^{2} a_l \; y[n-l] \tag{2.93}$$

$$= b_0\,x[n] + b_1\,x[n-1] + b_2\,x[n-2] - a_1\,y[n-1] - a_2\,y[n-2] \tag{2.94}$$

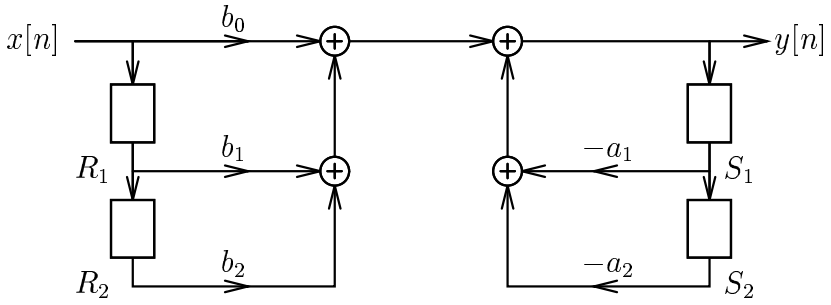

Figure 2.11: Block-diagram representation for a 2^{nd}-order difference equation; '*direct form*'.

can be represented by the flow-chart 2.11. The incomingelement $x[n]$ on the left side is involved in two operations: on the one hand (straight line) the incoming element is multiplied by b_0, the result is added to the stream $b_1\,R_1$, $b_2\,R_2$, ..., and it is easy to see that the value of R_1 corresponds to the previous input element $x[n-1]$, and that R_2 corresponds to $x[n-2]$; on the other hand the incoming element $x[n]$ causes a shift of the memory cells, denoted as *update* step.

In the right part of the flow-chart the autoregressive part is illustrated. Let us start again with the straight line. After some additions this path yields the result $y[n]$. Due to this fact the registers S_1 and S_2 on the right are filled with the results $y[n-1]$ and $y[n-2]$, resp., of the last steps. Therefore, the added terms $-a_1\,S_1$ and $-a_2\,S_2$ correspond to the autoregressive terms. This implementation requires nb+na registers to manage the *memory* of the filter. Each computational step

$$y[n] = b_0\,x[n] + b_1\,R_1 + b_2\,R_2 - a_1\,S_1 - a_2\,S_2 \tag{2.95}$$

is followed by an update step

$$\begin{array}{lcllcl} R_2 & = & R_1 & S_2 & = & S_1 \\ R_1 & = & x[n] & S_1 & = & y[n]\,. \end{array} \tag{2.96}$$

It is easy to see that a difference equation of a higher order does not affect the structure of the system essentially. Only the cascades on the left and right side consist of more steps. The flow-graph theory states that the order of the cascades have no influence on the input-output behavior of a linear shift-invariant system. Therefore, Fig. 2.12 represents the same difference equation[1] but yields a different computational algorithm.

The right side essentially reflects the computational step

$$y[n] = b_0\,R_0 + b_1\,R_1 + b_2\,R_2 \tag{2.97}$$

whereas the left side represents the auxiliary computation R_0

$$R_0 = x[n] - a_1\,R_1 - a_2\,R_2 \tag{2.98}$$

in combination with the update steps

[1] if we neglect numerical differences caused by a finite representation of the numbers

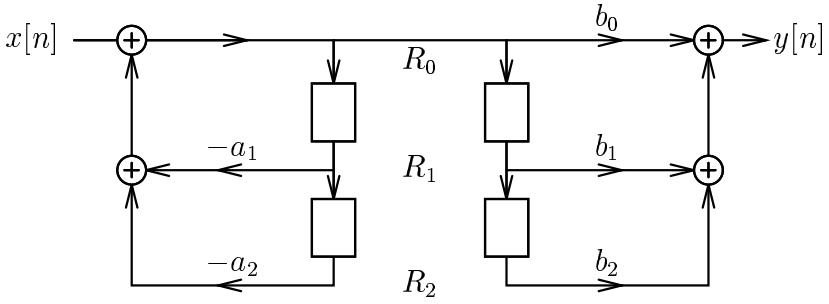

Figure 2.12 : Block-diagram representation for a 2^{nd}-order difference equation; '*direct form, reverse cascaded*'.

$$\begin{aligned} R_2 &= R_1 \\ R_1 &= R_0 \, . \end{aligned} \tag{2.99}$$

This structure halves the number of registers, because both cascades can use the same set of registers. The next flow-graph procedure, which leaves the transmission between input and output unchanged, is called *transposition*. The transposition of a flow graph is accomplished by reversing the direction of all branches in the network. Fig. 2.13 shows the transposed form of Fig. 2.11.

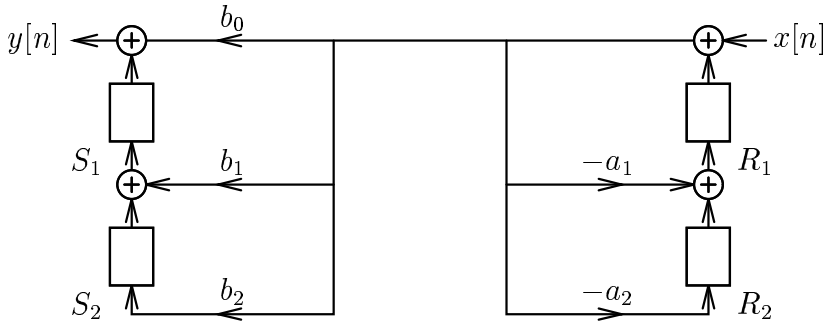

Figure 2.13 : Block-diagram representation for a 2^{nd}-order difference equation; '*transposed form*'.

The input sequence $x[n]$ enters the system from the right side. The output sequence leaves the system on the left. Again, the reversed cascaded form of this transposed form is of main interest for the implementation on a digital computer (cf. Fig. 2.14).

Especially if we associate the unit delay steps and registers in the middle (cf. Fig. 2.15), a well tailored computational algorithm can be derived.

The computational step is restricted to

$$y[n] = b_0 \, x[n] \; + \; Z_1 \tag{2.100}$$

and followed by the update step

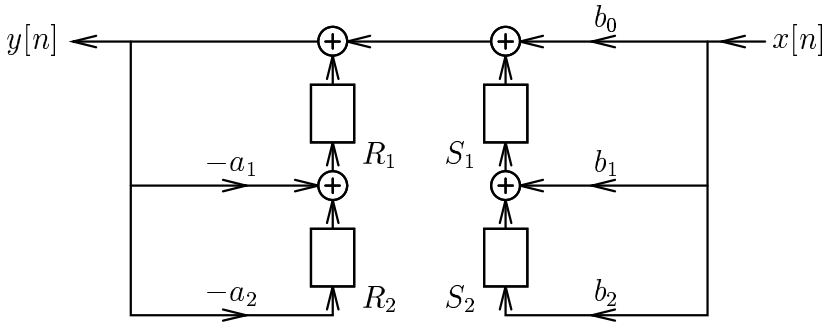

Figure 2.14: Block-diagram representation for a 2^{nd}-order difference equation; '*transposed form, reverse cascaded*'.

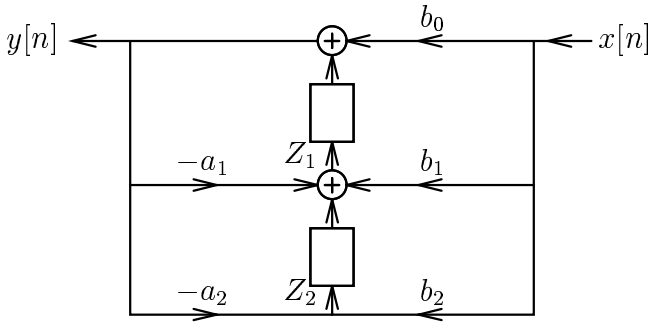

Figure 2.15: Block-diagram representation for a 2^{nd}-order difference equation; '*transposed form, reverse cascaded, compressed memory*'.

$$\begin{array}{lcllll} Z_1 & = & b_1\, x[n] & + & Z_2 & - & a_1\, y[n] \\ Z_2 & = & b_2\, x[n] & & & - & a_2\, y[n]\ . \end{array} \tag{2.101}$$

If the order of the filter is larger than two (2), then the first update step has to be iterated $na-1$ times. This structure requires the minimum number of delay elements or registers, respectively. Therefore, we introduce this form (cf. Alg. 2.2.1) into the computational algorithms.

The initial state condition that past inputs as well as outputs are zero ($\bar{\ell}[i] = 0$, $\ell[i] = 0$, $i < 0$), corresponds to a '*zero memory*' ($reg_1, \ldots, reg_{na} = 0$) of the digital filter. Therefore, the filter needs a *warm-up phase* to fill up all the registers, and especially for recursive filters to reproduce realistic filter values. If all the registers are filled in a proper way, the filter procedure generates for each new input value one filtered output value. The computational as well as the storage steps are included in this algorithm. The only thing we have to take care of are the first steps. Confer Sec. 2.2.4 for further discussions on the warm-up phases.

```
! Computational Step to compute ℓ̄[n]
ℓ̄[n] = b_0 ℓ[n] + reg_1
! Update Step to compute reg_i
DO i = 1, ..., #na − 1
    reg_i = b_i ℓ[n] + reg_{i+1} − a_i ℓ̄[n]
END DO i
reg_na = b_na ℓ[n] − a_na ℓ̄[n]
```

Algorithm 2.2.1: $\bar{\ell}[n] = FILTER(\ell[n])$; efficient filter implementation with minimized number of registers.

2.2.2 Cascaded Filter

As shown in the previous section any discrete linear filter can be represented in different ways. In Section 2.1.5 we show in equation (2.89) one form of the filter representation in the frequency domain. If we factorize the nominator and denominator we obtain the zero-pole-gain form

$$H(z) = \frac{(z-z_0)(z-z_1)(z-z_2)(z-z_3)\dots(z-z_{n_b})}{(z-p_0)(z-p_1)(z-p_2)(z-p_3)\dots(z-p_{n_a})} \tag{2.102}$$

with the zeros z_i and the poles p_i. In this form we can immediately split this filter into two lower order sections without changing the spectral behavior, e.g.

$$H(z) = \frac{(z-z_0)(z-z_1)(z-z_2)}{(z-p_0)(z-p_1)(z-p_2)} \quad \frac{(z-z_3)\dots(z-z_{n_b})}{(z-p_3)\dots(z-p_{n_a})}\,, \tag{2.103}$$

or in other words, we derive two sub-filters, which can be applied in a sequence (linearity!). Especially a sequence of second order filters (second-order sections) reflects

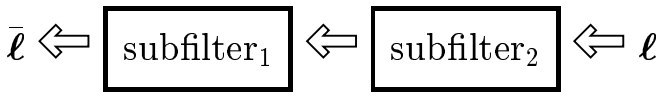

Figure 2.16 : Sequence of discrete filters.

on the one hand a numerically preferable behavior, and on the other hand, the design of these second order sections can be done very intuitively by positioning a conjugated pair of zeros and poles in the z-plane. Especially notch filters (filters with a narrow stop-band) can be constructed in an extremely simple way by a zero on the unit circle in the z-plane at the frequency that is to be suppressed (cf. e.g. *BUTTKUS (2000)[2]*, Sec. 18.2).

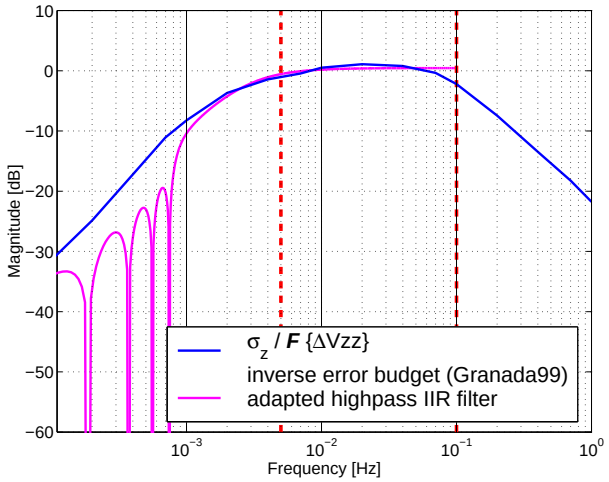

Figure 2.17 : Adapted filter; implemented by a high-pass filter in a cascaded sequence followed by four notch filters. These notch filters are constructed to eliminate the disturbances at the discrete frequencies 1 to 4 cycles per revolution (cpr).

A second-order sections representation arranges second order filters in a cascaded form providing advantages in designing the filters. Through careful pairing of the poles and zeros, ordering of the sections in the cascade, it is possible to reduce the quantization noise. Especially the *Delft-data-set* (cf. Sec. 2.3.1.1), but also some simulated GOCE error spectra (cf. Fig. 2.3), show some specific effects for 1 to 4 cycles per revolution (cpr). Therefore, we investigated special notch filters for these frequencies. If we try to model these phenomena in one filter with the order ten, numerical effects destroy the spectral behavior. Therefore, we introduce a cascade of second-order filters, which are able to handle this spectral behavior. By now the implementation of the cascade-filter in the `pcgma`-algorithm is finished and numerical simulations will be performed to study its behavior.

2.2.3 Computational Aspects

A frequency selective filter can be applied in the time domain (2.88) or in the frequency domain, where the measurements $\boldsymbol{\ell}$ are Fourier transformed and denoted as sample spectrum or periodogram $\mathcal{F}\{\boldsymbol{\ell}\}$, and the impulse response function $\boldsymbol{f}$ is transformed to the frequency response function $\mathcal{F}\{\boldsymbol{f}\}$. The convolution in the time domain degenerates to a simple multiplication in the frequency domain (cf. Fig. 2.7).

With regard to large adjustment problems, the time domain approach has the advantage that the filter process can be applied to data during acquisition. Therefore, a sequential adjustment procedure can be applied, which means that the contribution of each individual observation equation can be worked off sequentially. The typical operations, the computation of

$$\boldsymbol{N} = \bar{\boldsymbol{A}}^T \bar{\boldsymbol{A}}\ ,\ \boldsymbol{n} = \bar{\boldsymbol{A}}^T \bar{\boldsymbol{\ell}} \qquad \text{or} \qquad \boldsymbol{N} = (\boldsymbol{F}\boldsymbol{A})^T \boldsymbol{F}\boldsymbol{A}\ ,\ \boldsymbol{n} = (\boldsymbol{F}\boldsymbol{A})^T \boldsymbol{F}\boldsymbol{\ell} \tag{2.104}$$

using the direct solver, and the determination of the form

$$\boldsymbol{q} = \bar{\boldsymbol{A}}^T \bar{\boldsymbol{A}}\, \boldsymbol{p} \qquad \text{or} \qquad \boldsymbol{q} = \boldsymbol{A}^T \boldsymbol{F}^T \boldsymbol{F}\boldsymbol{A}\, \boldsymbol{p} \tag{2.105}$$

with respect to iterative solvers can be performed row-by-row, using each row $\boldsymbol{A}(k,:)$ of the design matrix $\boldsymbol{A}$ only once. This is important when we have in mind large and very large systems, making the storage of $\boldsymbol{A}$ as an entire matrix impossible and requiring the computation and processing to be done row-by-row.

The filter in the time domain (2.88) can be seen like a box (cf. Alg. 2.2.1), where within each step a new input value $\ell(n)$ produces an output value $\bar{\ell}(n)$. The box stores the coefficients, as well as some of the past results in a special memory-stack. Therefore, the operation s $\bar{\boldsymbol{\ell}} = \boldsymbol{F}\boldsymbol{\ell}$ can be performed step-by-step by a function call $\bar{\ell}(k) = FILTER(\ell(k))$. The same can be done with each column of the matrix $\boldsymbol{A}$ to compute the product $\bar{\boldsymbol{A}} = \boldsymbol{F}\boldsymbol{A}$, where a row-wise access yields $\bar{\boldsymbol{A}}(k,:) = FILTER(\boldsymbol{A}(k,:))$. Here, an array of filter-boxes is applied. Each column possesses its own filter-box using the same filter operators (coefficients), but each box is equipped with its own memory-stack (single instruction - multiple data). Each call of the filter operation produces a new result $\bar{\boldsymbol{A}}(k,:)$ and updates the memory-stack. Therefore, it is not necessary to filter the whole sequence at once, but this can be done individually, observation by observation, and allows to finalize all computations of one single observation. In particular, the two update steps to assemble the normal equation system can be performed within the same loop (cf. Alg. 2.2.2). After the filtering of the observation equation, the dyadic product of each observation is computed and added to the normal equations (*update-step*).

This strategy is very efficient, because within one loop through the observations all computations are done. To reduce the computational effort of filtering all columns of the matrix $\boldsymbol{A}$ (filter-array), a low order recursive filter is an ideal choice to represent the correlations of the measurement series. Fig. 2.18 summarizes the characteristics of an ARMA(2,2) filter, which is able to work as a pre-whitening filter for satellite gradiometry measurements (e.g. component ΔV_{zz}) with a power spectral density function given by Fig. 2.2. In the caption of Fig. 2.18 it is mentioned that the phase spectrum $\measuredangle(\omega)$ of this filter is not linear. Therefore, the group delay (the derivative of the phase spectrum) varies for different frequencies. This individual delay is absorbed during the assembling of the normal equations $\boldsymbol{A}^T \boldsymbol{F}^T \boldsymbol{F}\boldsymbol{A}$ by the operation $\boldsymbol{F}^T \boldsymbol{F}$. In matrix formulation the causality of the filter $\boldsymbol{F}$ is expressed by the lower triangular Toeplitz structure, because the matrix-vector operation $\bar{\boldsymbol{x}} = \boldsymbol{F}\boldsymbol{x}$ combines only elements $x(j)$, $j = 0, \ldots, k$ to compute $\bar{x}(k)$. In contrast, the matrix $\boldsymbol{F}^T$ reflects an anti-causal system, or in terms of filtering, a filter operation with a time-reversed sequence. The delay caused by the first filter operation is compensated by the second filter operation. This re-filtering is typically used to correct the phase shifts and to produce a zero-phase filter. Confer *KOCH (1994)[6]* or *BUTTKUS (2000)[2]*. From the computational aspect the cascaded filtering requires no additional effort if we assemble the normal equations $\bar{\boldsymbol{A}}^T \bar{\boldsymbol{A}}$ by dyadic products of the filtered rows. However, if a column-wise approach

```
! initialize filter array A
INIT_FILTER_A(A_row)
! initialize scalar filter ℓ
INIT_FILTER_ℓ(ℓ)
q = 0
n = 0

DO k = 1,...,#n_obs
   [A_row,ℓ] = COMPUTE_OBS(k)
   ! filter A_row column wise
   Ā_row = FILTER_A(A_row)
   ℓ̄     = FILTER_ℓ(ℓ)
   ! update N by a dyadic product
   N = N + Ā_row^T Ā_row
   ! update n by a scaled vector
   n = n + Ā_row^T ℓ̄
END DO k
```

```
! initialize scalar filter h
INIT_FILTER_h(h)
! initialize scalar filter h̄
! scalar filter
INIT_FILTER_h̄(h̄)
q = 0

DO k = 1,...,#n_obs
   A_row = COMPUTE_OBS(k)
   ! scalar product
   h = A_row • p
   ! filter scalar h
   h̄ = FILTER_h(h)
   ! filter scalar h̄
   h̿ = FILTER_h̄(h)
   ! update q by a scaled vector
   q = q + A_row^T h̿
END DO k
```

Algorithm 2.2.2: Efficient implementation of the filter for large design matrices $\boldsymbol{A}$. The computational steps to compute the normal equation $\boldsymbol{N} = (\boldsymbol{FA})^T(\boldsymbol{FA})$ shows the algorithm on the left. On the right an efficient algorithm to compute the form $\boldsymbol{q} = \boldsymbol{A}^T\boldsymbol{FFAp}$ is worked out. This form has to be computed during each iterative solution. The shape of the input vector $\boldsymbol{p}$ is used to reduce the computational steps by solving this product from the right to the left. In this case only scalar products, scalar filter operations and a scaled vector update are necessary. However, to preserve the sequential access to the observation equations, a symmetric filter operator $\boldsymbol{F}^T = \boldsymbol{F}$ is assumed.

is applied, we have to take care of the time-reversed ordering. Exactly this problem occurs during the iterative approach, because by computing (2.105) we want to take advantage of the shape of the vector $\boldsymbol{p}$. Therefore, we avoid matrix-matrix operations and prefer the following order of computation

$$\boldsymbol{q} = (\boldsymbol{A}^T(\boldsymbol{F}^T(\boldsymbol{F}(\boldsymbol{A}\,\boldsymbol{p})))) \;, \tag{2.106}$$

having in mind again a row-by-row approach of the matrix $\boldsymbol{A}$. A problem arises with the time-reversed second filter process, because $(\boldsymbol{F}(\boldsymbol{A}(k,:)\,\boldsymbol{p}))$ produces for each row k of $\boldsymbol{A}$ one filtered value $h(k)$. Sure enough, we can collect these values and perform the second filter operation with the reversed sequence, but then we have to recompute the matrix $\boldsymbol{A}$ to finish the computations of (2.106). A way out of this dilemma arises through the usage of a finite impulse response filter. The matrix representation $\boldsymbol{F}$ becomes a banded lower triangular structure and, therefore, the filter operation is degenerated from the whole sequence to a finite number observations. In addition, we can take advantage of symmetric transversal moving average filters (see Fig. 2.18), for which the direction of filtering is irrelevant. This fact is reflected by the property that

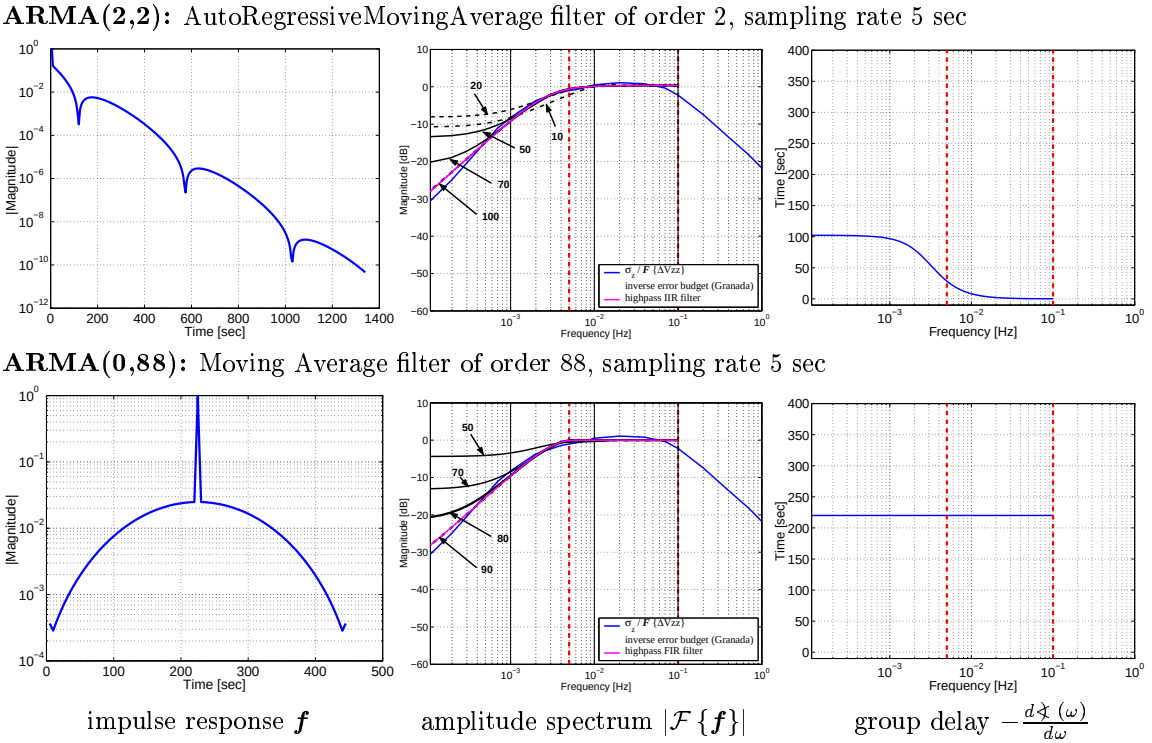

Figure 2.18: Characteristics of an **A**uto**R**egressive**M**oving**A**verage filter of the order 2 (ARMA(2,2)) and a **M**oving**A**verage filter of the order 88 (ARMA(0,88)). The upper (lower) left figure shows the infinite (finite) impulse response of the filter. In the middle the amplitude spectra reflect the spectral behavior with respect to the inverse error budget of the gradiometer measurements (component ΔV_{zz}). Special attention is paid to the warm-up phase of the filter. The curves after $10, 20, \ldots, 90$ samples reflect the boundary condition and, therefore, the fill up of the intern memory of the filter-box. On the right the deviation of the phase spectrum $\measuredangle(\omega)$ with respect to the frequency ω - the group delay - of the filter gives an impression of the delay in units of time with regard to individual frequencies. The upper figure shows that different frequencies use varying times to be transported through the filter. It takes the low frequencies 100 *sec* (20 samples) to penetrate the filter and high frequencies pass the filter without delay. In contrast to this frequency dependent delay the MA-filter (see low right diagram) shows a constant delay (220 *sec*, 44 samples) for all frequencies.

all the frequencies have a constant delay, which can be easily handled by a constant time shift applied to the entire sequence. This approach enables a very efficient computation of (2.106), avoiding the filtering of all columns of the design matrix $\boldsymbol{A}$, because only the vectors $\boldsymbol{h} = \boldsymbol{A}\boldsymbol{p}$ and $\bar{\boldsymbol{h}} = \boldsymbol{F}\boldsymbol{h}$ have to be filtered element-by-element. The update step of the vector $\boldsymbol{q}$ can be performed by

$$\boldsymbol{q}^{(k)} = \boldsymbol{q}^{(k-1)} + \boldsymbol{A}(k,:)^T \text{FILTER\_}\bar{\text{h}}(\text{FILTER\_h}(\boldsymbol{A}(k,:)\ \boldsymbol{p}))\ , \tag{2.107}$$

with the initial condition $\boldsymbol{q}^{(0)} = \boldsymbol{0}$. This update step where $\boldsymbol{A}(k,:)$ denotes the k^{th} row of the design matrix requires only a single pass $k = 1, \ldots, \#n\_obs$ through the design matrix $\boldsymbol{A}$ row-by-row. The two filter operations act on scalars, because they are applied to sequences of scalar values.

2.2.4 Warm-up Phases

One nice additional property of the finite impulse response filters is the direct access to the behavior in boundary regions. The warm-up phase at the very beginning of a sequence or in case of a data gap can be immediately deduced from the support of the finite impulse response. For shorter time periods the spectral behavior is given by the Fourier transform of the truncated impulse response. Fig. 2.18 shows this warm-up behavior. The amplitude spectra for both mentioned filters reflect a warm-up time of about 90 samples (450 *sec*) to reproduce the spectral behavior of the gradiometer measurements. Right from the beginning especially low frequencies are disturbed and, therefore, a warm-up phase is necessary to fill the memories of the filter-box appropriately.

2.3 Elaboration of a test scenario to evaluate the quality of SGG products

2.3.1 Elaboration of test data sets

In order to demonstrate the performance of the different approaches, we generate test data sets with the intention to simulate the noise characteristics as realistically as possible. In this section we describe two different strategies to generate random variables with a specific spectral behavior. On the one hand, a harmonic random process simulates a periodic behavior with a discrete spectrum, while on the other hand, a general linear process generates a non-periodic noise with a purely continuous spectrum. In reality, a combination of both effects, periodic and non-periodic, will degrade the measurement signal.

Concerning the satellite mission GOCE the error budget of the gradiometer output was studied (cf.. *ESA (1999)[3]*), and the spectral behavior of the measurements is given in terms of the power spectral density curves (cf. Fig. 2.2).

Based on this spectral information, test data sets are generated to study the performance of different solution strategies. In the frame of the ESA study *ESA (2000)[4]* the so-called *Delft-data-set* was generated by SID/DEOS (cf. *ESA (2000)[4]*, pp. 63-66 and pp. 138-141). The simulated measurements (three main diagonal elements of the gradient tensor) are regularly distributed along the orbit with a sampling interval of 5 s. The simulated orbit is a sun-synchronous, 29-days repeat orbit, with an inclination of $i = 96.6°$ and an altitude of approximately 250 km. The colored noise is generated by a random harmonic process. As an example, Fig. 2.19 shows the statistical behavior of the radial component ΔV_{zz} of this data set, which demonstrates the specific property of a harmonic process, i.e. a periodic behavior of the signal, and a non-decreasing periodic covariance function. The Fourier analysis of the data reflects also the discrete characteristic of the the power spectra. On the basis of the same orbit data a second

data set is generated, where the colored noise is simulated by an ARMA filter process. We use the filter coefficients described in detail in *ESA (2000)[4]*, pp. 155-157, and change the numerator and denominator of the frequency response function, which means an interchange of the zeros with the poles. In order to stabilize the behavior, we additionally introduce a stop band filter for zero and extremely low frequencies. Fig. 2.20 shows the statistical behavior of this data set, which is denoted in this article as *ARMA-data-set*.

2.3.1.1 Delft-Data-Set

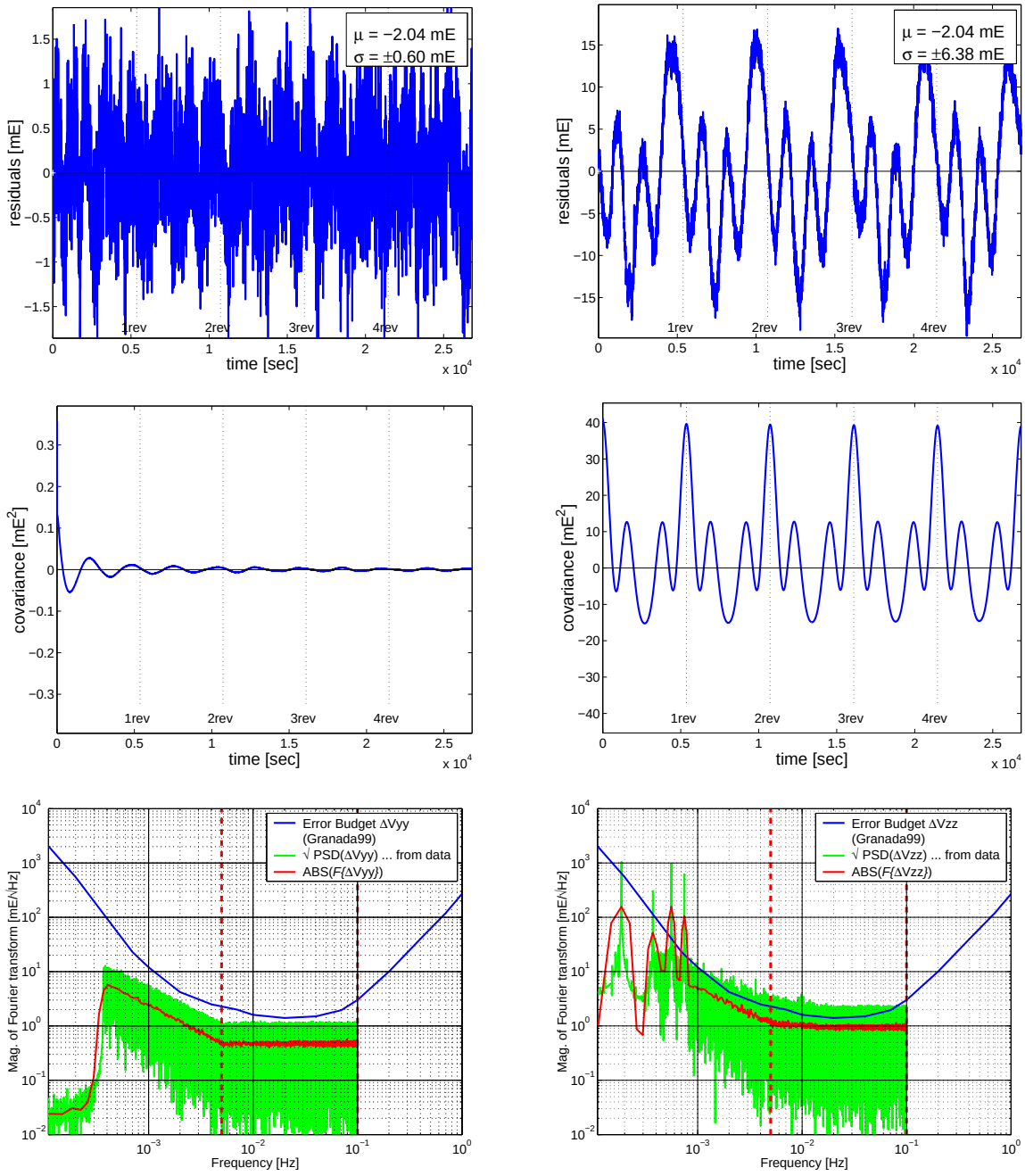

Figure 2.19: Periodic colored noise generated by a harmonic random process.
left hand side: ΔV_{yy} right hand side: ΔV_{zz}
top: signals
middle: empirical covariance function
bottom: periodogram and power spectrum density

2.3.1.2 ARMA-Data-Set

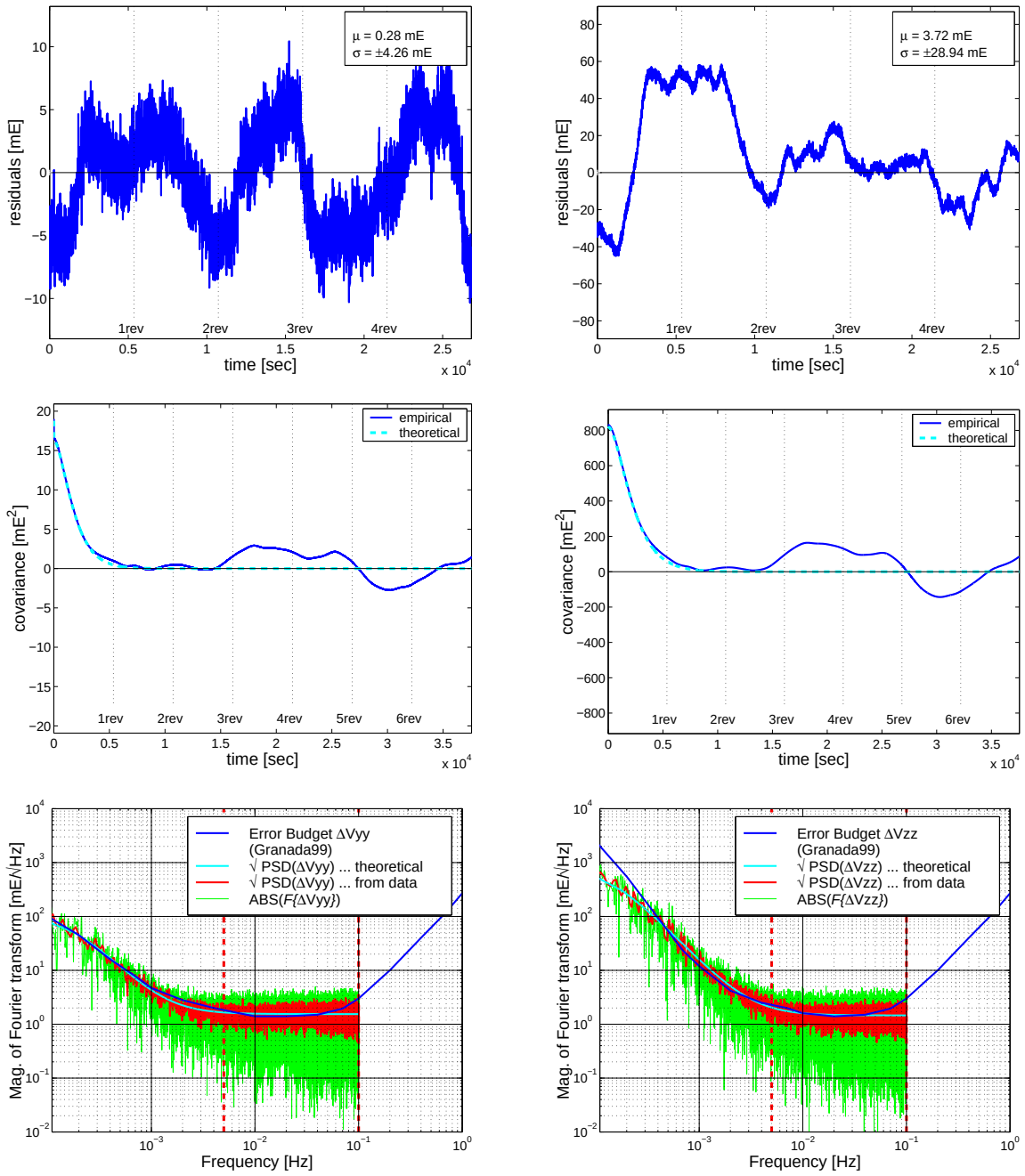

Figure 2.20: Non-periodic colored noise generated by an ARMA-processes.
left hand side: ΔV_{yy} right hand side: ΔV_{zz}
top: signals
middle: empirical covariance function
bottom: periodogram and power spectrum density

2.3.2 Simulations - Closed-Loop-Computations

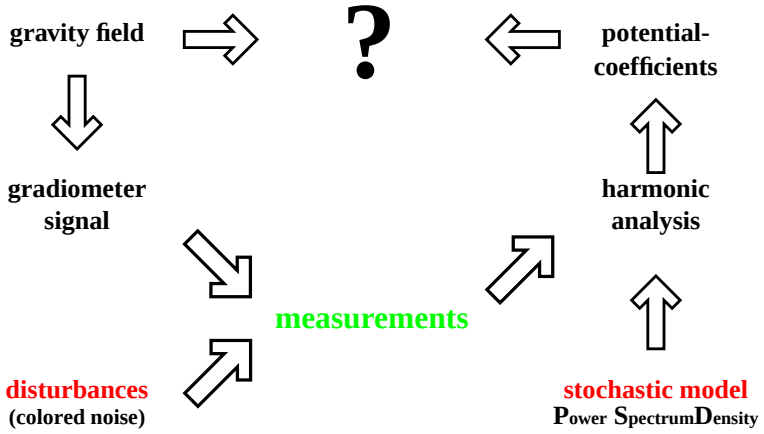

Figure 2.21 : Closed-Loop Simulation; from an a priori known gravity field, parameterized by spherical harmonic coefficients, two data sets are deduced. On the one hand the geoid heights on a regular grid are computed as reference field. On the other hand the observation functionals are determined with respect to a realistic satellite orbit. These functionals are superposed by a colored noise and form the measurement series. This sequence is used together with the stochastic model as input to the spherical harmonic analysis procedure. The adjustment approach leads again to a set of spherical harmonic coefficients. These coefficients are compared with the a priori known coefficients in two ways. First the corresponding coefficients are directly confronted and second the re-computed geoid heights are compared with the original ones. The second comparison is very sensitive to an energy shift between the spherical harmonic coefficients of different degrees, because of the downward continuation and integration process.

This closed loop simulation is based on a data set from a 29 days sun-synchronous repeat orbit with an initial altitude of about 250 km, measuring the three main diagonal elements of the gradient tensor (radial, along track, across track) with a sampling period of 5 s. This results in more than 1.5 million observations containing information about the Earth's gravity field up to degree and order 180 (based on the Earth model OSU91a), superposed by a noise model generated by a harmonic random process (cf. Fig. 2.19) or an ARMA process (cf. Fig. 2.20) as described in the previous Sec. 2.1.4 and 2.1.5.

Within all our simulations we can not detect a significant difference in the solution behavior using the different noise models. Consequently, in the following documentation we concentrate on the *ARMA-data-set*.

2.3.2.1 Lumped Coefficients vs. Direct Approach

The gravitational potential of the Earth is parameterized by a truncated harmonic series expansion in spherical coordinates (r, ϕ, λ)

$$f^{s_t}(\phi,\lambda,r) = \frac{GM}{r}\left\{1+\sum_{\ell=2}^{\ell_{max}}\sum_{m=0}^{\ell}\left(\frac{R}{r}\right)^{\ell}\bar{P}_{\ell m}(\sin\phi)\left(\bar{C}_{\ell m}\cos m\lambda+\bar{S}_{\ell m}\sin m\lambda\right)\right\}. \quad (2.108)$$

G, M and R are the gravitational constant, the Earth's mass and the Earth's reference radius, respectively, while $\bar{P}_{lm}$ denotes the fully normalized Legendre polynomials depending on the harmonic degree ℓ and order m.

The goal is now to determine the corresponding harmonic coefficients $\bar{C}_{lm}$ and $\bar{S}_{lm}$ as accurately as possible.

The dedicated gravity gradiometry mission GOCE will deliver essentially two types of measurements: GPS satellite-to-satellite tracking (SST) data reflecting orbit perturbations and representing first order derivatives of the gravitational potential, as well as gravity gradients (SGG) measured by the 3-axes gravity gradiometer representing second order derivatives. In the present paper we will concentrate on the latter measurement type.

Gathering all the second order derivatives with respect to the main directions (radial, along track, across track) in an observation vector $\boldsymbol{\ell}$ and the corresponding error covariances in the matrix $\boldsymbol{\Sigma}$, using a standard Gauss-Markov model and applying the best linear uniformly unbiased estimation with respect to the $\boldsymbol{\Sigma}^{-1}$-norm leads to the normal equation system

$$(\boldsymbol{A}^T\boldsymbol{\Sigma}^{-1}\boldsymbol{A})\,\tilde{\boldsymbol{x}} = \boldsymbol{A}^T\boldsymbol{\Sigma}^{-1}\boldsymbol{\ell} \quad (2.109)$$

for the parameter vector $\tilde{\boldsymbol{x}} = \{\bar{C}_{lm};\bar{S}_{lm}\}$, where the design matrix $\boldsymbol{A}$ represents the linear (or linearized) relation between observations $\boldsymbol{\ell}$ and the parameters $\boldsymbol{x}$ and thus contains the base functions of the series expansion (2.108). This approach, is in principle applied by all *direct methods* to solve for the coefficients.

Due to the fact that measurements taken along a satellite's track are not homogeneously distributed with respect to the spatial domain of the sphere, the orthogonality properties of the base functions are lost, and thus the normal equation matrix $\boldsymbol{A}^T\boldsymbol{\Sigma}^{-1}\boldsymbol{A}$ is a dense matrix. However, if the gravity gradients are uninterruptedly measured with constant step size along a circular repeat orbit, it can be shown that all coefficients of different orders m as well as *cos*- and *sin*-related coefficients become uncorrelated, leading to a block-diagonal structure of the equation system (cf. *SNEEUW (2000)[11]*).

In reality, these simplifying conditions will not be strictly fulfilled, and, consequently, the normal equation system will deviate from the block-diagonal structure. However, due to the large number of unknown parameters and thus also the huge dimension of the normal equation system $\boldsymbol{A}^T\boldsymbol{\Sigma}^{-1}\boldsymbol{A}$ (about 90000 unknowns for a maximum resolution of $l_{max} = 300$, corresponding to 70 km half wavelength), the system can not be directly inverted.

Therefore, for the processing of real mission data the *direct method* was implemented in terms of the `pcgma` (**P**reconditioned **C**onjugate **G**radient **M**ultiple **A**djustment) algorithm (cf. *SCHUH (1996)[12]*), using a block-diagonal preconditioner $(\boldsymbol{A}^T\boldsymbol{\Sigma}^{-1}\boldsymbol{A})_{\oplus}$ as a first guess (initialization step) and applying iteratively a conjugate gradient method to successively improve the parameter estimates.

While in the *direct method* the observations are regarded as functions of the geographical location (r, θ, λ), they can also be considered as a periodic time series for one repeat period (cf. *RUMMEL et al. (1993)[10]*, *SNEEUW (2000)[11]*). Assuming a circular orbit, (2.108) can be rewritten as

$$f^{s_t} = \frac{GM}{R} \sum_l \left(\frac{R}{r}\right)^{l+1} \sum_m \sum_k \bar{F}^k_{lm}(i)[\alpha_{lm} \cos \psi_{km}(t) + \beta_{lm} \sin \psi_{km}(t)] \tag{2.110}$$

with $\bar{F}^k_{lm}(i)$ denoting the inclination function which depends on the orbit inclination i, and the coefficients α_{lm}, β_{lm} related to the harmonic coefficients $\bar{C}_{lm}$, $\bar{S}_{lm}$. Abbreviating

$$\left\{ \begin{array}{c} A_{km} \\ B_{km} \end{array} \right\} = \frac{GM}{R} \sum_l \left(\frac{R}{r}\right)^{l+1} \bar{F}^k_{lm}(i) \left\{ \begin{array}{c} \alpha_{lm} \\ \beta_{lm} \end{array} \right\} , \tag{2.111}$$

(2.110) is a Fourier series

$$f^{s_t} = \sum_m \sum_k [A_{km} \cos \psi_{km}(t) + B_{km} \sin \psi_{km}(t)] \tag{2.112}$$

where $\psi_{km}(t)$ is related to two fundamental frequencies ω_o (orbit revolution) and ω_e (Earth's rotation).

In this *time-wise approach* (also frequently denoted as *semi-analytic approach*) in the first step the Fourier coefficients ('lumped coefficients') A_{km}, B_{km} are computed by FFT methods, and in the second step the harmonic coefficients $\bar{C}_{lm}$, $\bar{S}_{lm}$ are estimated order by order, assuming strict block-diagonal structure of the system. The deviations from this property are incorporated by means of an iterative procedure.

2.3.2.2 Comparison

The *direct method* as well as the *semi-analytic approach* were applied to estimate the set of 32757 coefficients describing the Earth's gravity field up to a spatial resolution of about 110 km half wavelength. Due to the fact that the input data set is based on a realistic, perturbed orbit, both methods have to apply an iterative solution strategy, computing 15 iterations for each approach.

Fig. 2.22 shows the deviations of the estimated coefficients from the initial 'exact' OSU91a-model in terms of a degree rms

$$\sigma_l = \sqrt{\frac{1}{2\,l+1} \sum_{m=0}^{l} [(\bar{C}^{(est)}_{lm} - \bar{C}^{(OSU)}_{lm})^2 + (\bar{S}^{(est)}_{lm} - \bar{S}^{(OSU)}_{lm})^2]} \, . \tag{2.113}$$

Except for a slightly differing convergence behavior, it can be stated that both methods reach the final solution after four or five iterations, and that both results are nearly identical. This statement is underlined by Fig. 2.23, which illustrates the absolute deviations of the coefficient estimates from the true values. Due to the polar gap problem (no observations are made in the polar regions because of the sun-synchronous orbit design), the zonal and near-zonal coefficients ($m < 10$) are resolved worst.

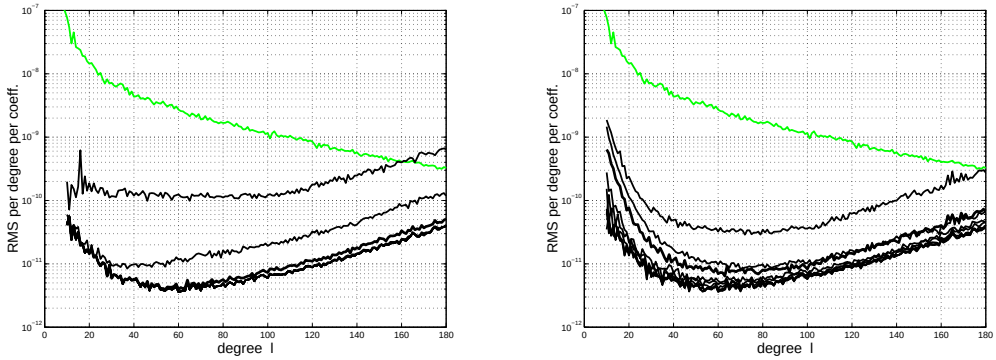

Figure 2.22 : *ARMA-data-set* ($\ell_{max} = 180$); convergence behavior:
Semi-analytic approach (left) versus *direct method* (right). Gray line: Spectrum OSU91a, black lines: Differences between exact and iterative solutions σ_l as defined by (2.113).

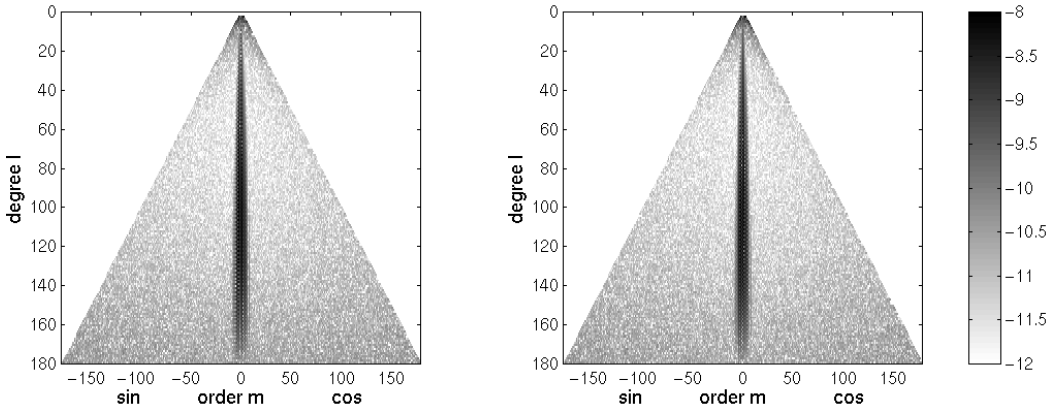

Figure 2.23 : *ARMA-data-set* ($\ell_{max} = 180$); Spectral triangles:
Semi-analytic approach (left) versus *direct method* (right). Deviations of coefficients after the 15. iteration from exact solution. Plotted is $log_{10}(|\ldots|)$.

The quality of the solutions can also be compared in terms of second level products such as geoid heights, thus closing the loop of our simulation strategy. Fig. 2.24 shows the absolute geoid height deviations in [m] of the *semi-analytic approach* (left) and the *direct method* solution (right) after the 15. iteration. In the first row we compare the global solution. Although the actual error structures are different, they have the same order of magnitude for both approaches. But it should be mentioned here, that due to the filter characteristics the long wavelength structure of the Earth's gravity field is only badly determined by the SGG-only-models. Therefore, the global deviations are strongly influenced by the initial state conditions of the filters, the actual realization of the colored noise at the begin of the sequence and the warm-up strategy. All these influences have a random character and cause different global results, but don't allow a scientific interpretation of these random results.

In the second row we illustrate a regional solution for the equiangular test area 10° W to 55° E in longitude and 10° N to 65° N in latitude. The global trend was removed

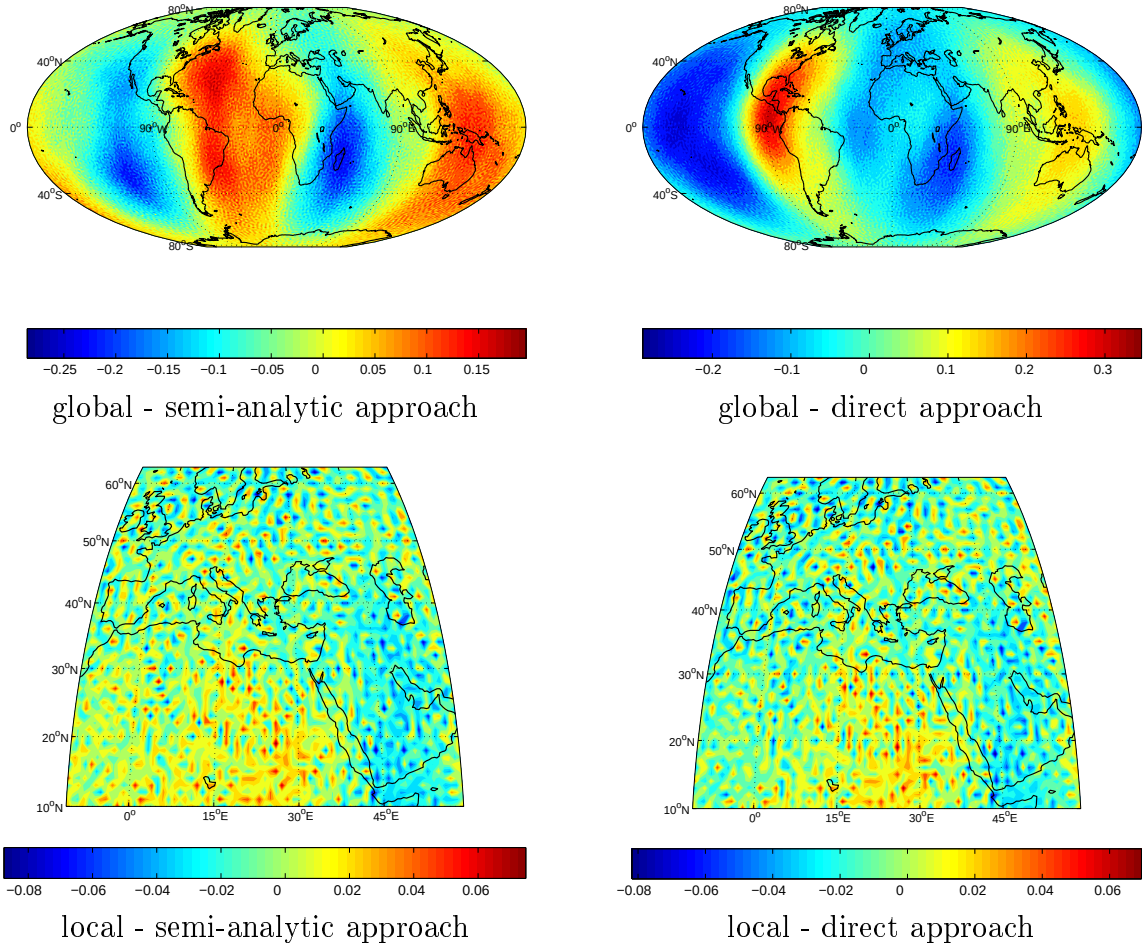

Figure 2.24: *ARMA-data-set* ($l_{max} = 180$);
Reconstruction of second level information on a $1° \times 1°$ grid; geoid heights [m]: Comparison *semi-analytic approach* versus *direct method* (both after 15 iterations). Beside the global behavior the local approaches show the capability to reconstruct the high frequency behavior. For the local representation the data are reduced by a moving average ($30° \times 30°$).

subtracting a trend field which was generated applying a simple $30° \times 30°$ moving average filter. Reducing the long-wavelength errors, the two regional approaches show the capability to reconstruct the high frequency behavior.

Table 2.1 summarizes some statistical parameters of the geoid height difference fields for the two approaches after the 5^{th} and 15^{th} iteration, respectively.

The only significant difference between the two approaches occurs in the first iterations (cf. 5^{th} iteration) for the global solution, which can be explained by a worse convergence behavior of the `pcgma` with respect to the long wavelengths and low order coefficients (cf. Fig.2.22). On the other hand it should be mentioned that due to the filtering the long wavelengths are determined very badly. Therefore, the choice of the initial conditions and the intrinsic noise components at the beginning of the sequence influence

5 iterations	global		$-83° \leq \phi \leq 83°$		local			
	min	max	min	max	min	max	mean	σ
semi-analytic approach	-64	67	-0.283	0.228	-0.088	0.086	-0.001	0.025
direct approach	-10825	12616	-5.917	2.722	-0.106	0.147	0.008	0.037
15 iterations	global		$-83° \leq \phi \leq 83°$		local			
	min	max	min	max	min	max	mean	σ
semi-analytic approach	-63	67	-0.285	0.228	-0.088	0.086	-0.001	0.025
direct approach	-69	87	-0.289	0.389	-0.082	0.079	-0.003	0.024

Table 2.1: *ARMA-data-set* ($\ell_{max} = 180$);
Reconstruction of second level information on a $1° \times 1°$ grid; geoid heights [m]: Numerical comparison *semi-analytic approach* versus *direct approach* (both after 15 iterations). Beside the global behavior (incl.and excl.polar regions) the two local results demonstrate the capability to reconstruct the high frequent behavior. For the local representation the data are reduced by a moving average ($30° \times 30°$). The values characterize the differences between the geoid heights computed and the a priori OSU91a model with respect to the reconstructed Earth model. All differences are expressed in [m].

	global		$-83° \leq \phi \leq 83°$		local				
	min	max	min	max	min	max	mean	σ	
semi-analytic approach	-143	91	-0.823	0.862	-0.138	0.118	-0.038	0.069	MA
					-0.041	0.045	0.001	0.013	2MA
direct approach	-62	65	-0.796	0.884	-0.135	0.125	-0.037	0.069	MA
					-0.042	0.044	0.001	0.012	2MA

Table 2.2: *Delft-data-set* ($\ell_{max} = 180$);
Reconstruction of second level information on a $1° \times 1°$ grid; geoid heights [m]:
Numerical comparison *semi-analytic approach* versus *direct approach* (both after 15 iterations). Beside the global behavior (incl.and excl.polar regions) the two local approaches show the capability to reconstruct the high frequent behavior. For the first local representation the data are reduced by a moving average ($30° \times 30°$). The second local representation the moving average ($20° \times 30°$) process is used twice to reduce all global effects. The values characterize the differences between the geoid heights computed and the a priori OSU91a model with respect to the reconstructed Earth model. All differences are expressed in [m].

the global behavior extraordinarily, because this information mainly determines the global behavior. The solution with the Granada noise characteristic (cf. Fig.2.2) reflects no information or only very weak information on the long wavelength part. The realized solutions vary nearly randomly because no information can be deduced.

For the sake of completeness also the results of the simulations with respect to the Delft-Data set are illustrated (cf. Fig. 2.25 and Table 2.2).

Again, both solution strategies produce nearly identical results. The only difference compared to the *ARMA-data-set* is due to the effect that this periodic model involves

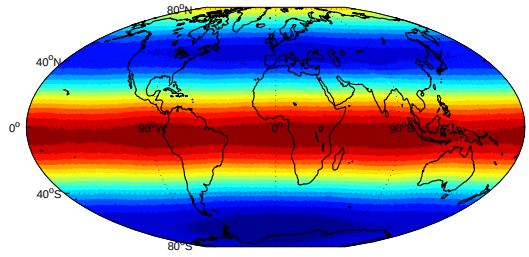

global - semi-analytic approach

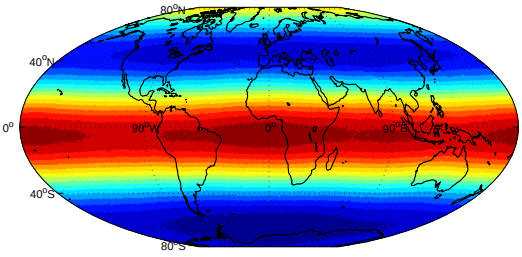

global - direct approach

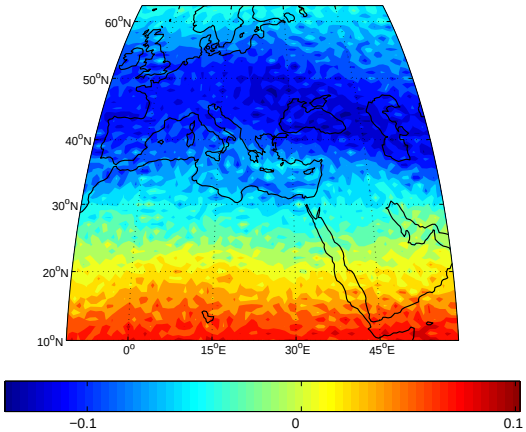

local (MA) - semi-analytic approach

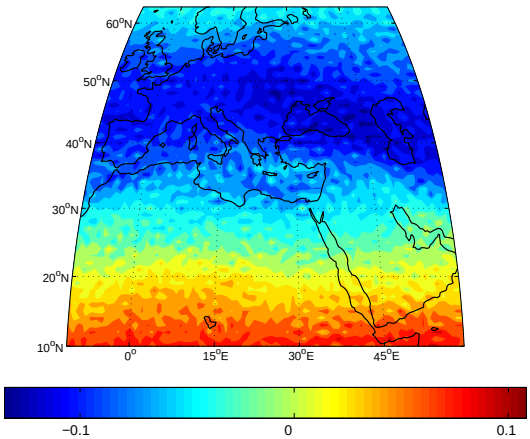

local (MA) - direct approach

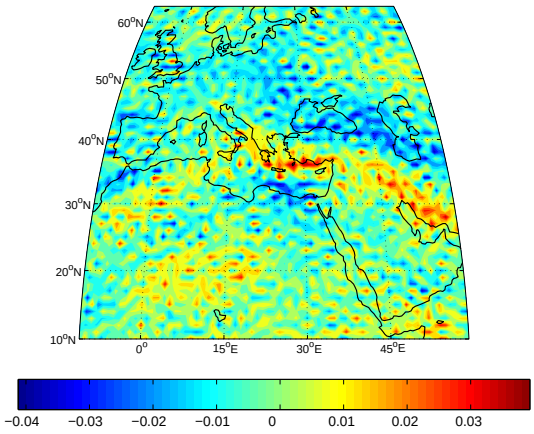

local (2MA) - semi-analytic approach

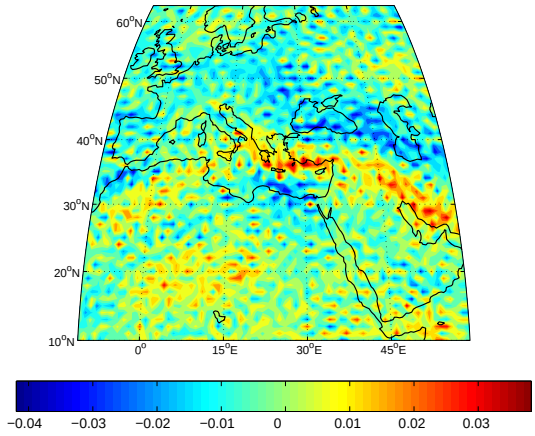

local (2MA) - direct approach

Figure 2.25: *Delft-data-set* ($\ell_{max} = 180$);
Reconstruction of second level information on a $1° \times 1°$ grid; geoid heights [m]: Comparison *semi-analytic approach* versus *direct approach* (both after 15 iterations). Beside the global behavior the two local approaches show the capability to reconstruct the high frequent behavior. For the first local representation the data are reduced by a moving average ($30° \times 30°$). The second local representation the moving average ($20° \times 30°$) process is used twice to reduce all global effects.

large disturbances in the frequency range from one to four cycles per revolution. Therefore, an additional moving average process is necessary to eliminate this global effect. Confer above discussion about global effects.

2.3.2.3 Discussion

The results discussed in the previous section demonstrate that two completely different and independent solution strategies, i.e. the *direct method* implemented in terms of the `pcgma` algorithm, as well as the *time-wise (semi-analytic) approach*, lead to essentially identical results, and it is shown that both methods can handle periodic and non-periodic random processes as well.

The major conceptual difference lies in the treatment of the system in the space versus time/frequency domain, respectively, which is directly linked to a different incorporation of the colored measuring noise and the implementation of filters. While the *direct method* computes a convolution of the impulse response function in space domain, the *semi-analytic approach* provides a more direct access to the frequency characteristics of the gradiometer, which can be mathematically expressed by a simple multiplication in frequency domain. From the point of view of computational effort, the semi-analytic approach is much cheaper, resulting in a faster recovery of the coefficient estimates, but with the same order of accuracy. However, some restricting conditions concerning the orbit design and the continuity of the data stream have to be fulfilled to apply the *semi-analytic approach*, while all such phenomena directly related to the space domain such as data gaps are easier to cope with applying a *direct method*.

2.3.3 Investigations with respect to spectral leakage effects

The dedicated satellite mission will provide large data volumes for the determination of the Earth's gravity field. Nevertheless, the large but finite discrete set of measurements cannot resolve all the details (frequencies) of the gravity field. Moreover, the data distribution is irregular due to data gaps in the polar regions and due to data concentrations particularly along rims surrounding the polar caps. As a consequence, a discrete spectral analysis of the Earth's gravity field has to deal with spectral leakage effects.

Standard signal processing tools provide numerous techniques for the filtering of the special frequencies. These tools are based on regularly distributed data, but fail on inhomogeneously distributed data sets. Simplified examples (test environment) are developed (cf. *WASLE et al. (2000)[17]* and *WASLE (2001)[18]*) to enhance the understanding of leakage effects in the framework of spherical harmonic analysis. This test environment allows now to study the properties of different (deterministic, stochastic, regularization) strategies to minimize leakage effects.

The theoretical investigations result in two statements:

- The leakage effect influences the whole spectral behavior and disturbs all frequencies. Therefore, a frequency selective filter can reduce this effect by filtering out frequencies from the data set, but cannot eliminate the effect for low frequencies.
- One method to eliminate the spectral leakage effect is an orthogonalization procedure due to the data distribution. This procedure is numerically extremely expensive and it is impossible to solve this approach in the case of GOCE in a strict way. But with some simplifications we can use a scaling procedure (re-weighting) to reduce the leakage effect. Unfortunately, this scaling procedure results in time dependent filter coefficients and, therefore, it requires further investigations to include this strategy into the solution algorithms.

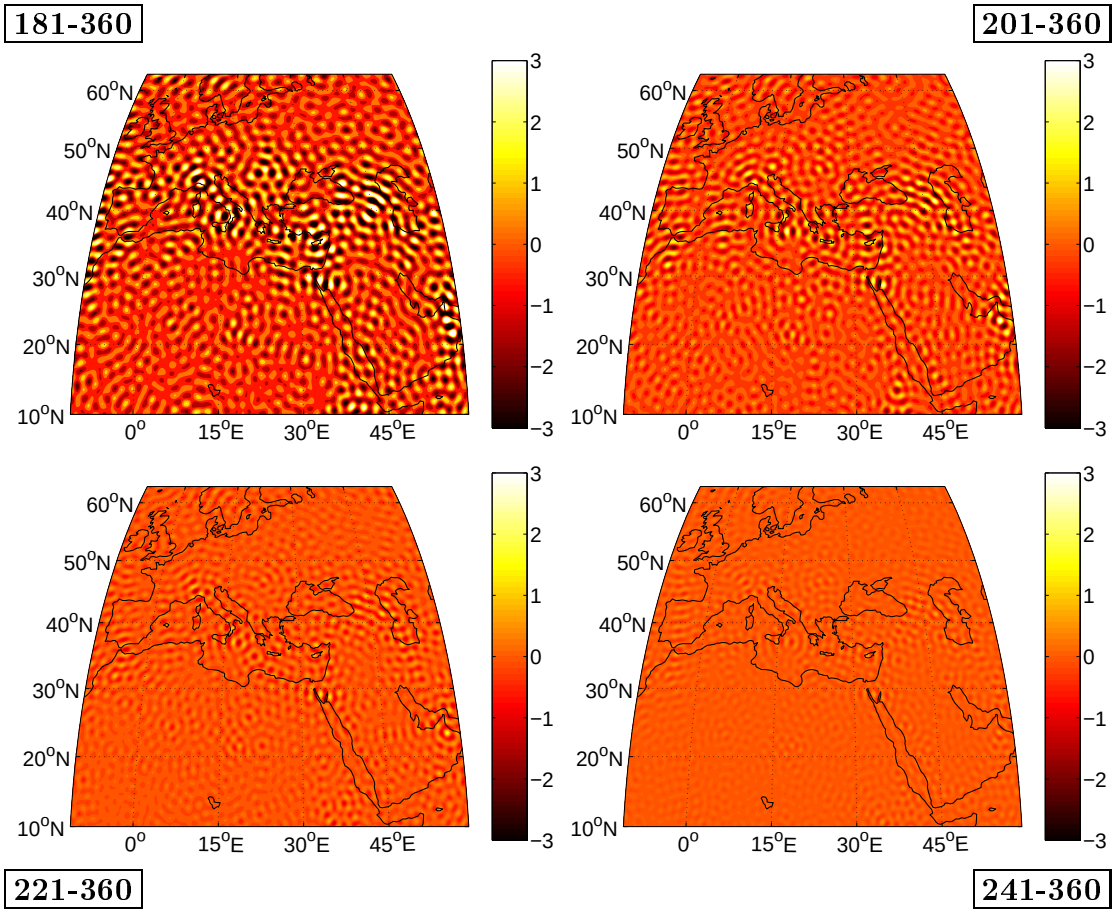

Figure 2.26: Contents of the high frequency part of the OSU91a model with respect to the T_{zz} component in satellite altitude of $250\,km$. All figures share the same scale from $-3\,mE$ to $+3\,mE$. The maximal signal varies between $\pm 6\,mE$ for the range between 181 and 360 to $\pm 0.6\,mE$ in the range between 241 and 360.

Nevertheless, we generate a test data set, where the components of the Earth's gravity field up to degree and order 360 are included in the signal. In the first simulation

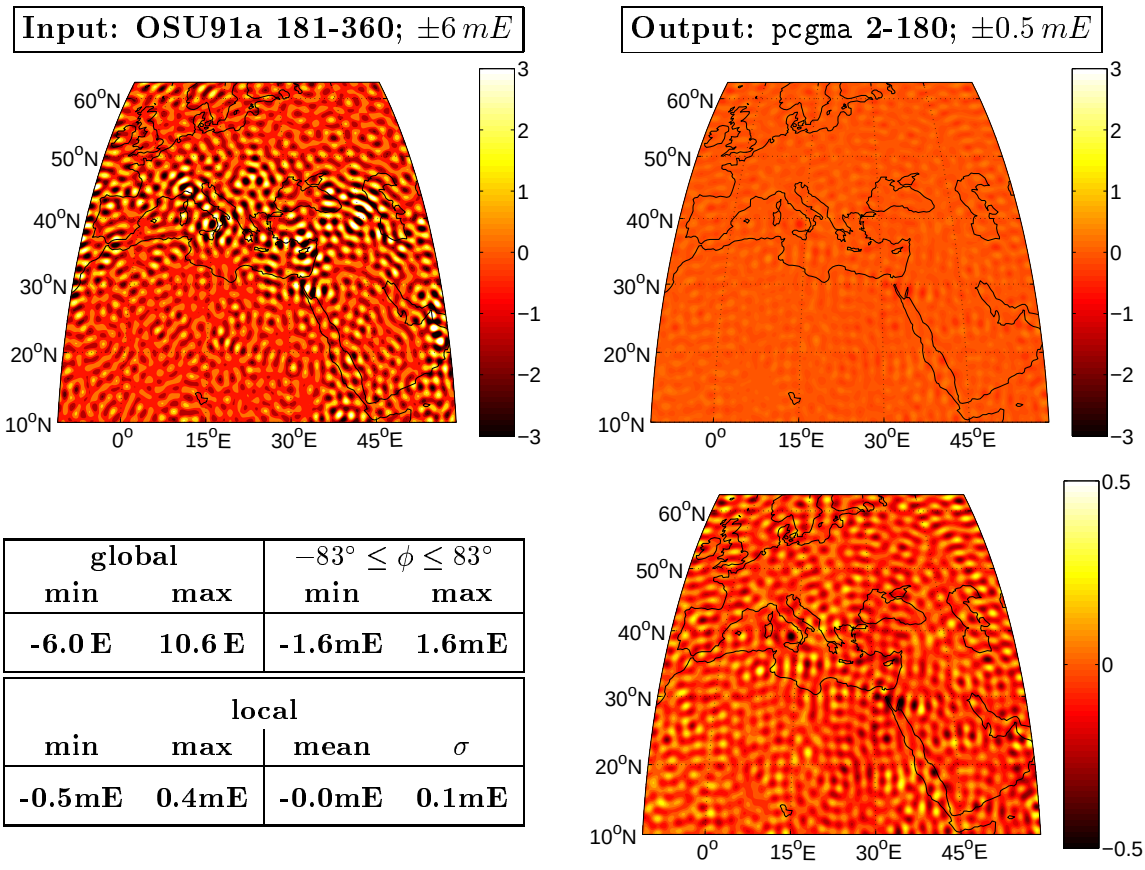

global		$-83° \leq \phi \leq 83°$	
min	**max**	**min**	**max**
-6.0 E	**10.6 E**	**-1.6mE**	**1.6mE**

local			
min	**max**	**mean**	σ
-0.5mE	**0.4mE**	**-0.0mE**	**0.1mE**

Figure 2.27: Spectral Leakage Effects; Reconstruction of the tensor component T_{zz} [mE] on a $0.25° \times 0.25°$ regular grid:
Spherical harmonic analysis up to degree 180 with the high frequence part of the OSU91a model (degrees 181-360) as input signal. In the upper row the input signal and the output signal are plotted with the same colorbar $\pm 3\,mE$, which is in the range of the measurement accuracy. The table summarizes the statistics of the `pcgma` output filed. The lower right figure plots the output signal in an adequate range. Only 10% of the input signal is absorbed by the adjustment procedure.

we study the pure leakage effect. In the next step also a colored noise (ARMA) is superimposed to the signal.

In Fig. 2.26 the gradiometer signal at satellite altitude of 250 km for the high frequency part of the OSU91a model is plotted. It can be seen that the gravity field information becomes smaller and smaller due to the smoothing effect with respect to satellite altitude. The effects induced by the contents of the degree 181 to 360 are in the range of $\pm 6\,mE$ and decrease to $\pm 3\,mE$ (201-360), $\pm 1.5\,mE$ (221-360) and $\pm 0.6\,mE$ (241-360). The last values are below the measurement noise of $\pm 3\,mE$ (or $\pm .8\,mE$ cf. *ESA (1999)[3]*) . Therefore, we can not expect to be able to deduce high frequency (>240 degree) information from the SGG measurements. All the internal variance studies reflect this behavior. If we look, for example, to Fig. 2.31 or Fig. 2.39 it can be seen that the accuracy of the coefficients for high degrees have the same size as the infor-

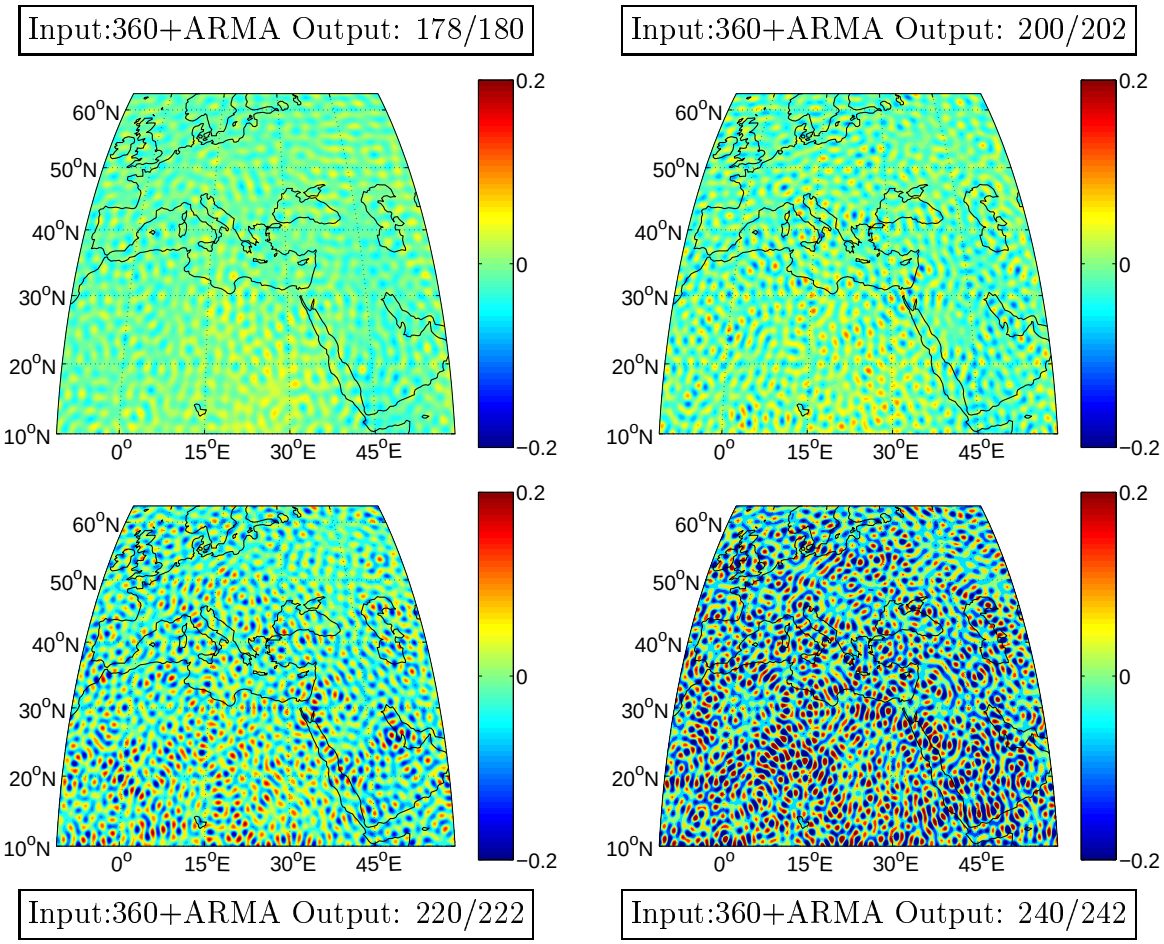

Figure 2.28: Spectral Leakage Effects; Reconstruction of second level information on a $0.25° \times 0.25°$ grid; geoid heights [m]:
The OSU91a signals up to degree 360 superimposed by an ARMA noise are reconstructed by a spherical harmonic analysis up to degree 180, 202, 222, and 242. The table summarizes the residuals of the geoid height differences in [m], where the last two degrees are used as puffer zone. The identifier (178/180/360) characterizes these quantities. 360 denotes the maximal involved frequency in the signal. The number of reconstructed frequencies is 180. The truncated model 178 is compared with the 178 true model. To reduce the global weakness of the solution the data are reduced by a moving average ($30° \times 30°$).

signal: 360+ARMA	local [m] min	max	mean	σ
model 178/180/360	-0.092	0.079	-0.002	0.021
model 200/202/360	-0.131	0.137	-0.002	0.034
model 220/222/360	-0.265	0.254	-0.002	0.059
model 240/242/360	-0.528	0.531	-0.002	0.108

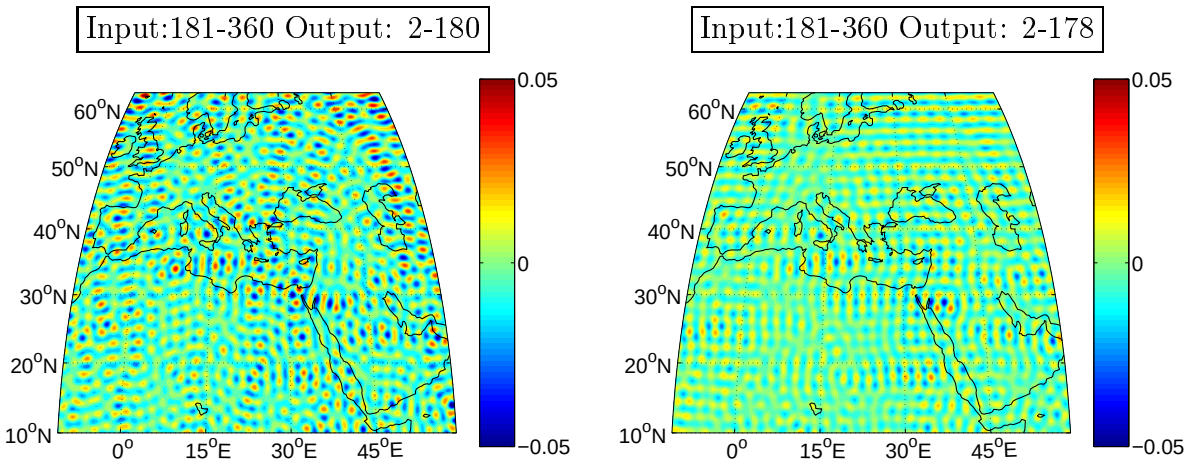

Figure 2.29 : Spectral Leakage Effects; Reconstruction of second level information on a $0.25° \times 0.25°$ grid; geoid heights [m]:
This simulation shows the truncation effect of the spherical harmonic series. The input signal consists only of the truncated signal for degree 181 to 360. The reconstruction of the geoid heights on a $0.25° \times 0.25°$ grid yields that a part of the signal is occupied by lower frequencies. The two figures show that most of the signal is aliased to the coefficients of the last two degrees 179 and 180. The table below summarizes the results numerically. The upper part of the table shows the computation of the pure leakage effect. A signal from 181 up to degree and order 360 is reconstructed by a spherical harmonic analysis up to degree 180. The table summarizes the residuals, if all of the reconstructed information is used (model: 180/180) in comparison to the model, where the last two degrees are used as puffer zone (178/180). The truncated model is compared with the 178 true model. The last two lines of the table reflect the behavior of the adjustment procedure, if in addition to the incomplete model (spectral leakage) an ARMA noise model is superimposed to the signal information. The third line repeats the results of a computation without spectral leakage as reference, and the fourth line shows that the additional leakage effect doesn't decrease the quality of the results very much.

model	global [m]		$-83° \leq \phi \leq 83°$		local [m]			
	min	max	min	max	min	max	mean	σ
180/180/181-360	-153	228	-0.39	0.36	-0.054	0.060	-0.000	0.012
178/180/181-360	-153	228	-0.39	0.35	-0.042	0.034	-0.000	0.009
180/180/180+arma	-48	70	-0.29	0.42	-0.089	0.082	-0.002	0.020
178/180/360+arma	-161	141	-0.36	0.42	-0.092	0.079	-0.002	0.021

mation itself. But also external accuracy prediction, done by closed loop simulations, shows the same results (cf.Fig. 2.28). The accuracy of the reconstructed geoid heights decreases with increasing degrees of the deterministic model. If, for example, a model up to degree 240 is reconstructed the table in Fig. 2.28 shows maximal errors in the range of $\pm 0.5\,m$ and the root mean square error (rms) of $\pm 0.1\,m$. In contrast, a model up to degree 180 reproduces the geoid heights in the test area with an accuracy of $\pm 0.1\,m$ maximal error and $\pm 0.02\,m$ rms. The truncation of the deterministic model causes a stabilization (regularization) of the whole procedure, and it can be stated that

the measurements at satellite altitude have not enough information to determine all the parameters.

But now back to the leakage effect. If we truncate the spherical harmonic expansion to a certain degree, all the high frequency part of the signal is not represented in the deterministic model. If a regular data distribution is assumed, the orthogonality relations provide a filtering of the signal and, therefore, the high frequency part is not absorbed by the system. In the case of satellite measurements, only well distributed measurements, but not gridded data are available. To quantify this absorption effect some test computations are performed. Fig. 2.27 shows the results of a simulation, where only the high frequent part between 181 to 360 of OSU91a model is used as input signal. The spherical harmonic analysis is performed up to degree 180. If no information is absorbed by the model, the output of the adjustment should reflect a zero field, but the individual data distribution of the test data set causes residuals in the range of $\pm 0.5\,mE$, with a rms of $\pm 0.1\,mE$.

If we reconstruct the geoid heights the pure leakage effect results in geoid disturbances in the range of $\pm 5\,cm$ and an rms of $1.2\,cm$ (cf. Fig. 2.29). It can be deduced that the last two reconstructed degrees (cf. Fig. 2.30) are mostly influenced by the leakage effect. If these last two degrees are neglected (puffer zone) a quarter of the disturbing energy is filtered out.

In contrast to these plain models, also combined models (input signals from 2 to 360 plus ARMA noise) are computed. The table at the bottom of Fig. 2.29 summarizes the results, where the undisturbed model (`180/180/180+arma`) with an rms of $\pm 20\,cm$ is used as reference model. The mixed model shows nearly the same accuracy as the model without leakage effects in the range of $\pm 9\,cm$ and an rms of $\pm 2.1\,cm$.

This seems to be very soothing, especially, because we can expect this effect to become for higher resolutions (e.g. 240-300) this effect becomes smaller and smaller due to the signal contents in the high degree regions. On the other hand, this effect is a deterministic and not a stochastic effect. Therefore, if we look at a six months measurement period, we expect an improvement of the accuracy due to independent observations (which is not really true, see discussion harmonic processes) and the average process. But the deterministic effects are not reduced by the average process and, therefore, further investigations are necessary to study this effect in detail.

Especially, the analysis of the residuals should be performed with respect to the space domain (see discussion in Sec. 2.1.1), because the truncation effect (spectral leakage) should result in a space dependent process. But it can also be seen as a non-stationary disturbing force in the time domain. The discussion in Sec. 2.1.6 shows that additional deterministic error sources result in a different behavior of the probability density functions of the resulting amplitude spectra as well as in the phase spectra. Therefore, it is necessary to look in detail at the stochastic behavior of the residuals (cf. Sec. 2.4).

Simulation 180/360

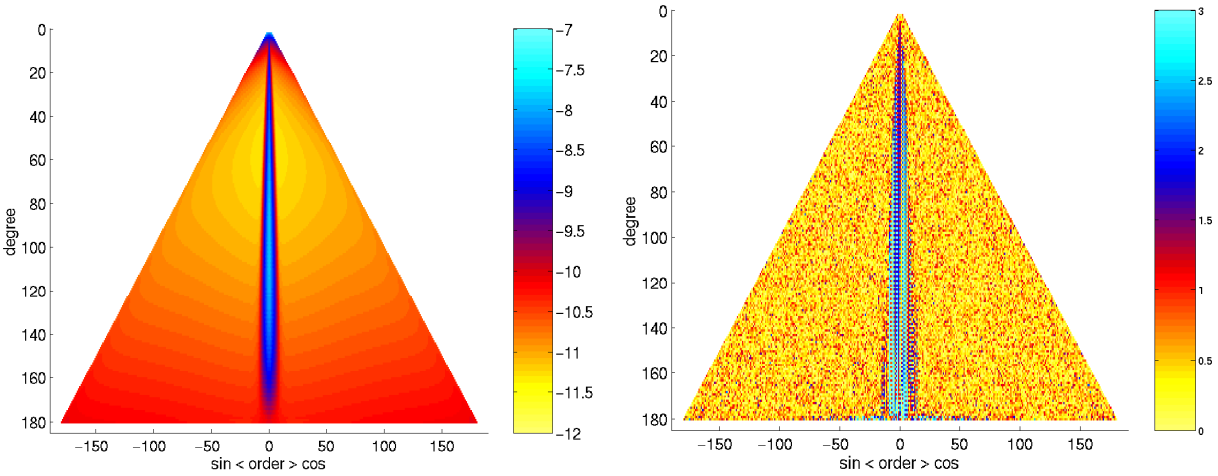

Figure 2.30: Spectral triangles: Accuracy of the spherical harmonic coefficients; (left) $\sigma_{S_{nm}}, \sigma_{C_{nm}} \ldots$ accuracy of the coefficients, $\sigma_{C_{nm}}$; (right) $\texttt{ABS}\left(C_{nm}(osu) - C_{nm}(pcgma)\right)/\sigma_{C_{nm}} \ldots$ relative accuracy of the reconstructed coefficients, range $[0 - 3\sigma]$.

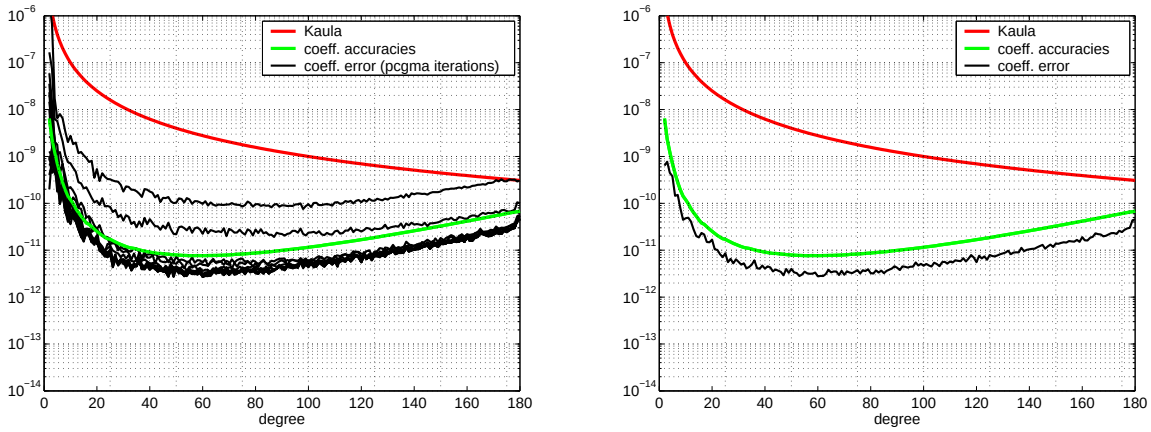

Figure 2.31: Accuracy and convergence of the spherical harmonic coefficients; median over all orders of the same degree; (left) all iterations (right) last iteration.

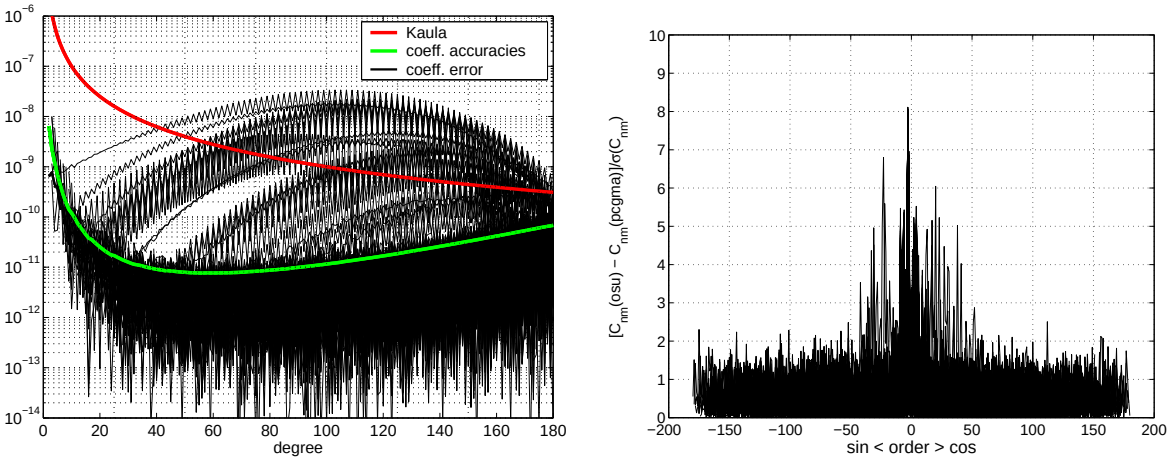

Figure 2.32: Accuracy of the solution of the spherical harmonic coefficients;
(left) per degree;
absolute discrepancies $\texttt{ABS}\,(C_{nm}(osu) - C_{nm}(pcgma))$ of the computed spherical harmonic coefficients,
(right) per order;
relative discrepancies $\texttt{ABS}\,(C_{nm}(osu) - C_{nm}(pcgma))\,/\sigma_{C_{nm}}$ of the computed spherical harmonic coefficients.

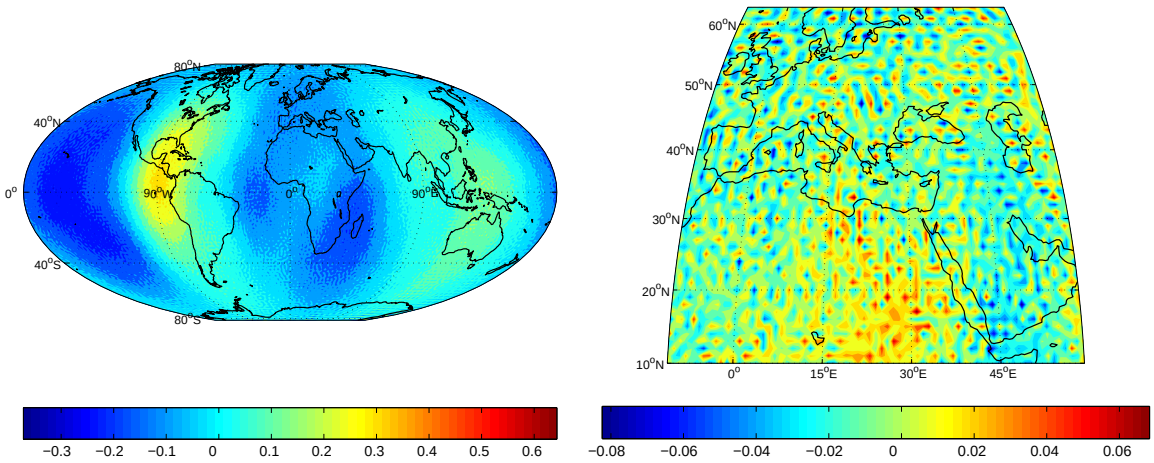

Figure 2.33: *ARMA-data-set* ($\ell_{max} = 360$); reconstruction of second level information: discrepancies of geoid heights between OSU (degree 178) and PCGMA (computed 180, used 178).
(left) global reconstruction; (global: min= -225 m, max=180 m;
$-83° \leq \phi \leq 83°$: min=-0.37 m, max=0.71 m)
(right) local reconstruction: (min = -0.082 m, max = 0.078 m,
mean = -0.003 m, rms = 0.025 m)
For the local representation the data are reduced by a moving average ($30° \times 30°$).

Simulation 222/360

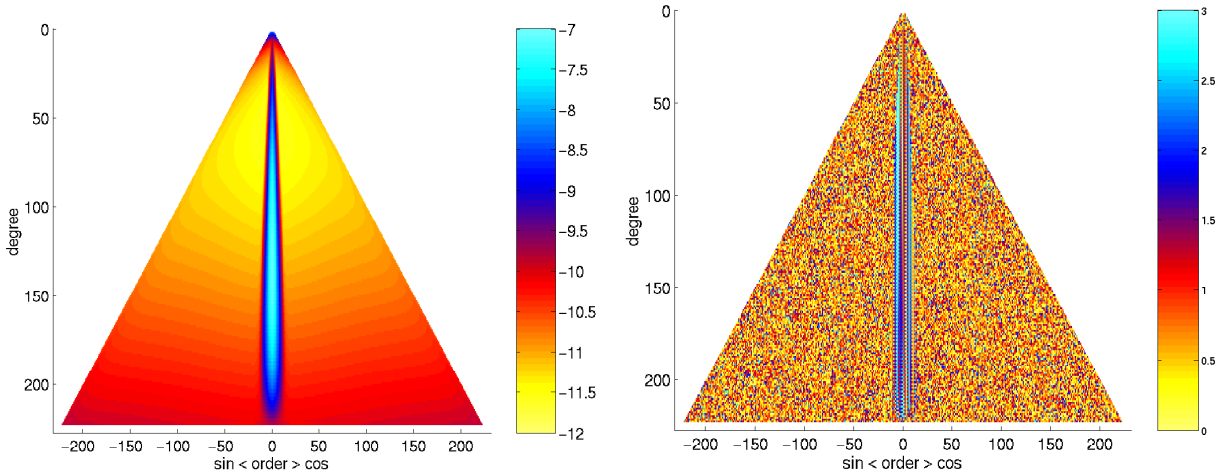

Figure 2.34: Spectral triangles: Accuracy of the spherical harmonic coefficients; (left) $\sigma_{S_{nm}}, \sigma_{C_{nm}} \ldots$ accuracy of the coefficients, $\sigma_{C_{nm}}$; (right) $\texttt{ABS}\left(C_{nm}(osu) - C_{nm}(pcgma)\right)/\sigma_{C_{nm}} \ldots$ relative accuracy of the reconstructed coefficients, range $[0 - 3\sigma]$.

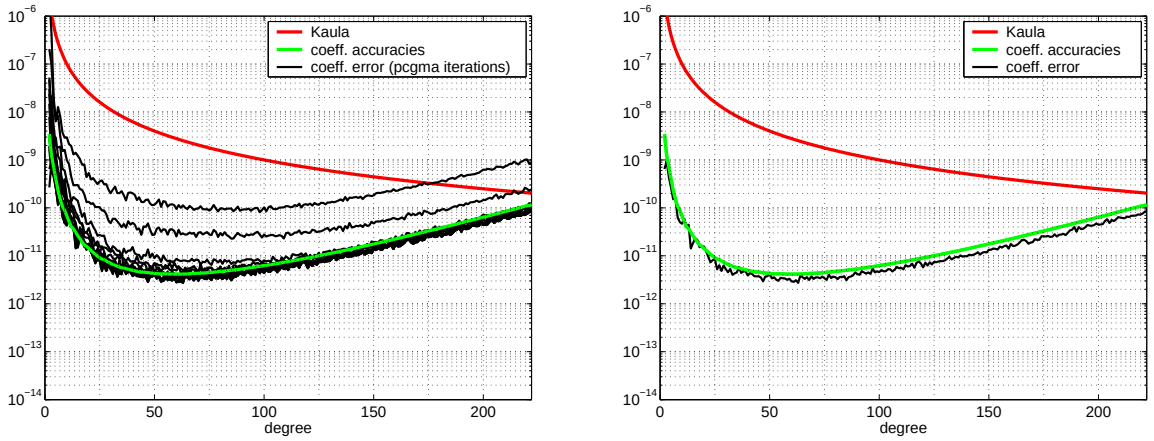

Figure 2.35: Accuracy and convergence of the spherical harmonic coefficients; median over all orders of the same degree; (left) all iterations (right) last iteration.

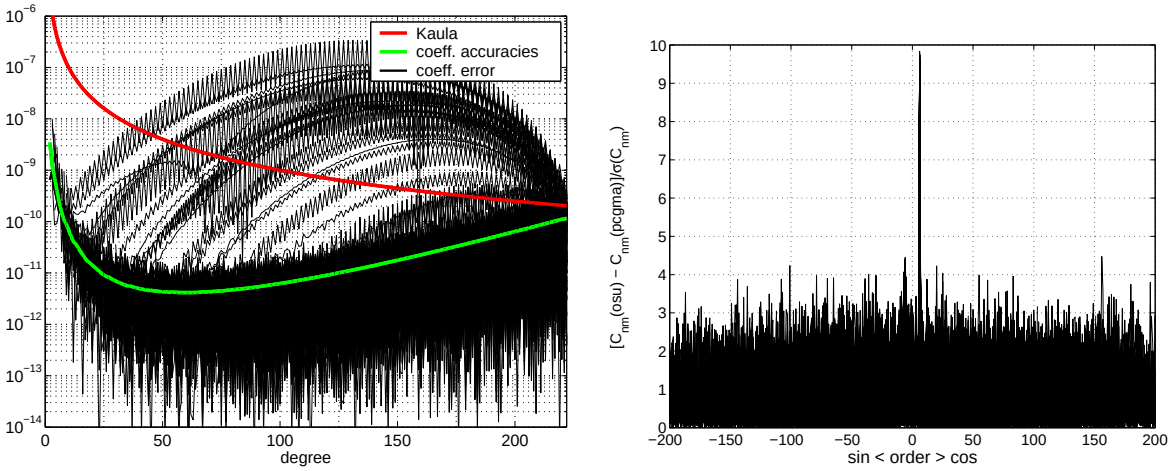

Figure 2.36: Accuracy of the solution of the spherical harmonic coefficients;
(left) per degree;
absolute discrepancies $\texttt{ABS}\,(C_{nm}(osu) - C_{nm}(pcgma))$ of the computed spherical harmonic coefficients,
(right) per order;
relative discrepancies $\texttt{ABS}\,(C_{nm}(osu) - C_{nm}(pcgma))\,/\sigma_{C_{nm}}$ of the computed spherical harmonic coefficients.

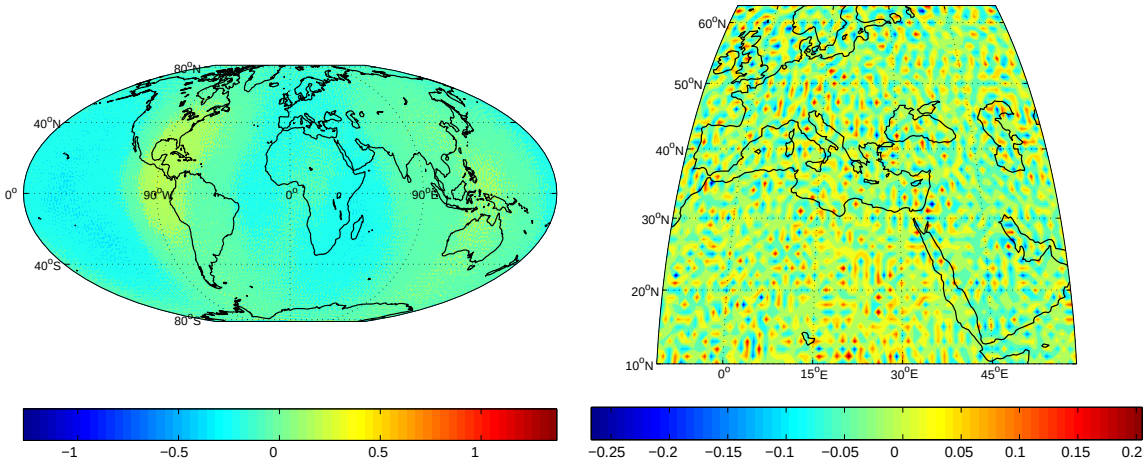

Figure 2.37: *ARMA-data-set* ($\ell_{max} = 360$); reconstruction of second level information: discrepancies of geoid heights between OSU (degree 220) and PCGMA (computed 222, used 220).
(left) global reconstruction; (global: min= -1151 m, max=2581 m;
$-83° \leq \phi \leq 83°$: min=-1.3 m, max=1.6 m)
(right) local reconstruction: (min = -0.267 m, max = 0.236 m,
mean = -0.002 m, rms = 0.075 m)
For the local representation the data are reduced by a moving average ($30° \times 30°$).

Simulation 242/360

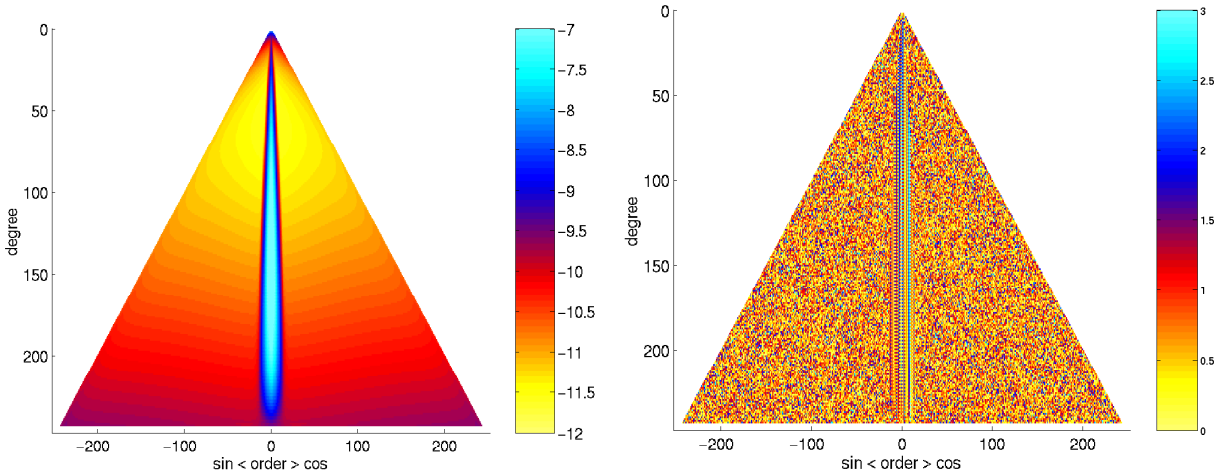

Figure 2.38 : Spectral triangles: Accuracy of the spherical harmonic coefficients; (left) $\sigma_{S_{nm}}, \sigma_{C_{nm}} \ldots$ accuracy of the coefficients, $\sigma_{C_{nm}}$; (right) $\texttt{ABS}\left(C_{nm}(osu) - C_{nm}(pcgma)\right)/\sigma_{C_{nm}} \ldots$ relative accuracy of the reconstructed coefficients, range $[0 - 3\sigma]$.

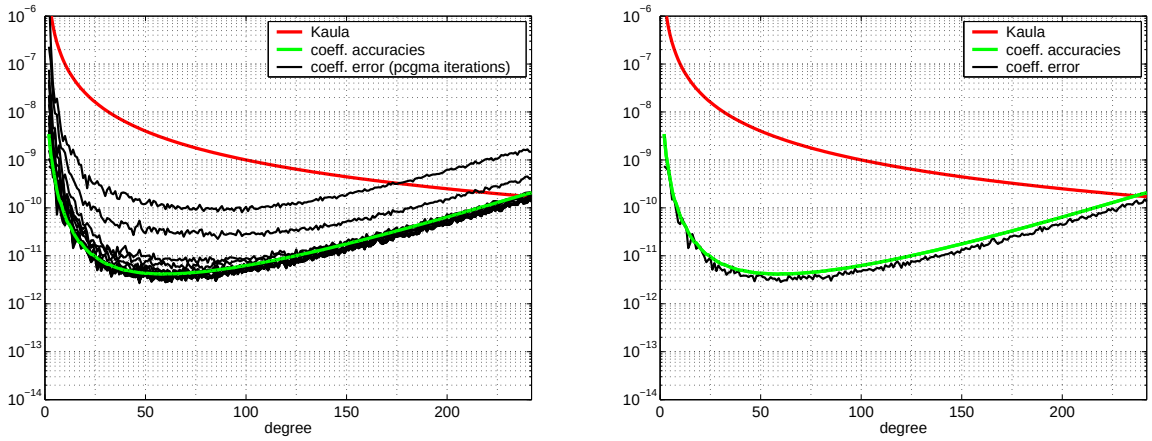

Figure 2.39 : Accuracy and convergence of the spherical harmonic coefficients; median over all orders of the same degree; (left) all iterations (right) last iteration.

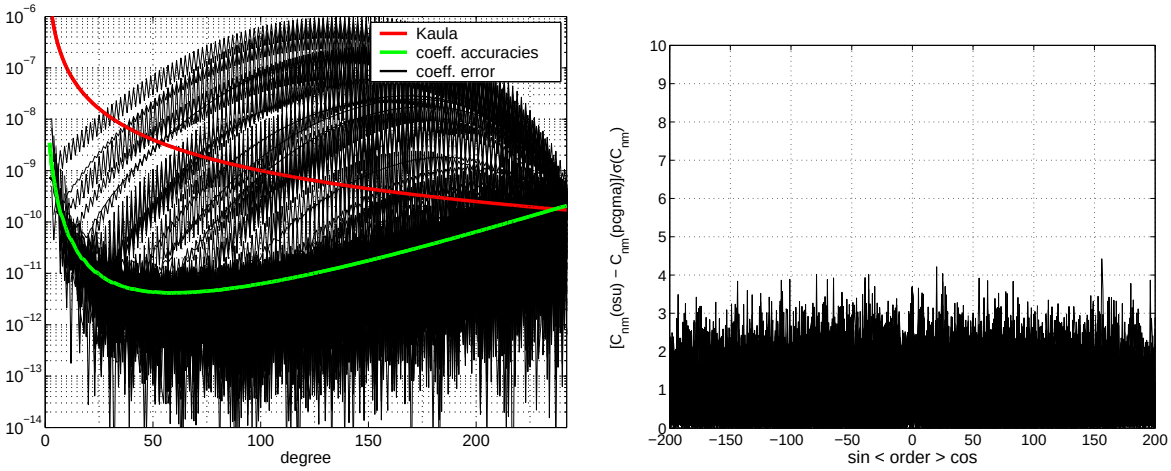

Figure 2.40 : Accuracy of the solution of the spherical harmonic coefficients;
(left) per degree;
absolute discrepancies $\texttt{ABS}\,(C_{nm}(osu) - C_{nm}(pcgma))$ of the computed spherical harmonic coefficients,
(right) per order;
relative discrepancies $\texttt{ABS}\,(C_{nm}(osu) - C_{nm}(pcgma))\,/\sigma_{C_{nm}}$ of the computed spherical harmonic coefficients.

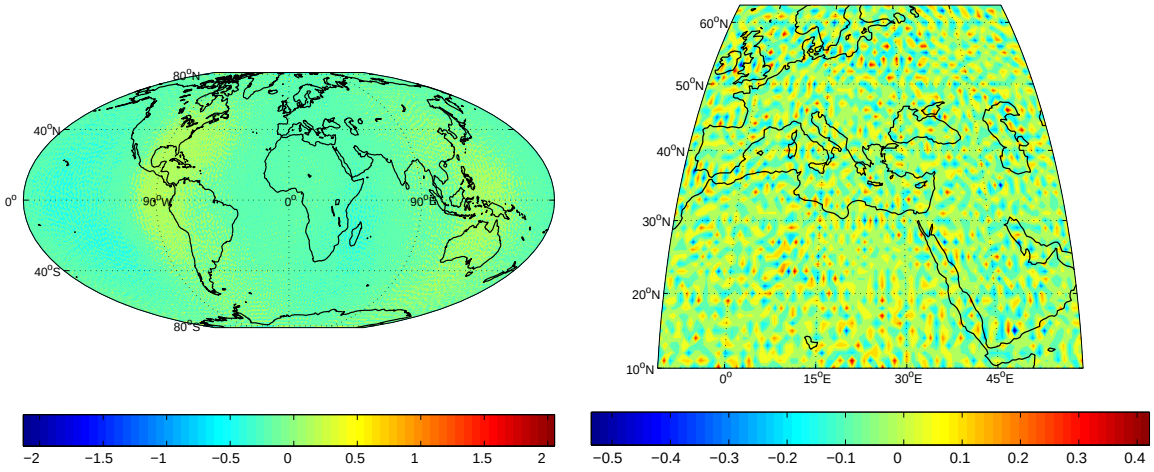

Figure 2.41 : *ARMA-data-set* ($\ell_{max} = 360$); reconstruction of second level information: discrepancies of geoid heights between OSU (degree 240) and PCGMA (computed 242, used 240).
(left) global reconstruction; (global: min= -879 m, max=7797 m;
$-83° \leq \phi \leq 83°$: min=-2.1 m, max=2.3 m)
(right) local reconstruction: (min = -0.536 m, max = 0.485 m,
mean = -0.002 m, rms = 0.139 m)
For the local representation the data are reduced by a moving average ($30° \times 30°$).

2.4 Statistical Hypotheses – Tests and Decisions

In most cases the estimated parameters of an adjustment procedure reflect the quantities of major interest. The residuals as second output stream are only used to estimate the variance of unit weight or variance components of the measurements. In addition, large individual residuals give a hint on gross errors. Data snooping procedures can be applied to detect these measurement errors. And, if a priori knowledge of the measurement accuracy is available (test measurements, calibration) the deduced variance from the residuals can be used to verify the model by statistical tests (Ω-test, cf. *KOCH (1998)[7]*).

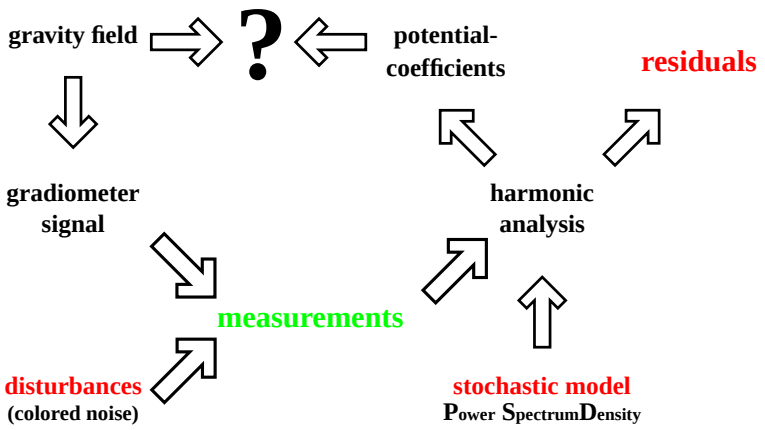

Figure 2.42 : Closed-Loop Simulation; in addition to the simulation Fig. 2.21 the residuals of the adjustment procedure serve as additional source to assess the computational process.

In case of the SGG measurements the a priori knowledge has to be verified and in addition the stability of the calibration of the measurement instruments during the whole mission time has to be controlled. Therefore, we try do develop objective criteria to evaluate the residuals.

This can be done in different ways and different domains. As a first step we look at the behavior in the time domain. We can apply strategies on the whole sequence and look at the first and second moments, the mean value and variance, but we can also compute the covariance function and compare this function with the a priori characteristics of the gradiometer. Here we have to have in mind that the residuals consist at least of two components, the colored signal components due to the measurement devices and the white noise components. But also unreduced temporal effects and other model errors (spectral leakage) may be involved in the residuals. As a next step we can split up the colored signal from the residuals and analyze the remaining part. The filtering procedure can be seen as a decorrelation process of the residuals. If we use a rigorous approach we have to use the estimated covariance matrix of the adjustment procedure, which can be deduced by the variance propagation law. Because of the huge systems, it

is (in the moment) impossible to compute these quantities. As a first approximation we introduce therefore the a priori information defined by the power spectral density of the measurements. As a result of this decorrelation process we should achieve uncorrelated, normal distributed quantities with a common variance. If we get white Gaussian noise, we can be sure that our model works well. Otherwise unmodeled effects are involved in the adjustment procedure. Additional statistical tools can be helpful to identify these inconsistencies (e.g. synchronization methods).

To supplement the time domain analysis we can also perform an analysis in the frequency domain. In sec. 2.1.3 and 2.1.4 we have elaborated the special properties of a random process in the frequency domain. In particular, we have developed the probability density distribution of the harmonic coefficients, the amplitudes and the phases of stationary and non-stationary random processes. Using this knowledge, we can design hypothesis tests also in the spectral domain to check e.g. the measurement bandwidth (cf. Sec. 2.4.3) or the filter characteristics (cf. Sec. 2.4.4).

Both test strategies, the time-domain as well as the frequency domain, can be used to analyze the complete mission (cf. Tab. 2.3 and 2.4), but can also be applied on special parts e.g. particular revolutions (cf. Fig. 2.45). Therefore, we divide the whole sequence into single revolutions and arrange the residuals in a rectangular scheme (Buys-Ballot scheme), where each column stands for one revolution. We can apply different synchronization strategies (cf. *TAUBENHEIM (1969)[16]*) to deduce additional information from the residuals in a statistically founded way.

A very similar rectangular scheme can also be built up in the frequency domain. We can transform the contents of each revolution into the frequency domain (using windowing and overlapping regions to reduce the (space-domain) leakage). For convenience we use now the transposed scheme. Each column of the complex scheme stands now for the coefficients of a special frequency. The rows characterize different realization of this process. Again we can apply hypothesis tests to analyze the spectral contents of the residuals in detail.

2.4.1 Test Data Sets

To show the wide range of different hypothesis tests we restrict ourself to two data scenarios, otherwise it will be too complex. As a standard scenario a `pcgma` solution of the *ARMA-data-set* as described in Sec. 2.3.1.1 is used. The spherical harmonic analysis up to degree 180 is computed with the new version `pcgma 3.0` on the workstation cluster of the Institute of Theoretical Geodesy, University Bonn. We use six Pentium 4 ($1.8\,GHz$) processing units and optimal tailored BLAS (Basic Linear Algebra Subprograms) routines to speed up the computations. The ARMA(2,2) filter (cf. Fig. 2.18) with a warm-up phase of 100 samples ($500\,s$) are used to describe the correlations. The global accuracy of the solution is already summarized in Fig. 2.24 and in the table of the caption of Fig. 2.29, respectively. This parallelly computed model corresponds exactly with the solution of the sequentially computed model `180/180/180+arma`. The behavior of the residuals and the filtered residuals is illustrated in Fig. 2.43. This test scenario is denoted as *stat-model-standard*.

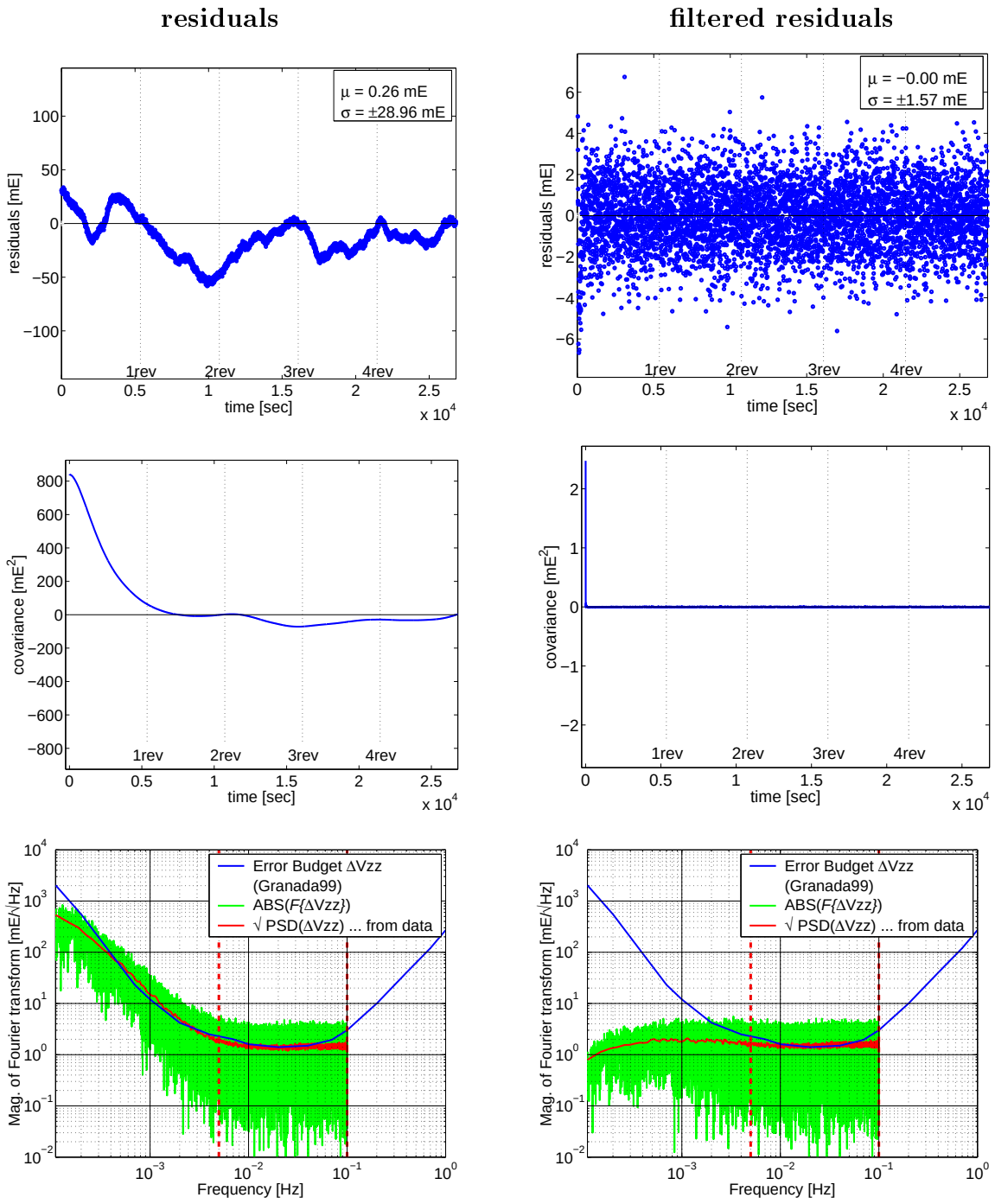

Figure 2.43 : Residuals of the *stat-model-standard* computed with `pcgma 3.0` with six computing nodes. As input signal a 180 OSU-model with superimposed ARMA noise is used. The spherical harmonic analysis is performed up to degree 180 (model: `180/180/180+arma`)
(left): residuals res_{zz} (right): filtered residuals $FILTER(res_{zz})$
(top): signals (middle): empirical covariance function
(bottom): periodogram and power spectrum density

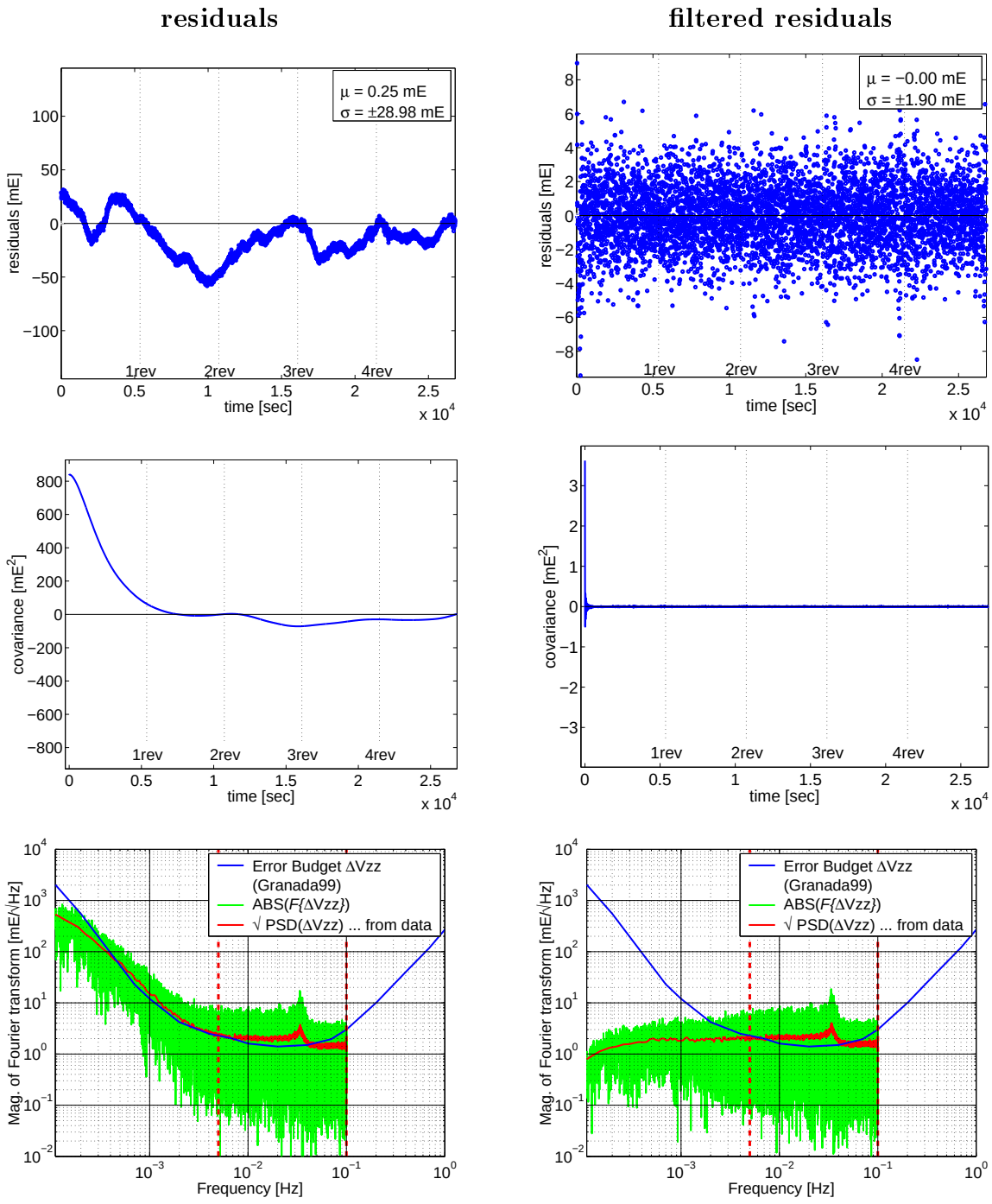

Figure 2.44: Residuals of the *stat-model-leakage* computed with `pcgma 2.5` with six computing nodes. As input signal a 360 OSU-model with superimposed ARMA noise is used. The spherical harmonic analysis is performed up to degree 180 and the coefficients up to degree 178 are compared (model: `178/180/360+arma`)
(left): residuals res_{zz} (right): filtered residuals $FILTER(res_{zz})$
(top): signals (middle): empirical covariance function
(bottom): periodogram and power spectrum density

In contrast to the consistent *stat-model-standard* an inconsistent model *stat-model-leakage* is taken into account. This model was also already introduced in Sec. 2.3.3 and was denoted as `178/180/360+arma`. The input data set of this model consists of a signal content up to degree 360 with a superimposed colored ARMA noise. All coefficients up to degree 180 are computed by a spherical harmonic analysis, but only the components up to degree 178 are included in the final model. The last two degrees serve as puffer zone (see discussion in Sec. 2.3.3). Fig. 2.44 summarizes the behavior of the residuals. Especially the filtered residuals on the left side reflect the deviations from the *stat-model-standard* model. Small deviations in the covariance function of the filtered residuals, as well as the typical behavior in the frequency domain, indicate model inconsistencies. In the next section we will elaborate strategies to evaluate this deviations in a statistical strict manner.

2.4.2 Hypothesis-Tests — Homogeneity

This test performs an analysis of variances and compares the residuals of the individual revolutions. The individual mean value and variance of each group (revolution) - columns of the Buys-Ballot scheme - is compared with the deviations of the mean values of the whole ensemble. The purpose of this test is to find out whether residuals from several groups (revolutions) have a common mean. The test returns a test-value, a fractile (F-distribution, 95%), and a p-value, which is defined by the (two-tailed) area beneath the probability density function outside the calculated test value. A p-value near zero casts doubt on the hypothesis and a p-value near one ratifies the assumptions. Usually the p-values are multiplied by a factor of 100 and expressed in percent. These values give us an indicator to accept the null hypothesis that the residuals of each group (revolution) have a common mean. The test is done with respect to a given probability (e.g. 95%).

We have implemented two different test strategies. The *variance-analysis-test* bases on independent, normally distributed samples and the *kruskal-wallis-test* performs a non-parametric analysis comparing the medians of the residuals of each revolution. The tables 2.3 and 2.4 show the output of these tests with respect to the data sets, *stat-model-standard* and *stat-model-leakage*. Both data sets form a consistent ensemble.

If we compare the results of two test strategies, we can see, that the ratio between testvalue and fractile (95%) has in both cases nearly the same size, approximately 1:5. Therefore, it can be stated, without doubt (p-value 1.000) that the mean value of the residuals of each group (revolution) does not change with time. But to be exact the strict formulation has to be: "Using this data set, we can not detect non-stationary effects". This includes the uncertainty that there might be non-stationary effects, but caused by the variance of the residuals we can't deduce them.

If we look at the results of the model *stat-model-leakage* (cf. Tab. 2.4) we can see an increase of the total variance of the residuals from $1.573\,mE$ to $1.904\,mE$ [1]. The test-value decreases because of these additional uncertainties. It can be stated that it will be more difficult to detect non-stationary effects with this data set.

[1] As mentioned above, this fact can be used to formulate statistical tests, e.g. Ω-test, but then a priori knowledge of the measurement accuracy is necessary, or we have to assume an ideal parameterization. Both assumptions are not realistic in our case.

```
+-------------------------------------------------------------------+
|  Variance-Analysis Test           vtv           f        sigma |
+-------------------------------------------------------------------+
|  total:                       1239621.762    501090       1.573 |
|  varianz of mean values:          211.927       466       0.674 |
|  mean group variance:         1239409.835    500624       1.573 |
+-------------------------------------------------------------------+
|     testvalue      =        0.184                                 |
|     fractile       =        1.110                                 |
|     p-value        =        1.000                                 |
+-------------------------------------------------------------------+
ans = TRUE
+-----------------------------------+
|        Kruskal & Wallis test      |
+-----------------------------------+
|  testvalue      =         103.552 |
|  fractile       =         517.326 |
|  p-value        =           1.000 |
+-----------------------------------+
ans = TRUE
```

Table 2.3: Hypothesis-Test on Homogeneity; filtered residuals *stat-model-standard*, probability 95%: The test-values of both tests indicate that the data set reflects a homogeneous behavior over all revolutions. No non-stationary effects (time dependent trends) can be identified.

```
+-------------------------------------------------------------------+
|  Variance-Analysis Test           vtv           f        sigma |
+-------------------------------------------------------------------+
|  total:                       1817335.095    501090       1.904 |
|  varianz of mean values:          211.541       466       0.674 |
|  mean group variance:         1817123.554    500624       1.905 |
+-------------------------------------------------------------------+
|     testvalue      =        0.125                                 |
|     fractile       =        1.110                                 |
|     p-value        =        1.000                                 |
+-------------------------------------------------------------------+
ans = TRUE
+-----------------------------------+
|        Kruskal & Wallis test      |
+-----------------------------------+
|  testvalue      =          91.042 |
|  fractile       =         517.326 |
|  p-value        =           1.000 |
+-----------------------------------+
ans = TRUE
```

Table 2.4: Hypothesis-Test on Homogeneity; filtered residuals *stat-model-leakage*, probability 95%: The test-values of both tests indicate that this data set reflects a homogeneous behavior over all revolutions. No non-stationary effects (time dependent trends) can be identified.

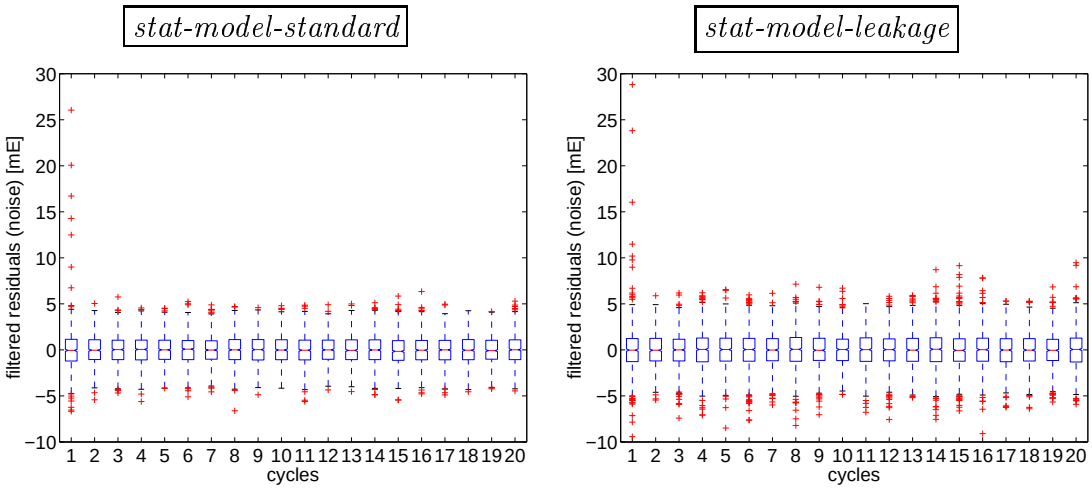

Figure 2.45 : The boxplot (MATLAB Statistic toolbox) produces a box and whisker plot for each revolution. The box has lines at the lower quartile, median, and upper quartile values and represents the range, where 50% of the data is situated. 25% of the samples reflects larger (smaller) values. The whiskers are lines extending from each end of the box by a factor of 1.5 to show the extent of the rest of the data. Outliers are data with values beyond the ends of the whiskers (two times larger than the quartile of the data).

The deviations due to spectral leakage are homogeneously distributed over all revolutions, and therefore, all the samples of the groups (revolutions) are consistent. If we want to look into details the plotting routine BOXPLOT of the *MATLAB© Statistical Toolbox* may be an appropriate tool. Fig. 2.45 shows an analysis of the first twenty (20) revolutions of both test data sets. The filtered residuals reflect the same mean (median) values for all revolutions (red bar in the boxes). In both cases the analysis of the first revolution reflects a larger number of *outliers*. These outliers are caused by the warm-up of the discrete filters in the analysis tool, because for the boxplot we use the entire sequence and don't eliminate the first 100 values (see discussion in Sec. 2.2.4).

At first glance we can detect that the number of outliers (values outside the whiskers) increases in the model *stat-model-leakage* (see right plot in Fig. 2.45). Additional tests on the distribution of the data can be used to deduce detailed information.

2.4.3 Hypothesis-Tests — Measurement Bandwidth

This test is based on a piecewise representation of the measurement series in the spectral domain. The residuals are divided into groups (e.g. single revolution or sections with ten revolutions). Each section is transformed into the frequency domain by a Fourier transformation. To avoid leakage effects a windowing is considered by a Hanning window. The results of all groups are collected again in a rectangular scheme, where each row represents the complex coefficients of a group (revolution).

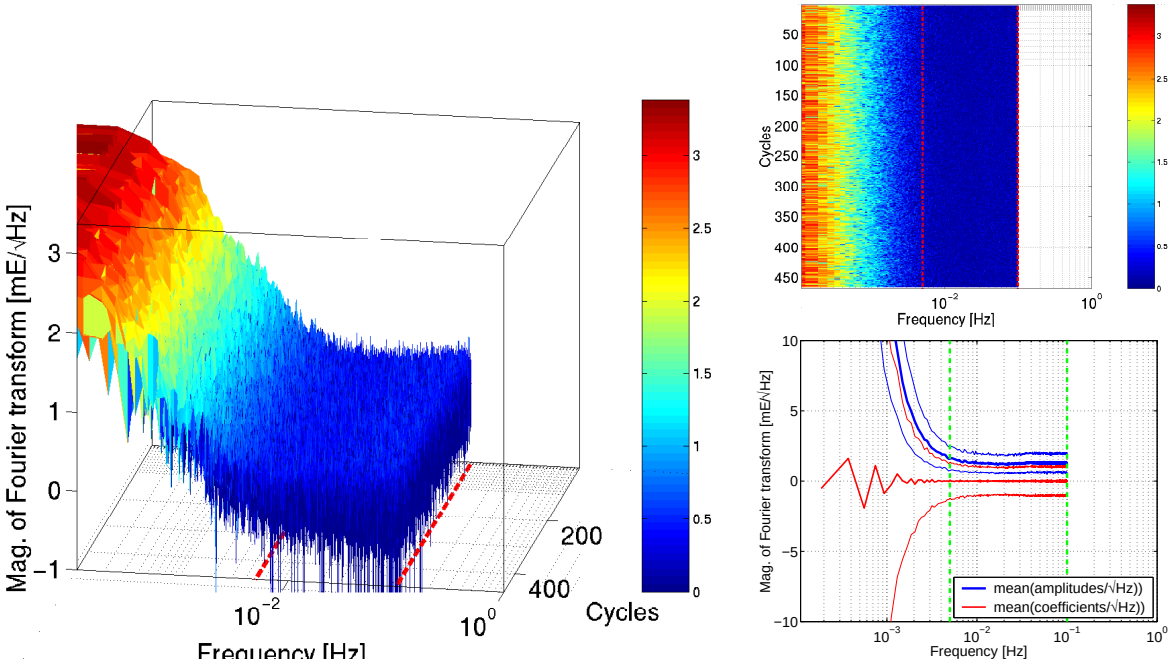

Figure 2.46: Spectrogram of the residuals; residuals *stat-model-standard*; These figures show a 3D, 2D and 1D picture of the amplitude spectra, where each row represents the amplitude spectrum of a group (one revolution). The left picture summarizes the different independent realizations and reflects the spectral behavior of the colored noise. The upper right picture shows the spectrogram, a 2D representation of a piecewise spectral representation of the measurement series. The lower right figure collects a column-wise (frequency-wise) evaluation of the mean values of the coefficients (red), the amplitudes (blue) and the corresponding confidence regions on one sigma level.

Figs. 2.46 and 2.48 illustrate this rectangular scheme. The columns of this scheme collect the coefficients of a special frequency and thus represent different realizations of the random process. The graphs in the lower right of Figs. 2.46 and 2.48 show that the mean values are *'near'* zero and the variances increase with low frequencies. This corresponds exactly to the definition of the harmonic process.

In Sec. 2.1.4 the statistical behavior of the coefficients and the amplitudes of a random harmonic process was elaborated and we have formulated there that the coefficients of

a random process are uncorrelated, zero mean and random variables with a common variance for each individual frequency. This information can now be used to design hypothesis tests to find an ensemble of frequencies, which reflects the same statistical behavior. We use three different test-strategies:

- the *F-test* is based on the assumption that the coefficients are normally distributed and independent (independent sections without overlapping).
- the *analysis of the variances* uses the similarity between the *Rayleigh-* and *Rice-*distribution and the normal distribution. The amplitudes are analyzed frequency by frequency to find consistent ensembles with respect to a initially defined frequency.
- the *Kruskal-Wallis test* is a nonparametric version of the variance analysis, where no assumption on the probability density functions of the coefficients is necessary.

If the unfiltered residuals are introduced as test quantities, a sequential test procedure can be designed to determine the measurement bandwidth of the instrument. The purpose of these tests is to detect an ensemble of frequencies, which have a common mean value. All results of these computations are summarized in Figs. 2.47 and 2.49.

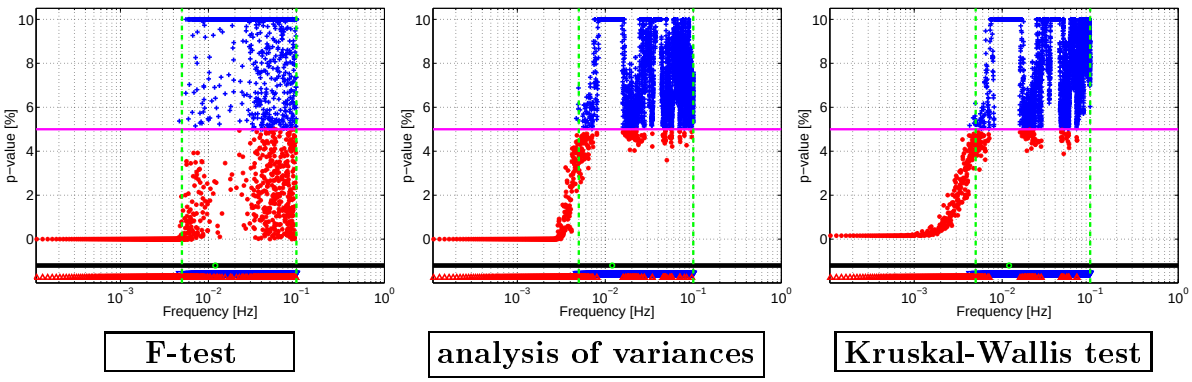

Figure 2.47: Evaluation of the measurement bandwidth; sampling *stat-model-standard*; This figure collects the results of three test-strategies to determine the measurement bandwidth. Blue triangles mark frequencies which form an ensemble with respect to the start frequency (green circle). In contrast to this all red marked frequencies don't belong to this ensemble. The p-values give an indicator for the error of first kind, if the assumption is neglected. The actual test probability (magenta line) limits the region of acceptance and refusal. In the upper part of each figure the p-values of each frequency are collected. In the lower part (under the black line) the results are summarized to impact an overall feeling of the spectral behavior.

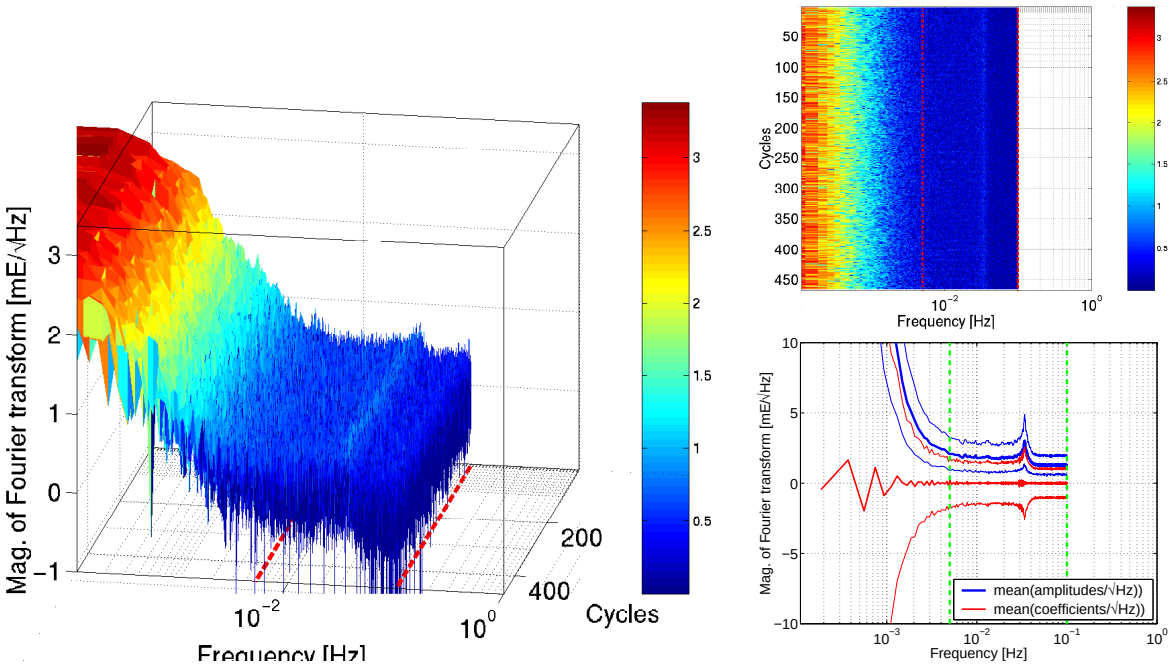

Figure 2.48: Spectrogram of the residuals; sampling *stat-model-leakage*; These figures show a 3D, 2D and 1D picture of the amplitude spectra, where each row represents the amplitude spectrum of a cycle (one revolution). The left picture summarizes the different independent realizations and reflects the spectral behavior of the colored noise. The upper right picture shows the spectrogram, a 2D representation of a piecewise spectral representation of the measurement series. The lower right figure collects a column-wise (frequency wise) evaluation of the mean values of the coefficients (red), the amplitudes (blue) and the corresponding confidence regions on one sigma level.

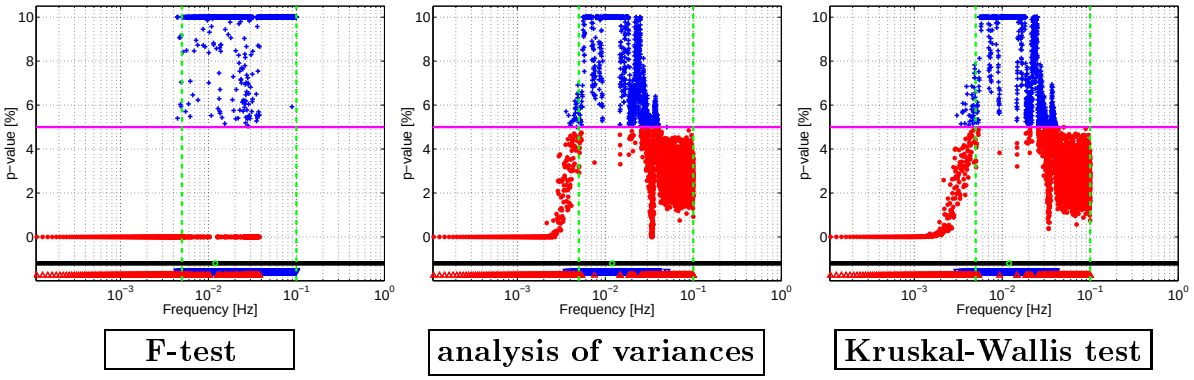

Figure 2.49 : Evaluation of the measurement bandwidth; sampling *stat-model-leakage*; This figure collects the results of three test-strategies to determine the measurement bandwidth. Blue triangles mark frequencies which form an ensemble with respect to the start frequency (green circle). In contrast to this all red marked frequencies don't belong to this ensemble. The p-values give an indicator for the error of first kind, if the assumption is neglected. The actual test probability (magenta line) limits the region of acceptance and refusal. In the upper part of each figure the p-values of each frequency are collected. In the lower part (under the black line) the results are summarized to impact an overall feeling of the spectral behavior.

It should be mentioned that further investigations are necessary to optimize these test procedures. At the moment these sequences of hypothesis tests have a lot of control parameters (sorting, initial point, search direction, number of iterations) which are all implemented to have maximum flexibility. Additional research is necessary to tune these parameters with the purpose to design a highly sensitive procedure with the best utilization of the given data set.

2.4.4 Hypothesis-Tests — Filter Characteristics

This test uses the same scheme as the test in Sec. 2.4.3, where the measurement bandwidth is tested. Again a rectangular scheme in the frequency domain is build up, but in contrast to the measurement-bandwidth-test we now collect the spectral representation of the filtered residuals. We apply the same test strategies, with the same assumptions like in Sec. 2.4.3, and can determine now, which frequencies are involved in the filtered residuals. Again we construct ensembles of frequencies. The Fig. 2.50 summarizes the results.

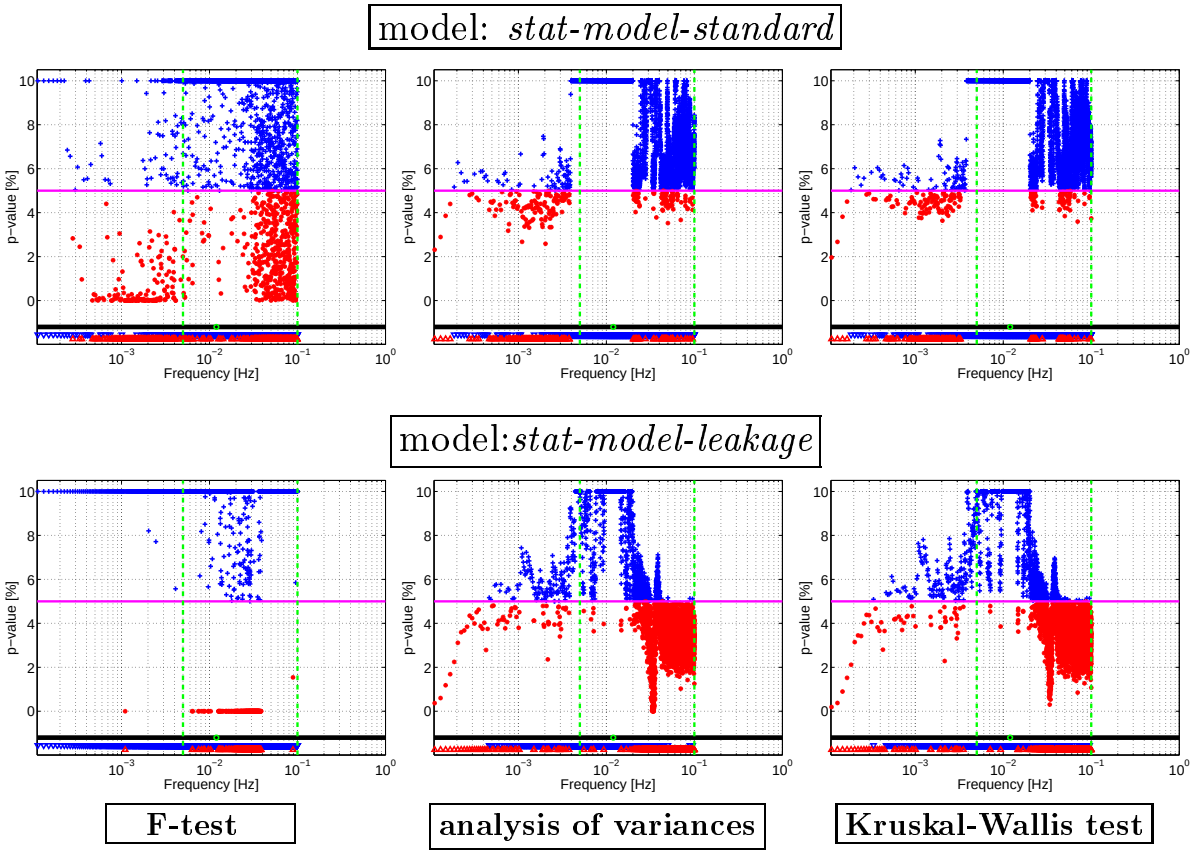

Figure 2.50: Verification of the filter characteristics; filtered residuals; first row: *stat-model-standard*; second row: *stat-model-leakage*; This figure collects the results of three test-strategies to control the filter characteristics. Blue triangles mark frequencies which form an ensemble with respect to the start frequency (green circle). In contrast to this all red marked frequencies don't belong to this ensemble. The p-values give an indicator for the error of first kind, if the assumption is neglected. The actual test probability (magenta line) limits the region of acceptance and refusal. In the upper part of each figure the p-values of each frequency are collected. In the lower part (below the black line) the results are summarized to impact an overall feeling of the spectral behavior.

2.4.5 Conclusion - Outlook

The large amount of data and information gives the possibility to apply powerful statistical strategies to assess the residuals of a spherical harmonic analysis. In Fig. 2.51 a structural overview about the test strategies is given.

	residuals	**filtered residuals**
time-domain	**gross error detection** **Ω-test** **variance-components**	**independence** **homogeneity** **correlation length**
frequency-domain	**measurement bandwidth**	**filter characteristics** **periodic effects** **det. model errors**

Figure 2.51: Test strategies to analyse the residuals.

But it has to be mentioned, that this first tests can only demonstrate the large potential of these statistical tests. Further investigations are necessary to adapt common tools, to design new strategies and to tune the parameters to get best results.

References

[1] Bottoni G.P., R. Barzaghi: 1993, 'Fast Collocation'. Bulletin Geodesique, Vol. 67, No. 2, pp. 119-126.

[2] Buttkus B.: 2000, 'Spectral Analysis and Filter Theory in Applied Geophysics'. Springer, Berlin.

[3] ESA SP-1233(1): 1999, 'The Four Candidate Earth Explorer Core Missions - Gravity Filed and Steady-State Ocean Circulation Mission'. Granada 1999.

[4] ESA: 1998, 'From Eötvös to Milligal'. Final Report of the ESA study 13392/98/NL/GD.

[5] ESA: 2000, 'GOCE End-to-End Closed Loop Simulation'. Final Report, ESA study.

[6] Koch K.R., M. Schmidt: 1994, 'Deterministische und stochastische Signale'. Dümmler, Bonn.

[7] Koch K.R.: 1994, 'Parameterschätzung und Hypothesentests in linearen Modellen'. Dümmler, Bonn.

[8] Moritz, H.: 1980, 'Advanced Physical Geodesy'. Wichmann, Karlsruhe.

[9] Oppenheim A., R. Schafer: 1975, 'Digital Signal Processing'. Prentice-Hall Inc., Englewood Cliffs, New Jersey.

[10] Rummel R. et al.: 1993, 'Spherical harmonic analysis of satellite gradiometry'. Neth. Geod. Comm., no. 39.

[11] Sneeuw N.: 2000, 'A semi-analytical approach to gravity field analysis from satellite observations'. Dissertation, DGK, no. 527.

[12] Schuh W.-D.: 1996, 'Tailored Numerical Solution Strategies for the Global Determinations of the Earth's Gravity Field'. Mitteilungen der geodätischen Institute der TU Graz, no. 81.

[13] Schuh W.-D., H. Sünkel, W. Hausleitner, E. Höck: 1996, 'Refinement of Iterative Procedures for the Reduction of Spaceborne Gravimetry Data'. ESA-Project CIGAR IV, WP 4, Final Report, pp. 157-212.

[14] Schuh W.-D., R. Pail, G. Plank: 2001, 'Assessment of different numerical solution strategies for gravity field recovery'. Proceedings of the "International GOCE User Workshop", April 23-24, ESTEC, Noordwijk.

[15] Strang, G.: Introduction to Applied Mathematics. Wessesley-Cambridge Press, Massachusetts

[16] Taubenheim J.: 1969, 'Statistische Auswertung geophysikalischer und meteorologischer Daten'. Akademische Verlagsgesellschaft Gest & Portig, Leipzig.

[17] Wasle E., W.-D. Schuh: 2000, 'Leakage and aliasing effects in the framework of discrete spectral analysis'. Poster Presentation, EGS XXV General Assembly, Nice.

[18] Wasle E.: 2001, 'The Significance of Orthogonality in the Framework of Digital Signal Analysis'. Diploma thesis, TU Graz.